NEW THEORETICAL MODELS AND RATIO IMAGING TECHNIQUES ASSOCIATED WITH THE NASA EARTH RESOURCES SPECTRAL INFORMATION SYSTEM

by

R. K. Vincent
Infrared and Optics Division

ENVIRONMENTAL RESEARCH INSTITUTE OF MICHIGAN

FORMERLY WILLOW RUN LABORATORIES.
THE UNIVERSITY OF MICHIGAN

JULY 1974

prepared for

NOTICES

/b

1. Report No. NASA CR-ERIM 190100-30-T	2. Government Accession No.	3. Recipient's Catalog No.
4. Title and Subtitle NEW THEORETICAL MODELS AND RATIO IMAGING TECHNIQUES ASSOCIATED WITH THE NASA EARTH RESOURCES SPECTRAL INFORMATION SYSTEM		5. Report Date July 1974
		6. Performing Organization Code
7. Author(s) R. K. Vincent		8. Performing Organization Report No. ERIM 190100-30-T
9. Performing Organization Name and Address Environmental Research Institute of Michigan Infrared and Optics Division P.O. Box 618 Ann Arbor, MI 48107		10. Work Unit No. Task V
		11. Contract or Grant No. NAS 9-9784
12. Sponsoring Agency Name and Address National Aeronautics and Space Administration Johnson Space Center Earth Observations Division Houston, TX 77058		13. Type of Report and Period Covered Technical Report 1 February 1973 through 31 January 1974
		14. Sponsoring Agency Code

15. Supplementary Notes
Dr. Andrew Potter/TF3, serves as Technical Monitor for NASA.

16. Abstract

Four independent investigations are reported; in general these are concerned with improving and utilizing the correlation between the physical properties of natural materials as evidenced in laboratory spectra and spectral data collected by multispectral scanners.

(1) Two theories permitting the calculation of emittance spectra for rock and mineral surfaces of various particle sizes are compared to show that, for most silicate rock surfaces, texture does not exercise as much control as chemical composition over the spectral emittance. This holds true as long as the diameters of particles comprising the surface are on the order of $30 \mu m$ or larger — as is the case for most rocks not covered by products of weathering.

(2) Optimum filter combinations for implementing a two-channel thermal infrared ratio technique with low-altitude aircraft scanner data, for the purpose of discriminating among silicate rock types on the bases of $\% SiO_2$ and $\% (SiO_2 - A\ell_2O_3)$, are shown to be 8.1-10.1 μm for the shorter wavelength filter and 9.2-11.2 μm for the longer wavelength filter.

(3) Approximately 235 laboratory spectra of soils, minerals, rocks, and some vegetation were condensed into 11-digit ratio codes for use with ERIM's M-7 airborne multispectral scanner. These codes can be used for feature selection

17. Key Words Spectral ratioing Geology remote sensing Infrared Aerosol surface Rock-surface model modeling Aircraft ratio codes Logic design	18. Distribution Statement Initial distribution is indicated at the end of this document.

19. Security Classif. (of this report) UNCLASSIFIED	20. Security Classif. (of this page) UNCLASSIFIED	21. No. of Pages	22. Price

PRICES SUBJECT TO CHANGE

16. Abstract (Continued)

and in searching for false alarm candidates. Eventually they may be used as training sets for completely automatic data processors of the future.

(4) A system for producing automatic recognition maps aboard either a space shuttle or high-altitude aircraft of the future is outlined. A preprocessor and automatic recognition map processor for automatic on-board processing through use of a sequence of binary decisions based on ratio gating and computer-stored ratio codes as training sets are described in general terms.

PREFACE

A comprehensive multispectral program devoted to the advancement of state-of-the-art techniques for remote sensing of the environment has been a continuing program at the Environmental Research Institute of Michigan (ERIM), formerly the Willow Run Laboratories of The University of Michigan. The basic objective of this multidisciplinary program is to develop remote sensing as a practical tool to provide the user with processed information quickly and economically.

The importance of providing timely information obtained by remote sensing to such people as the farmer, the city planner, the conservationist, and others concerned with problems such as crop yield and disease, urban land studies and development, water pollution, and forest management must be carefully considered in the overall program. The scope of our program includes: (1) extending the understanding of basic processes; (2) discovering new applications; (3) developing advanced remote-sensing systems; (4) improving fast automatic data processing systems to extract information in a useful form; and also (5) assisting in data collection, processing and analysis as well as in ground truth verification.

This document is a technical report for NASA Contract NAS 9-9784 and covers the period from 1 February 1973 through 31 January 1974. Dr. Andrew Potter of NASA-Houston is Technical Monitor. The overall program is guided by Mr. R. R. Legault, an ERIM Vice-President and Director of the Infrared and Optics Division. The work reported herein was directed by J. D. Erickson, Head of the Multispectral Analysis Section. The ERIM number for this report is 190100-30-T.

CONTENTS

PRECEDING PAGE BLANK NOT FILMED

FIGURES

TABLES

NEW THEORETICAL MODELS AND RATIO IMAGING TECHNIQUES ASSOCIATED WITH THE NASA EARTH RESOURCES SPECTRAL INFORMATION SYSTEM

1
SUMMARY

During the years 1970-72, NASA's Johnson Space Center in Houston sponsored the compilation and storage of laboratory spectra of natural materials in the Earth Resources Spectral Information System (ERSIS) originally established by the Willow Run Laboratories and now maintained by WRL's successor organization, ERIM. Although ERSIS laboratory spectra have proved useful in educating the remote sensing community about spectral features associated with various chemical compositions, their usefulness for quantitative data analysis has been limited. The primary reason for this has been the lack of theoretical models with which to link laboratory data to multispectral scanner data.

This report is directed toward providing that link. Dealing with geological remote sensing problems, it contains the results of four independent investigations having two things in common: all make use of the types of spectral curves available in ERSIS, and all are concerned with correlating the physical data collected from multispectral scanners.

In one investigation, two theoretical models were devised that permit the calculation of spectral emittance spectra for rock and mineral surfaces of various particle sizes. The simpler of the two models can be used to qualitatively predict the effect of texture on the spectral emittance of rocks and minerals; it is also potentially useful as an aid in predicting the identification of natural atmospheric aerosol constituents. The second investigation determined, via an infrared ratio imaging technique developed earlier under this NASA task, the best pair of infrared filters for silicate rock-type discrimination. In a third investigation, laboratory spectra of natural materials were compressed into 11-digit ratio codes for use in feature selection, in searches for false alarm candidates, and eventually for use as training sets in completely automatic data processors. In the fourth investigation, general outlines of a ratio preprocessor and an automatic recognition map processor are developed for on-board data processing in the space-shuttle era; here, ratio codes of laboratory and field spectra may serve as substitutes for in-scene training sets.

2

INTRODUCTION

This report, the fourth in a series [1-3], is directed toward providing theoretical models capable of linking laboratory spectral data with multispectral scanner data in order to solve geological remote sensing problems. It contains the results of four independent investigations conducted under the ERSIS task of NASA Contract NAS 9-9784. These investigations have two things in common: all make use of the types of spectral curves on hand in ERSIS, and all are concerned with correlating the physical properties of natural materials—as evidenced in laboratory spectra— to spectral data collected by multispectral scanners. Thus the various procedures described are designed to make the interpretation of multispectral scanner data, by scientists in the remote sensing community, easier and more comprehensible; they should also prove useful in planning remote sensing experiments in which multispectral scanners are included.

Two investigations were begun last year and completed in the early part of this contract year. The first one, reported in Section 3 under the title, "Two Models for Irregular Rock and Mineral Surfaces," presents theories which permit the calculation of approximate spectral emittance spectra for rock and mineral surfaces of various particle sizes. The inputs to the simplest model are a near-normal-incidence infrared reflectivity curve for a polished surface of the rock or mineral and a specified particle size typical of the rock or mineral surface under natural conditions. This model is also potentially an aid to the prediction or identification of natural atmospheric aerosol constituents, as discussed in Section 3.4. The results of Section 3.3 have already, in fact, been found useful to NASA scientists at Goddard Space Flight Center, who are comparing calculated spectra of atmospheric models with infrared spectra of the Martian atmosphere from the Mars Mariner mission.

1. Vincent, R. K., R. Horvath, F. Thomson, and E. Work, Remote Sensing Data-Analysis Projects Associated with the NASA Earth Resources Spectral Information System, Report No. 31650-26-T, NASA Contract NAS 9-9784, Willow Run Laboratories of the Institute of Science and Technology, The University of Michigan, Ann Arbor, 1972.

2. Suits, G., R. K. Vincent, H. Horwitz, and J. Erickson, Optical Modeling of Agricultural Fields and Rough-Textured Rock and Mineral Surfaces, Report No. 31650-78-T, NASA Contract NAS 9-9784, Environmental Research Institute of Michigan, Ann Arbor, November 1973.

3. Vincent, R. K., Rock-Type Discrimination from Ratio Images of Pisgah Crater, California, Report No. 31650-77-T, NASA Contract NAS 9-9784, Willow Run Laboratories of the Institute of Science and Technology, The University of Michigan, Ann Arbor, 1972.

The Optimum Filters investigation is described in Section 4. This investigation led to the determination of the best pair of infrared filters for mapping $\%(SiO_2 - Al_2O_3)$ variations by means of an infrared ratio imaging technique developed earlier under this NASA task.

Section 5, entitled "Ratio Codes of Laboratory Data for Selected Ratios of the NASA/ERIM M-7 Airborne Scanner Channels," presents a new data compression technique designed to assist current efforts in interpretation of ratio images as well as future efforts concerned with the design of efficient ratio gating logic algorithms. Eleven of the 66 ratios (excluding reciprocals) achieved with the ERIM M-7 scanner in the 0.4-2.5 μm region (twelve channels) were calculated for approximately 235 laboratory spectra of soils, minerals, rocks, and some vegetation. The resulting ratios were divided into ten range intervals numbered from 0 through 9. Eleven single digits then make up the ratio code, which reduces the spectral shape information of a target reflectance spectrum to an 11-digit number. The ratio codes are useful for a priori selection of those ratio images which best enhance a particular target, in finding false alarm candidates for a specific target of interest, and possibly for training sets in automatic recognition map processors of the future.

Section 6 explains the preprocessing steps needed for ratio gating logic when laboratory or field spectra are to be used as training sets and suggests algorithm forms for a ratio gating logic system of the future. This system of logic is a possible candidate for on-board data processors of the future to be operated from either aircraft or space-shuttle platforms.

3
TWO MODELS FOR IRREGULAR ROCK AND MINERAL SURFACES

The problems encountered in geological remote sensing differ in several aspects from remote sensing problems concerning vegetative targets. First, temporal changes for geological targets are much slower than for vegetative ones. Second, for rock-type identification, variations in spectral emittance or reflectance are much more important than geometrical variations (in shape, shadowing, observation angle, etc.) across the scene, whereas both are relatively important for the identification of vegetative targets. Third, the thermal IR spectral region contains more information than the visible-reflective IR wavelength regions about the chemical composition of rocks, whereas the converse is true for vegetative targets.

Rocks and minerals present a special problem in the thermal IR region not normally encountered in the shorter wavelength regions. Thermal IR wavelengths ($\approx 10\mu$m) dimensionally approach the particle diameters of some of the grains in fine-textured rock surfaces, and this produces some complex optical phenomena related to surface roughness. For instance, Lyon [4] and other investigators have noted that the spectral emittance within the major reststrahlen bands (interatomic vibration modes in this case) of silicate rocks and minerals tends to increase with decreasing particle size. Later work [5] has shown that in spectral regions of moderate to small complex refractive index outside the reststrahlen bands (which are associated with a high complex refractive index), the emittance can either increase or decrease with decreasing particle size.

The dependence of spectral emittance on particle size is an important factor in geological remote sensing, because textural variations from rock to rock may mask differences in chemical composition, and vice versa. It is therefore necessary to separate,insofar as possible, the textural and chemical effects on the spectral emittance. To gain insight into this problem, a model of rough rock and mineral surfaces is sought which can at least qualitatively explain the effect of textural variations on the IR spectrum of those surfaces.

In last year's report for this task [2] two models were selected to describe qualitatively the effects of surface roughness on the infrared spectral emittance of rocks and minerals. Both models require the calculation of single-particle scattering parameters and emittance of a

4. Lyon, R. J. P., Evaluation of IR Spectrophotometry for Compositional Analysis of Lunar and Planetary Soils: Rough and Powdered Surfaces, Final Report, Part II, NASA Contract NASr-49(04), Stanford Research Institute,Menlo Park, 1964.

5. Vincent, R. K. and G. R. Hunt, Infrared Reflectance from Mat Surfaces, Applied Optics, Vol. 7, 1968, p. 53.

homogeneous, semi-infinite, optically thick "cloud" of particles with a radiative transfer model devised by Conel [6] and reviewed below. The contribution of this report is to extend Conel's theory to account for birefringence effects which, in the infrared wavelength region, are important for most natural geologic materials. The two methods selected for that purpose are described in Sections 3.2 and 3.3.

3.1 RADIATIVE TRANSFER MODEL

The radiative transfer model used here for calculation of emittance is the same as that used by Conel [6]. A plane-parallel "cloud" of infinite optical thickness consisting of uniform spherical particles of diameter d is assumed. The assumed anisotripic scattering phase function is

$$p = w_0[1 - w_1' \cos \theta] \tag{1}$$

where w_0 and w_1' are the single-particle scattering albedo and anisotropy factor, respectively, and θ is the angle between the incident and scattered wave normals. All three quantities are wavelength-dependent, but the λ subscript has been suppressed. The quantities w_0 and w_1' are calculable from Mie scattering theory as follows:

$$w_0 = \frac{Q_{sca}}{Q_{ext}} = \frac{\sum_{m=1}^{\infty} (2m + 1)\left[\left|a_m(\alpha, N)\right|^2 + \left|b_m(\alpha, N)\right|^2\right]}{\sum_{m=1}^{\infty} (2m + 1)R_e\left[a_m(\alpha, N) + b_m(\alpha, N)\right]} \tag{2}$$

$$w_1' = 3 <\cos \theta>$$

$$= \frac{\sum_{m=1}^{\infty} 6\left[\frac{m(m + 2)}{m + 1} R_e\left\{a_m(\alpha, N)a_{m+1}^*(\alpha, N)b_{m+1}^*(\alpha, N)\right\} + \frac{2m + 1}{m(m + 1)} R_e\left\{a_m(\alpha, N)b_m^*(\alpha, N)\right\}\right]}{\sum_{m+1}^{\infty} (2m + 1)\left[\left|a_m(\alpha, N)\right|^2 + \left|b_m(\alpha, N)\right|^2\right]} \tag{3}$$

6. Conel, J. E., Infrared Emissivities of Silicates: Experimental Results and a Cloudy Atmosphere Model of Spectral Emission from Condensed Particulate Mediums, J. Geophys. Res., Vol. 74, 1969, p. 1614.

where Q_{sca} = scattering efficiency factor

Q_{ext} = extinction efficiency factor

$\alpha = 2\pi d/\lambda$

and $a_m(\alpha, N)$ and $b_m(\alpha, N)$ are Mie coefficients which are functions of α and the complex index of refraction, $N = n - ik$, at that wavelength. After employing a simple two-point Gaussian quadrature method to solve the radiative transfer equation and then matching the proper boundary conditions at the cloud surface, as Conel did, one obtains for the spectral emittance

$$E = (1 - R) = \frac{2}{U + 1} \tag{4}$$

$$\text{where } U = \left[\frac{1 - w_o\left(\frac{w_1'}{3}\right)}{1 - w_o} \right]^{\frac{1}{2}}$$

Two qualifications to the theory should be mentioned here. Emission and reflection of the topmost layer of grains in the powder is neglected, so the E calculated from the above equation is a "bulk" emittance. Second, an n-point Gaussian quadrature method is used to replace an integral by a weighted sum of the integrand evaluated at n discrete points; for a two-point approximation, only one point in each hemisphere (forward- and backward-scattering directions) is selected. Therefore, the calculated emittance represents a rough approximation of the total hemispherical emittance. The emittance calculated for a "cloud" of particles is assumed to be approximately equal to the emittance of a rock surface, consisting of closely packed (touching) particles of the same uniform conposition as the "cloud" particles. This gross approximation can only be justified at this time by a "proof of the pudding" argument: it is a valid approximation if it yields valid results. Conel's work indicates that this approximation is qualitatively valid for granulated rock powders, and later results of this report also support the qualitative validity of this approximation.

Inputs to this model are particle diameter and complex refractive index as a function of wavelength. Here two complications arise. Rocks usually consist of mineral grains randomly oriented. But silicate and carbonate minerals, the most important constituents of igneous and sedimentary rocks, are birefringent in the thermal infrared wavelength region. This means that the complex index of refraction of a mineral crystal is dependent on the angle θ between the direction of propagation and the optical axis (or axes) of the crystal. These two directions define what is called a principal plane. Therefore, some accounting must be made for the birefringence of the randomly oriented mineral grains in the rock surface. The second complication

arises because, although some rocks are monomineralic, most rocks consist of several minerals. Therefore, the complex refractive indices of the individual minerals must be combined in some way to produce an effective index of refraction for a multimineralic rock.

There are two possible approaches to the above problems. One is to experimentally determine the refractive indices of the individual constituents and theoretically combine them to produce an effective refractive index. This approach is appealing only for the simplest cases. For instance, the effective index of a monomineralic rock consisting of uniaxial (one optical axis) crystals, such as nearly pure sandstone (primarily quartz) or limestone (calcite), may be described in terms of linear combinations of the ordinary ray (electric vector perpendicular to the principal plane and θ-independent) and extraordinary ray (electric vector parallel to the principal plane and θ-dependent) reflectances theoretically calculated for randomly oriented crystals in the rock surface. This approach is taken in Section 3.2, below. For more complex cases, where both birefringence and multiple minerals are present, a different approach is called for. It involves the calculation of effective indices from a spectral reflectivity measurement of the rock surface, which become inputs to the theory described by Eqs. (1-4). The resulting calculated reflectances or emittances, it is assumed, will then represent the optical properties of the complicated rock surface; this approach will be taken in Section 3.3.

3.2 THEORETICAL AVERAGING TO ACCOUNT FOR BIREFRINGENCE IN MONOMINERALIC ROCKS CONTAINING ONLY UNIAXIAL CRYSTALS

The first of these two approaches or models will be taken for the sedimentary rocks— sandstone (primarily quartz) and limestone (primarily calcite). Chert, also a sedimentary rock, is expected to be similar to sandstone in its spectral behavior because both contain high $\% SiO_2$. However, chert is noncrystalline, unlike quartz. Both quartz (SiO_2) and calcite ($CaCO_3$) are uniaxial minerals (one optical axis) for which the ordinary and extraordinary ray refractive indices are known, as described in two 1972 publications under this contract [1, 7]. The problem at hand is how to treat birefringence in a surface of randomly oriented uniaxial crystals or, in other words, how to combine the emissive effects of the ordinary and extraordinary complex indices of refraction to describe the emittance of the rock surface.

Conel ignored this problem by using, exclusively, the ordinary ray index of refraction to calculate emissivity spectra of quartz powders in a wavelength region where quartz is only weakly birefringent (ordinary and extraordinary indices approximately equal). Peterson and

7. Vincent, R. K., Emission Polarization Study on Quartz and Calcite, Applied Optics, Vol. 11, 1972, pp. 1942-45.

Weinman [8], in calculating the infrared scattering properties of quartz aerosols, accounted for birefringence by assuming that incident radiation was propagated as ordinary rays through 2/3 of the particles and as extraordinary rays through 1/3 of the particles. Consequently, they used these factors to linearly combine the ordinary and extraordinary extinction coefficients to thus obtain a total extinction coefficient. This is similar to the approximation made by Raman and Viswanathan [9] for a poly-crystalline medium composed of uniaxial crystals, which they based on the assumption that crystalline particles are identically aligned cubes with their edges parallel to principal axes of the crystal index ellipsoid. The average refractive index resulting from such an assumption is

$$\overline{N} = (2N_o' + N_e')/3 \tag{5}$$

where N_o' and N_e', respectively, are the complex principal ordinary and extraordinary indices of the uniaxial crystals comprising the medium. It is obvious, however, that any method which combines the ordinary and extraordinary indices prior to calculation of reflectance or emittance will be incorrect when the real parts of the two indices fall on opposite sides of 1.0, because reflectance increases as n departs from 1.0 in either direction, when air is the surrounding medium.

A theoretical method for treating birefringence for a homogeneous particulate surface composed of randomly oriented uniaxial crystals is now described in three steps. First the ordinary and extraordinary indices are averaged over all possible particle orientations to yield the two indices, $\overline{N}_o$ and $\overline{N}_e$, for an "average" particle orientation with respect to a given direction of light propagation. Secondly, emissivities are calculated for the particulate surface, using the theory discussed in the previous section, with the exclusive use of N_o and N_e to obtain $E(\overline{N}_o)$ and $E(\overline{N}_e)$, respectively. Finally, $E_o(\overline{N}_o)$ and $E_e(\overline{N}_e)$ are combined to obtain the total emissivity of the cloud from an expression of the form

$$E = P_o E_o(\overline{N}_o) + P_e E_o(\overline{N}_e) \tag{6}$$

where P_o and P_e (which will be called polarization fractions) have a sum equal to 1.

For the first step in this method, consider the case of radiation propagating inside a uniaxial crystal along the z-axis of an arbitrary XYZ coordinate system fixed in space. The optical axis $\vec{A}$ of the crystal, which defines the z' axis of the crystal's principal X'Y'Z' coordinate

8. Peterson, J. T. and J. A. Weinman, J. Geophys. Res., Vol. 74, 1969, p. 6947.

9. Raman, C. V. and K. S. Viswanathan, Proc., Ind. Acad. Sci., Vol. I, 1955, p. 37; reprinted in Handbuch der Physik, Vol. XXV, Ed., S. Flügge, Chapter 8, Crystal Optics; Diffraction, p. 122.

system, is described by a polar angle θ and azimuth angle ϕ (see Figure 1). The plane containing the propagation vector $\vec{I}$ and the optical axis A is called the principal plane. For any given direction of propagation $\vec{I}$ in a uniaxial crystal, there are two waves with different displacements $\vec{D}_0$ and $\vec{D}_e$ and different velocities V_0 and V_e allowed by the crystal.

Each velocity V_j is related to a complex index of refraction according to the equation

$$V_j = \frac{c}{N_j} = \frac{c}{n_j - ik_j} = \frac{c}{n_j(1 - iK_j)} \quad j = o \text{ or } e \tag{7}$$

For wavelength regions where k_0 and k_e are negligible, the "o" (ordinary) and "e" (extraordinary) refer respectively to vibrations perpendicular and parallel to the principal plane (linear polarization). This special definition of ordinary and extraordinary vibrations is not valid, however, whenever k_0 and k_e are significantly large since, in that case, $\vec{D}_0$ and $\vec{D}_e$ are no longer perpendicular to $\vec{I}$ (elliptical polarization).

The two phase velocities associated with a given value of θ are given by

$$V_0^2 = V_0'^2 \tag{8a}$$

and

$$V_e^2 = V_0'^2 \cos^2\theta + V_e'^2 \sin^2\theta \tag{8b}$$

where the primed and unprimed velocities refer respectively to values of velocity for $\theta = 90°$ and $\theta \neq 90°$. These primed velocities and their corresponding complex refractive indices will be referred to as "principal ordinary" and "principal extraordinary" because, for $\theta = 90°$, the XYZ system becomes the X'Y'Z' principal coordinate system of the uniaxial crystal.

Substitution of Eq. (7) into Eqs. (8a and b) yields

$$\frac{1}{n_0^2(1 - iK_0)^2} = \frac{1}{n_0'^2(1 - iK_0')^2} \tag{9a}$$

and

$$\frac{1}{[n_e(\theta)]^2[1 - iK_e(\theta)]^2} = \frac{\cos^2\theta}{n_0'^2(1 - iK_0')^2} + \frac{\sin^2\theta}{n_e'^2(1 - iK_e')^2} \tag{9b}$$

Equation (9a) states that the ordinary complex index of refraction is the same for all directions of propagation, i.e., $N_0 = N_0'$. Equation (9b), however, expresses the angular dependency of the extraordinary complex index of refraction. When Eq. (9b) is separated into real and imaginary parts and solved for $n_e'(\theta)$ and $K_e'(\theta)$, the results are
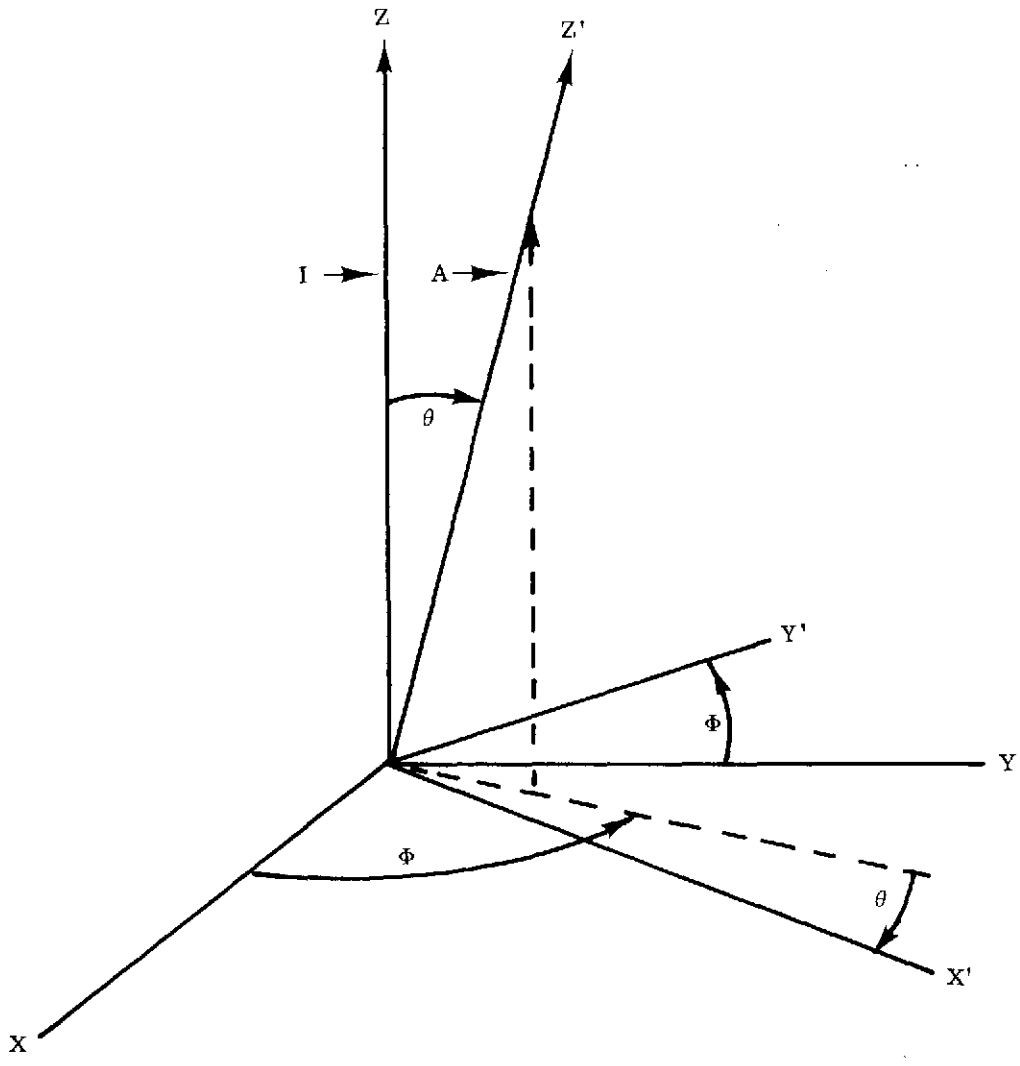
FIGURE 1. RELATION BETWEEN THE FIXED SPATIAL (XYZ) AND
THE PRINCIPAL (X'Y'Z') COORDINATE SYSTEMS IN A UNIAXIAL
CRYSTAL. I = radiation propagation direction. A = optical axis of
the crystal.

$$n_e(\theta) = \frac{M_1}{\left[\frac{1}{2}\left(M_2^2 + 4M_1^2\right)\left(\sqrt{M_2^2 + 4M_1^2} - M_2\right)\right]^{1/2}}$$ (10a)

and

$$K_e(\theta) = \frac{\sqrt{M_2^2 + 4M_1^2} - M_2}{2M_1}$$ (10b)

where

$$M_1 = \frac{n_o' k_o'}{\left(n_o'^2 + k_o'^2\right)^2} \cos^2 \theta + \frac{n_e' k_e'}{\left(n_e'^2 + k_e'^2\right)^2} \sin^2 \theta$$

and

$$M_2 = \frac{n_o'^2 - k_o'^2}{\left(n_o'^2 + k_o'^2\right)^2} \cos^2 \theta + \frac{n_e'^2 - k_e'^2}{\left(n_e'^2 + k_e'^2\right)^2} \sin^2 \theta$$

and

$$k_j' = n_m' K_j'$$

Equations (9) and (10), therefore, define the two complex indices of refraction associated with monochromatic radiation propagating at an angle θ with respect to the optic axis in an uniaxial crystal. These equations are valid for any positive real values of the principal indices n_o', k_o', n_e', and k_e'.

Now that N_o and N_e have been derived to describe interaction of an incident ray with a single crystalline particle, one can consider the case of a beam of incident radiation striking a homogeneous "cloud" of uniaxial crystals in which it is reasonable to assume that the particles are randomly oriented. This is the case except when the uniaxal crystal of interest has strongly preferred cleavage planes, and the macroscopic surface of the "cloud" is packed such that the preferred cleavage plane of the individual particles has a preferred orientation with respect to the incident beam. For any given direction of the incident beam propagating through a cloud of randomly oriented uniaxial crystals, the two effective complex refractive indices can be represented by the expressions

$$\overline{N}_o = \overline{n}_o - \overline{ik}_o = \frac{1}{2}\left[\int_0^\pi n_o' \sin \theta \, d\theta - i\int_0^\pi n_o' K_o' \sin \theta \, d\theta\right] = N_o'$$ (11a)

$$\overline{N}_e = \overline{n}_e(\theta) - \overline{ik}_e(\theta) = \frac{1}{2}\left[\int_0^\pi n_e(\theta)\sin\theta\,d\theta - i\int_0^\pi n_e(\theta)K_e(\theta)\sin\theta\,d\theta\right] \qquad (11b)$$

When Eq. (10) is substituted into (11b), the resulting integrals can be integrated by the Simpson rule to yield $\overline{N}_e$. It is clear from Eqs. (10) and (11) that the principal ordinary complex re-fractive index has an effect on both $\overline{N}_o$ and $\overline{N}_e$, whereas the principal extraordinary index effects only $\overline{N}_e$.

In general, the polarization fractions, P_o and P_e, as defined by Eq. (6) are probably wavelength-dependent. For this report, however, the simplest approximation will be made, that $P_o = P_e = 1/2$. This is consistent with the assumption that the particles are randomly oriented.

This method of accounting for birefringence effects on the spectral emittance of rough surfaces in monomineralic rocks consisting of uniaxial crystals has been applied to quartz and calcite. For quartz, the theoretically calculated spectral emittance for a particulate surface consisting solely of 125μm-diameter grains is compared in Figure 2 with an experimentally measured emittance of quartz powder with particles in the 74-250 μm range. Actually, some particles smaller than 74μm were present in the experimental sample, adhering to larger particles, because the quartz was not washed after grinding. In Figure 2, curve A is the experimental emittance [5] from a non-quantitative measurement, i.e., the emittance values were not calibrated to an absolute scale. Data near the 670cm^{-1} atmospheric CO_2 band have been omitted. Curve B is the theoretical curve calculated from Eqs. (11), (4), and (6), where it was assumed that $P_e = 1/2$ and $P_o = 1/2$. Curve C is the spectral emittance for $P_e = 0$, $P_o = 1$. Local emittance maxima frequency ($\nu = 10,000/\lambda$, with frequency in wavenumbers, or cm^{-1}, and wave-length in μm) positions of curve B agree within 5cm^{-1} of the maxima in experimental curve A.

The assumption that P_e and P_o are independent of wavelength is only an approximation, as pointed out earlier. The values of $P_e = P_o = 1/2$ are significant only if they can be used to ob-tain reasonably good qualitative theoretical emittance spectra for other particle diameters of quartz and for other minerals besides quartz. With these same values of $P_e = P_o = 1/2$, the theoretical spectrum for a particulate surface composed entirely of 30-μm-diameter quartz crystals was calculated. The result is shown as curve B of Figure 3. Curves C and D are once again the extraordinary ($P_e = 1$, $P_o = 0$) and ordinary ($P_e = 0$, $P_o = 1$) emittance spectra, re-spectively. The experimental spectrum shown as curve A is taken from quantitative total
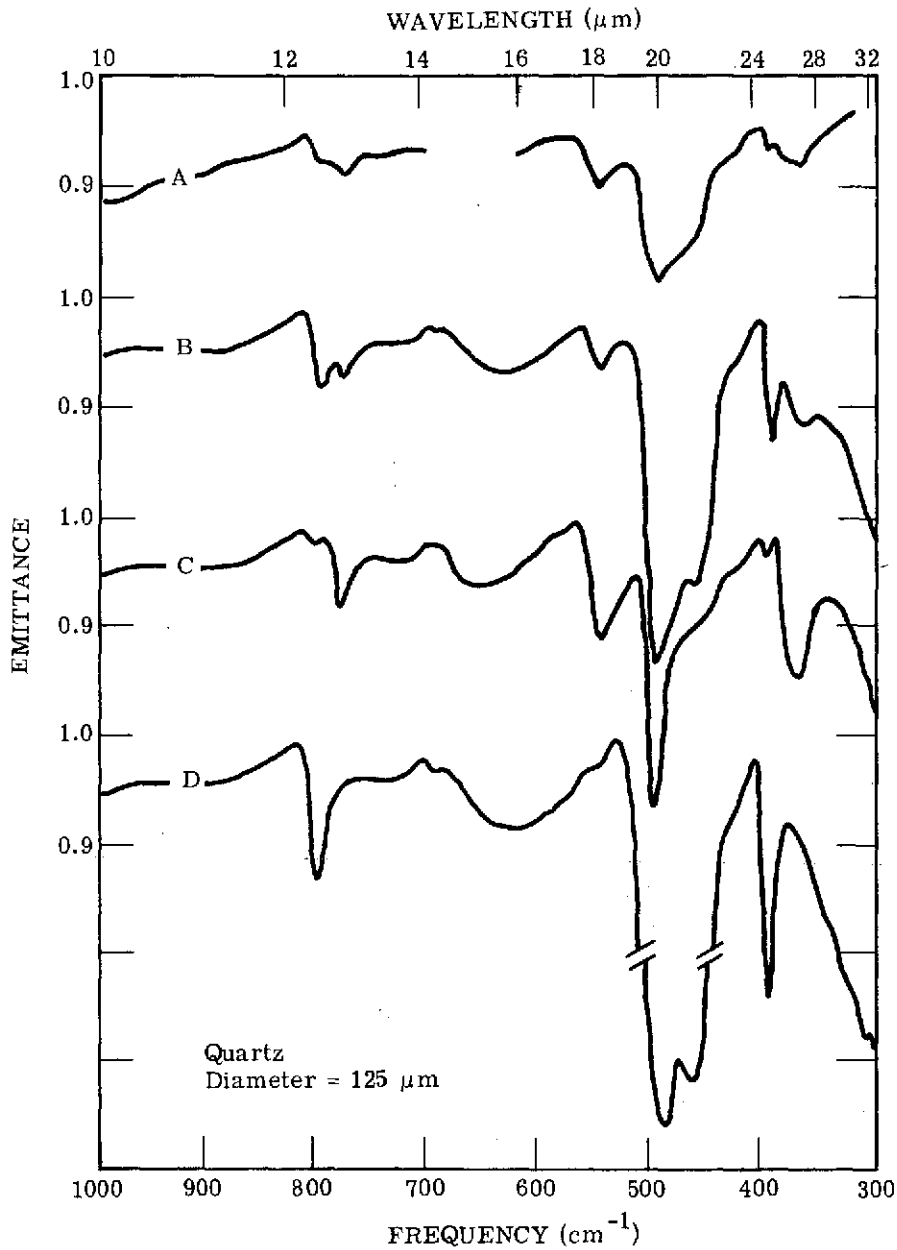
FIGURE 2. CALCULATED AND EXPERIMENTAL SPECTRAL
EMITTANCE OF QUARTZ FOR A 125-μm PARTICLE DIAMETER.
Curve A is an experimental spectrum for 74- to 250-μm quartz
powder. Curves B, C, and D are theoretical spectra for an assumed
quartz particle diameter of 125 μm and emittances $E_B = [E_0(N_0^t)$
$+ E_e(\overline{N}_e)] /2$, $E_C = E_e(\overline{N}_e)$, and $E_D = E_0(N_0^t)$. Slashes in Curve D
denote a vertical discontinuity of 0.1 in emittance.

WAVELENGTH (μm)
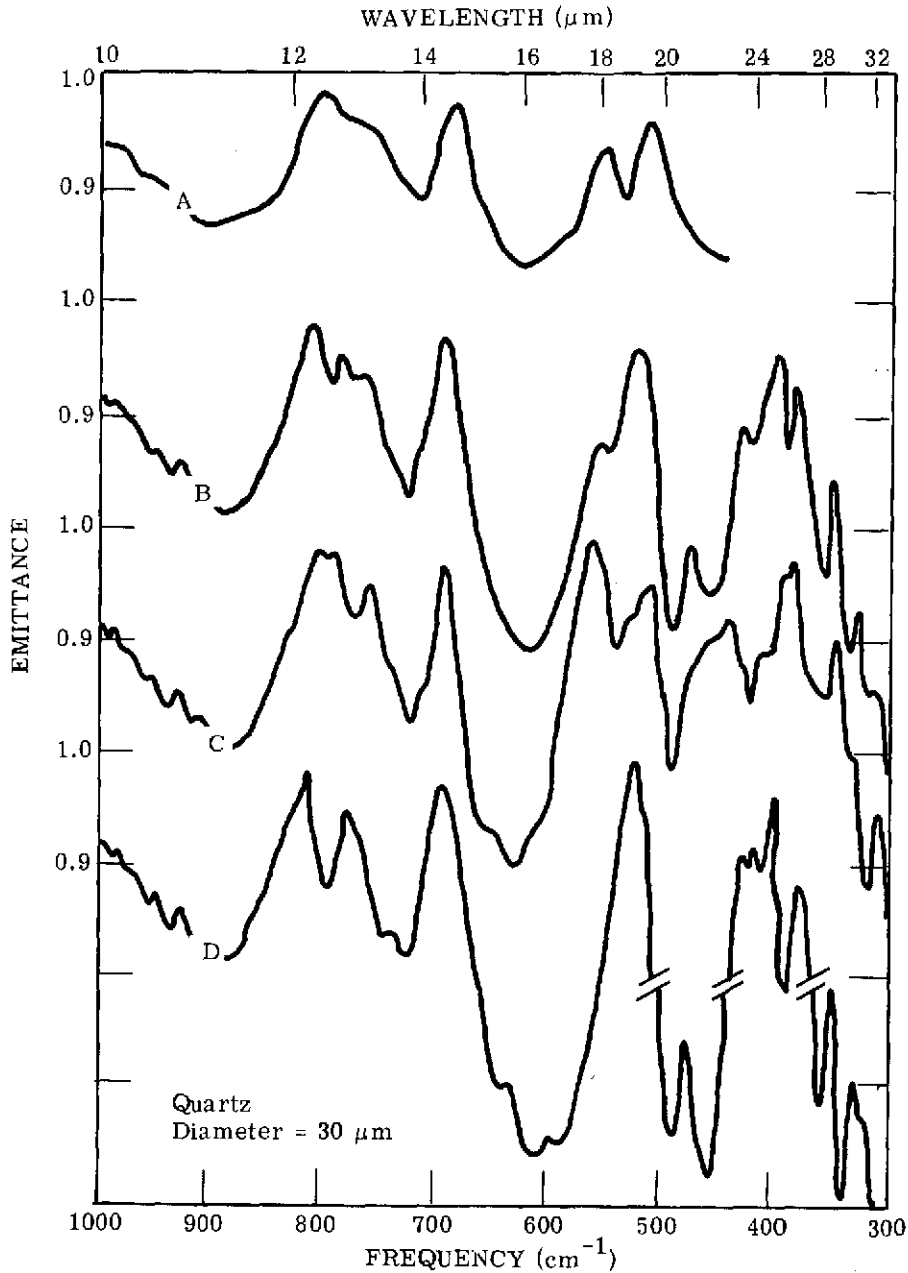
FIGURE 3.   CALCULATED AND EXPERIMENTAL SPECTRAL EMITTANCE OF
QUARTZ FOR A 30-μm PARTICLE DIAMETER. Curve A is an experimental quan-
titative reflectance spectrum plotted as $E_A = 1 - R_A$ for a quartz powder of 0- to
37-μm diameter. Curves B, C, and D are theoretical spectra for an assumed
quartz particle diameter of 30 μm and emittances $E_B = [E_0(N_0') + E_e(\overline{N}_e)]/2, E_C = E_e$
$(\overline{N}_e)$, and $E_D = E_0(N_0')$. Slashes in Curve D denote a vertical discontinuity of 0.1 in
emittance.

reflectance data (plotted as E = 1 - R) measured for J. E. Conel [10] at the National Bureau of Standards. The quartz powder had a particle size range from $0-37\,\mu$m and the reflectance measurements were made in a total integrating sphere apparatus attached to a Cary-White model 90 spectrophotometer. The sample was baked at 200°C for 8 hours in a dry nitrogen atmosphere to eliminate free water in the powder, then cooled to room temperature for the reflectance measurements.

Except for the region below 500cm^{-1} where the spectrophotometer is less sensitive, the calculated curve B of Figure 3 qualitatively matches curve A surprisingly well, given the fact that such gross approximations have been made throughout the development of this theoretical model. The local emissivity maxima in curve B are all within 10cm^{-1} of the maxima in curve A; however, the curve A maxima are systematically 5 to 10 cm^{-1} lower in frequency than the curve B maxima. This minor discrepancy may be caused by improper instrument calibration. In both Figures 2 and 3 the discrepancies between curves B and A near 500cm^{-1} can be at least partially explained by the fact that the quartz indices are least accurate in this vicinity.

The selection of $125\,\mu$m and $30\,\mu$m as the theoretical particle diameters to represent the 74-250 μm and 0-37 μm samples is not a critical assumption, except that particle diameters less than about $5\,\mu$m begin to yield more nearly a blackbody emissivity spectrum as particle diameter approaches zero. Any diameters within roughly 33% of the two respective chosen values produce spectral emittance curves which fit the experimental data about as well as curves B of Figures 2 and 3.

Before leaving the quartz case, it is instructive to compare the spectral emittances calculated above with those calculated directly from Eq. (4), after a linear combination of indices (such as Eq. 5). Figure 4 shows theoretical spectral emittance curves for a particle diameter of $125\,\mu$m which were calculated from Eq. (4) using the following linear combinations of principal ordinary and extraordinary rays: $\overline{N} = (2N'_o + N'_e)/3$ (curve B) and $\overline{N} = (N'_o + N'_e)/2$ (curve C). Curve D shows the results of combining the averaged extraordinary index from Eq. (11b) with the principal ordinary index $\overline{N} = (N'_o + \overline{N}_e)/2$. Curve A of Figure 4 is the same as experimental curve A shown earlier in Figure 2.

It is clear that curves B and C, which employ direct combinations of the principal indices, are quite inaccurate in the $300-500\ \text{cm}^{-1}$ and $750-800\ \text{cm}^{-1}$ regions. Curve D, which employs an averaged extraordinary index, is somewhat more similar to experimental curve A, but is obviously wrong in the vicinity of $470\ \text{cm}^{-1}$. Herein lies the aforementioned objection to the

10. Conel, J. E., Jet Propulsion Laboratory, Pasadena, Private Communication to R. K. Vincent, Willow Run Laboratories of the Institute of Science and Technology, The University of Michigan, Ann Arbor, 1970.
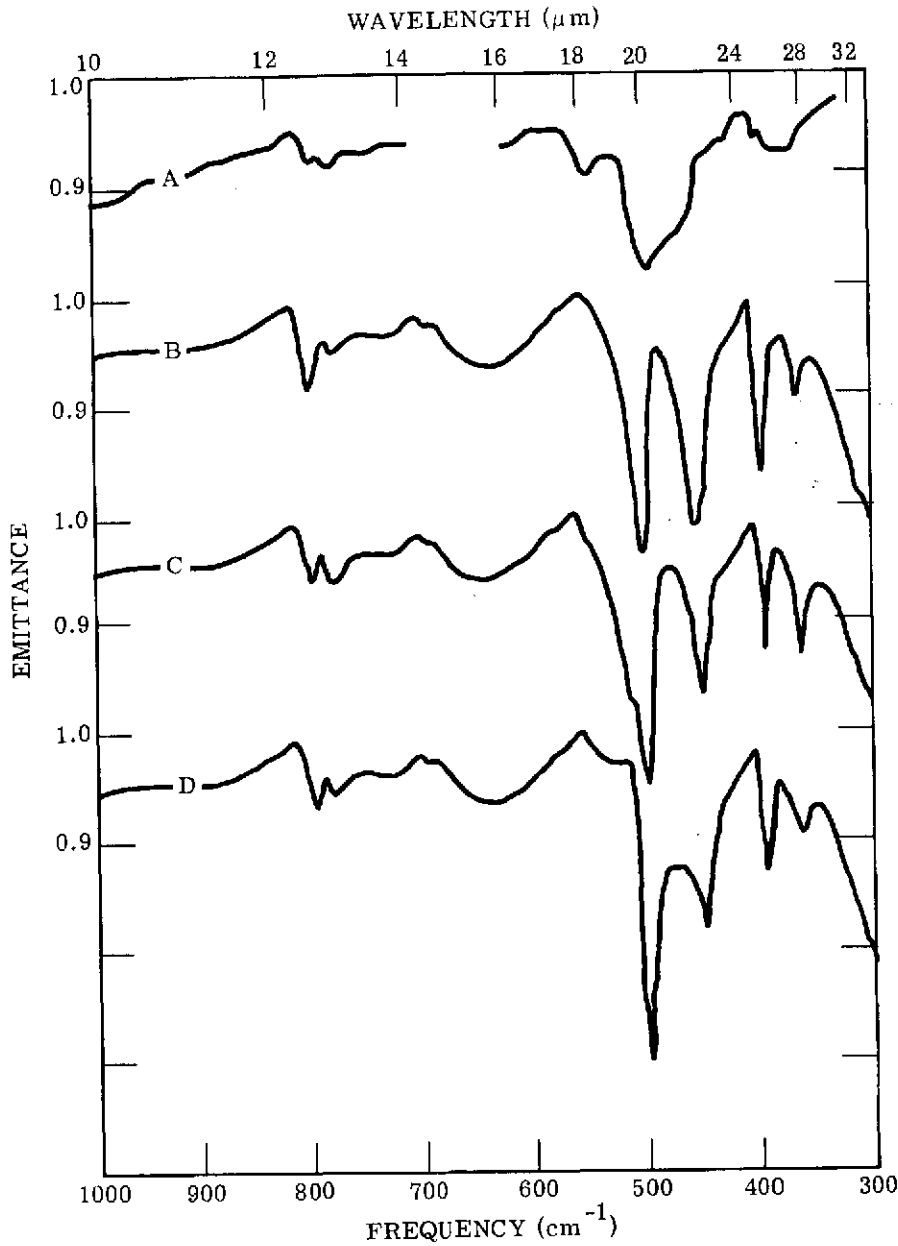
FIGURE 4. CALCULATED AND EXPERIMENTAL SPECTRAL
EMITTANCE OF QUARTZ FOR A 125-μm PARTICLE DIAM-
ETER—CALCULATED DIRECTLY FROM EQ. (4). Curve
A is an experimental spectrum for 74- to 250-μm quartz powder.
Curves B, C, and D are theoretical spectra for an assumed quartz
particle diameter of 125 μm. Average refractive index

$$N_B = (2N_0' + N_e')/3$$

$$N_C = (N_0' + N_e')/2$$

$$N_D = (N_0' + \bar{N}_e)/2$$

average index method: there are regions of the spectrum where one of the component indices is greater than 1.0 when the other is less than 1.0, which means that the index of a medium more optically dense than air is added to one that is less optically dense than air, resulting in an erroneous average index. A simple analogy of how such an error arises can be drawn from the normal-incidence Fresnel reflectivity equation, where the reflectivity for $N = n$ is equal to the reflectivity calculated for $N = 1/n$ in regions where k is negligible. If a medium of index $N = 0.5$ is mixed with a medium of index $N = 2.0$, the Fresnel reflectivity of the combined medium is the same as that for either of the two media before mixing—namely, 0.111. A linear combination of the two indices, however, would produce an average index of the medium somewhere between 0.5 and 2.0, which yields a Fresnel reflectivity lower than the correct value of 0.111. A comparison of Figures 4 and 2 shows that a linear combination of emittances works better than a linear combination of indices for uniaxial crystals.

The particulate surface model described for monomineralic rocks has produced qualitatively valid emittance spectra for two quite different particle diameter samples of the same mineral. The next question to be answered is whether the same theory can be used for other uniaxial minerals. Accordingly, Eqs. (11, 4, 6) were used to calculate the spectral emittance for calcite, with the same two particle diameters as were used for quartz. Figures 5 and 6 show those results. Curve A in Figure 5 is a nonquantitative experimental reflectance curve [5] plotted as $E_\lambda = 1 - R_\lambda$ for a calcite powder with a 74-250 μm particle diameter range; curve B is the theoretically calculated spectral emittance for a particle diameter of 125μm and $P_e = P_o = 1/2$. Figure 6 shows the same information for a nonqualitative experimental curve A [5] with a sample of 0-74 μm particle diameter range; and for the theoretical curve B, calculated with an assumed particle diameter of 30μm and $P_e = P_o = 1/2$.

The spectral features near 960cm^{-1} and 775cm^{-1} seen on both experimental A-curves (Figs. 5 and 6) are overtone and combinational bands not accounted for theoretically because they are too weak to show up in reflectance from a polished surface of calcite from which the indices of refraction are calculated. For this reason the theoretical curve does not include these two features. The theoretical B-curves of Figures 5 and 6 exaggerate the regions of low emittance (near 1000cm^{-1} and 775cm^{-1}) in a way similar to that noted previously in the quartz theoretical spectra.

Qualitatively, however, the model has predicted the spectral feature changes produced solely by varying particle diameter for two minerals of quite different compositions. The fact that the same model can be used to predict these qualitative spectral changes for different particle sizes of different minerals lends credence to the model, in spite of the gross approximations that were made in order to produce tractable results.

WAVELENGTH (μm)

CALCITE
Theoretical Curve for 125-μm Particle Diameter
Experimental Curve for 74- to 250-μm Powder

FREQUENCY (cm⁻¹)
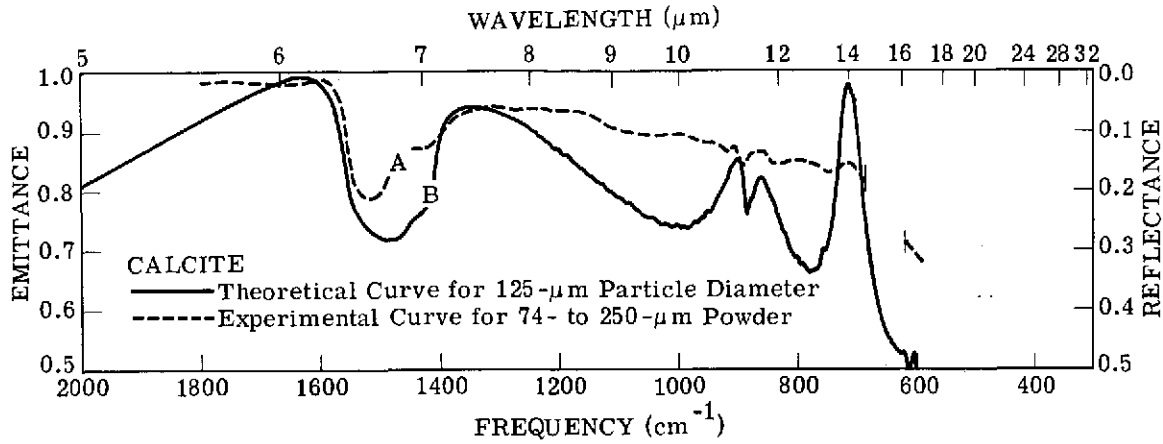
FIGURE 5. CALCULATED AND EXPERIMENTAL SPECTRAL EMITTANCES OF CALCITE
FOR A 125-μm PARTICLE DIAMETER

WAVELENGTH (μm)

CALCITE
Theoretical Curve for 30-μm Particle Diameter
Experimental Curve for 0- to 74-μm Powder

FREQUENCY (cm⁻¹)
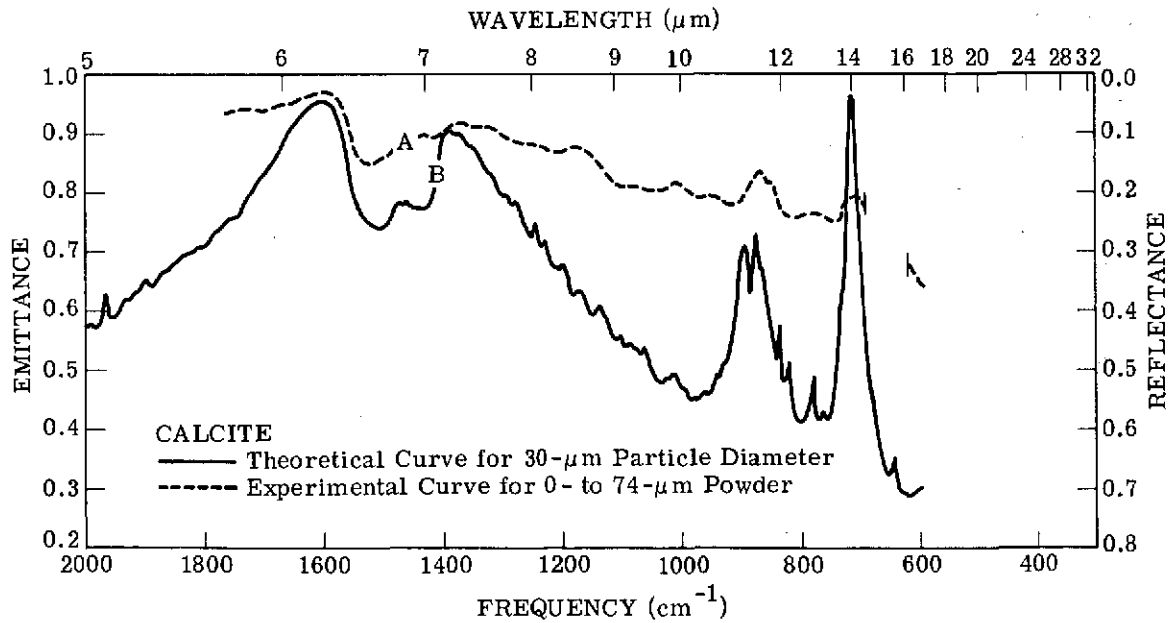
FIGURE 6. CALCULATED AND EXPERIMENTAL SPECTRAL EMITTANCES OF CALCITE
FOR A 30-μm PARTICLE DIAMETER

26

The simplifying assumption $P_e = P_o = 1/2$ has been made for both particle sizes of quartz and calcite. Visual reinspection of Figures 2 and 3 will show that for quartz, a slightly better qualitative fit with experimental data in the region near $550 cm^{-1}$ may be obtained by weighting P_e more heavily (up to about $P_e = 2/3$, $P_o = 1/3$). However, since this would seem to imply some preferential orientation of the quartz particles in the experimental sample, and since the theoretical calcite spectra are not improved by weighting the extraordinary component more heavily, no better values of P_e and P_o were sought in this investigation.

Some previously hypothesized [5] generalizations about the effect of particle size (or surface roughness) on spectral emittance are supported by the quartz and calcite results. Table 1 lists oscillator parameters for some of the quartz [11] and calcite [7] bands mentioned in the following discussion. Strong reststrahlen bands, with strengths greater than approximately 0.50, tend to retain their appearance as emittance minima with decreasing particle diameters, at least down to a diameter of $30 \mu m$. The $1072 cm^{-1}$ and $1080 cm^{-1}$ bands of quartz are not shown in Figures 2-4 because the results are almost identical to those of Conel [6] in that spectral region of relatively low birefringence. Intermediate bands, where the strength is around 0.1, display a peculiar change from emittance minima to apparent emittance maxima with a reduction in particle diameter from $125 \mu m$ to $30 \mu m$. Weak bands, with strengths on the order of 0.01, retain their appearance as emittance maxima for both particle diameters. Though these three types of spectral behavior have been experimentally observed [5] previously, the model predictions verify that the spectral emittance in the wavelength vicinity of intermediate bands can change from peak to trough with only a change in particle diameter. The peculiar experimental spectral features are not artifacts.

Conel's results for the 1000-1250 cm^{-1} region (8-10 μm) of quartz and the results of this study for calcite in the 1560-1430 cm^{-1} (6.4-7.0 μm) region show that in the strong reststrahlen regions, a reduction of particle diameter from coarse ($> 125 \mu m$) to fine-grained ($\approx 30 \mu m$) surfaces does not alter the spectral features a great deal. For loosely packed ultrafine-grained surfaces, where particle diameters can be on the order of $< 5 \mu m$, however, even the strong reststrahlen bands may change appreciably.

Conclusions of this section relating to geological remote sensing are deferred to Section 3.4, where results from this and the now following Section (3.3) will be discussed together.

11. Spitzer, W. G., and D. A. Kleinman, Infrared Lattice Bands of Quartz, Phys. Rev., Vol. 121, 1961, p. 1324.

TABLE 1. OSCILLATOR PARAMETERS OF SOME QUARTZ
AND CALCITE INTERATOMIC VIBRATION MODES

Type	Material	Component	Frequency (ν in cm^{-1})	Strength ($4\pi\rho$)	Width (γ)
Strong	Quartz	Ordinary	1072	0.67	0.0071
Strong	Quartz	Extraordinary	1080	0.67	0.0069
Strong	Quartz	Ordinary	450	0.82	0.0090
Strong	Quartz	Extraordinary	495	0.66	0.0090
Strong	Calcite	Ordinary	1404	0.57	0.0069
Interme-diate	Quartz	Ordinary	797	0.11	0.0090
Interme-diate	Quartz	Extraordinary	779	0.10	0.0100
Interme-diate	Calcite	Extraordinary	870	0.08	0.0016
Weak	Calcite	Ordinary	711	0.01	0.0033

3.3 EXPERIMENTAL AVERAGING TO ACCOUNT FOR BIREFRINGENCE AND COMPOSI-
TIONAL INHOMOGENEITY IN MULTIMINERALIC OR MONOMINERALIC ROCKS
CONTAINING BIAXIAL AND/OR UNIAXIAL CRYSTALS

The theory covered in the preceding section for monomineralic rocks containing only uni-
axial crystals is sufficiently complicated to discourage efforts toward applying it to complex
rocks. Therefore, a simpler approach will be taken for the general case of multimineralic rocks
containing both biaxial and uniaxial minerals. Instead of trying to calculate the indices of re-
fraction of each mineral (with as many as three indices per mineral), an effective complex index
of refraction will be calculated for the whole rock via the following five-step procedure. First,
a surface of the rock sample is cut and polished. It will be assumed that within the area of the
polished surface being measured, all minerals comprising the rock are represented in cross
section in the same relative proportions as their volume percentages in the rock, and that the
crystals of each mineral are randomly oriented in the polished cross section. Second, a re-
flectivity spectrum is measured for near-normal incidence. Third, a classical oscillator fit-
ting program [1, 7, 11] is used to calculate the indices of refraction, whereby the spectral re-
flectivity curve is treated in the same manner as if it were a curve from a single, nonbirefrin-
gent crystal. Fourth, the resulting oscillator constants are used to generate an effective index
of refraction for the rock. Finally, the effective refractive index is input to the Mie scattering
and radiative transfer model of Conel's (described earlier in Section 3.1) which yields a cal-
culated emittance spectrum. The difference between the procedures of this and the previous
section is that there the averaging for birefringence effects was done theoretically, starting
from the actual refractive indices of a single crystal of the rock or mineral, whereas in this
section the averaging for both birefringence and multimineralogy is done with one experimental
measurement.

The first two rocks chosen as test cases were limestone (mostly calcite and dolomite) and
chert (accreted SiO_2; quartz is crystalline SiO_2) because they have simple compositions, which
are similar to the subjects (calcite and quartz) of the previous section, and because near-normal-
incidence spectral reflectivity curves of smooth surfaces of these rocks were already available
in ERSIS. Figure 7 shows the spectral reflectivity curves for smooth surfaces of both lime-
stone [12] and chert [4], ERSIS curve numbers B07139014 and B02131005, respectively.

The Manitou limestone curve was difficult to fit with the classical oscillator program, be-
cause the data do not extend to sufficiently low wavelengths to include all major carbonate

---

12. Martin Marietta Corp., Application of Remote Sensor Data to Geologic and Economic
Analysis of the Bonanza Test Site, Colorado, First Year Summary Report, Denver, 1970.

reststrahlenfeatures near 6.6μm. Figure 8 shows the calculated effective refractive index of Manitou limestone. The spectral region below 8μm is inaccurate for the previously stated reason. With this index of refraction, the procedure prescribed above yielded the calculated spectral emittance curves of Manitou limestone shown in Figure 9 for particle sizes 125μm, 30μm, and 1μm. Also included are the laboratory data for calcite reported earlier, though these lab data are not quantitatively accurate in that their emittance values are not absolute. Data for wavelengths greater than 8μm are encouraging in that they are not as exaggerated as the theoretical curves of the previous section, and clearly show the reversal of the spectral feature near 11.2μm from emittance minimum (for 125μm particles) to emittance maximum (for 1μm particles). Some of the discrepancy between experimental and theoretical curves in Figure 9 concerning the exact positions of the spectral features near 11.2μm and 14μm is most likely caused by differing chemical compositions between the lab sample represented by the experimental curves in Figure 9 and the limestone sample used to calculate the theoretical curves in the same figure. The lab sample was pure calcite, whereas the Manitou limestone, because the spectral features in Figure 7 appear at 11.2μm and 14μm, is suspected to have been strongly dolomitized. Dolomite is $CaMg(CO_2)$ whereas pure limestone is $CaCO_3$; substitution of the Mg ion for the Ca ion (dolomitization) causes the spectral feature to occur at lower wavelengths than the 11.4μm position of the $CaCO_3$ feature. However, the 30μm-diameter calculated curve does not show as much reversal as the $0-37\mu$m experimental curve, for which no explanation is apparent.

Figure 10 shows the calculated refractive indices for fine-grained chert. Figure 11 shows spectral emittance curves of chert (calculated by the same procedure) for particle sizes 125μm, 30μm, and 1μm. Also included are the laboratory spectra (not quantitatively accurate) reported in the previous section for quartz. Once again the theoretical spectra are not as exaggerated as in the previous section, and the apparent reversal in the 12-13 μm wavelength region from emittance minimum (for 125μm particle size) to apparent maximum (for 30μm particle size) is correctly predicted. The calculated results could not be performed for longer wavelengths because the reflectivity data in Figure 7 do not go past 13μm.

The above results for chert and, to a lesser degree limestone, are encouraging. The calculated curves correctly predict the effect of particle size on the spectral emittance, except for perhaps the 30μm curve of limestone. The extent of agreement between calculated and experimental curves is remarkable when one takes two factors into account: different samples were used to produce the two curves for each rock type, and seemingly gross approximations were made in producing the theoretical curves. The most serious discrepancy is the difference in wavelength positions of the 11.2μm and 13.8μm limestone spectral features between the experimental and calculated curves. The explanation given, that the Manitou limestone sample is
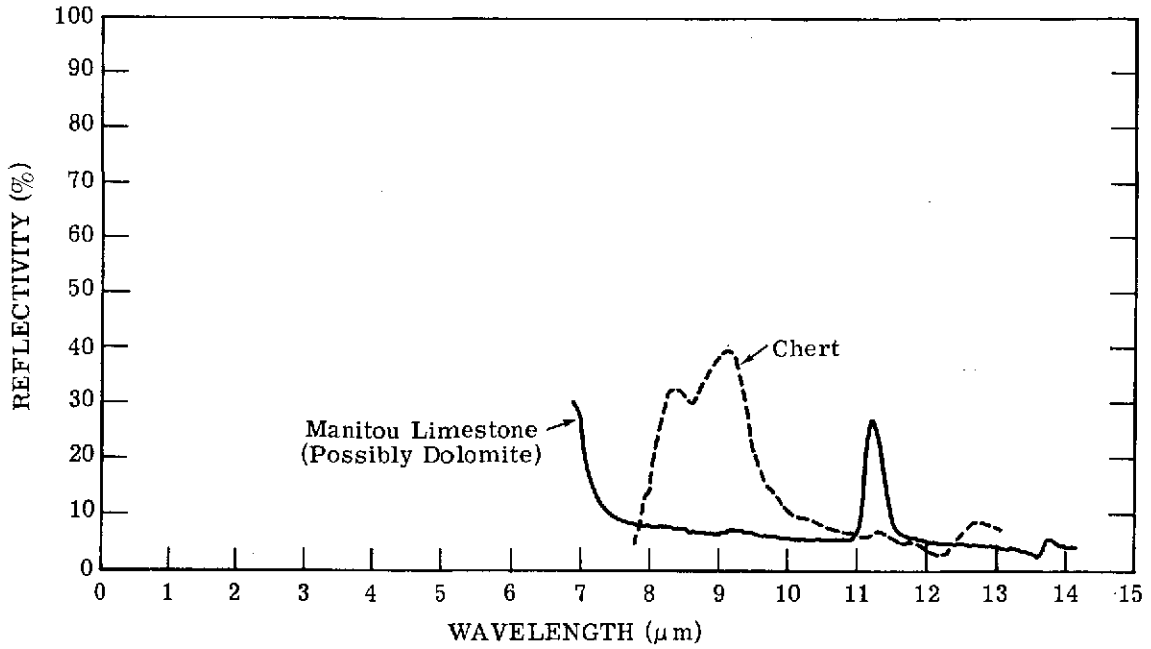
FIGURE 7. EXPERIMENTAL REFLECTIVITIES OF POLISHED SURFACES OF MANITOU
LIMESTONE AND CHERT
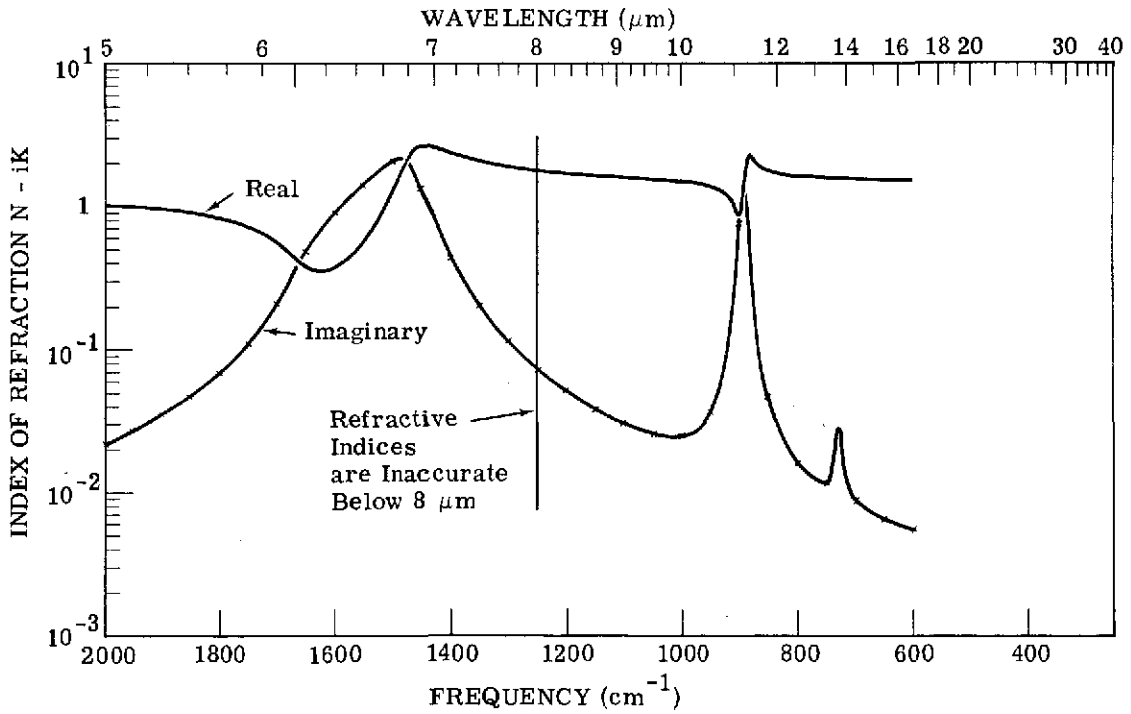
FIGURE 8. EFFECTIVE COMPLEX INDEX OF REFRACTION OF MANITOU LIMESTONE

31

WAVELENGTH (μm)

Experimental Curve for 74- to 250-μm Calcite Sample

Theoretical Curve for 125-μm Particle Diameter

FREQUENCY (cm^{-1})

(a) Diameter = 125.0 μm

WAVELENGTH (μm)

Theoretical Curve for 30-μm Particle Diameter

Experimental Curve for 0- to 37-μm Calcite Sample

FREQUENCY (cm^{-1})

(b) Diameter = 30.0 μm

WAVELENGTH (μm)

Theoretical Curve for 1-μm Particle Diameter

Reflective Indices
Inaccurate Below 8 μm

FREQUENCY (cm^{-1})
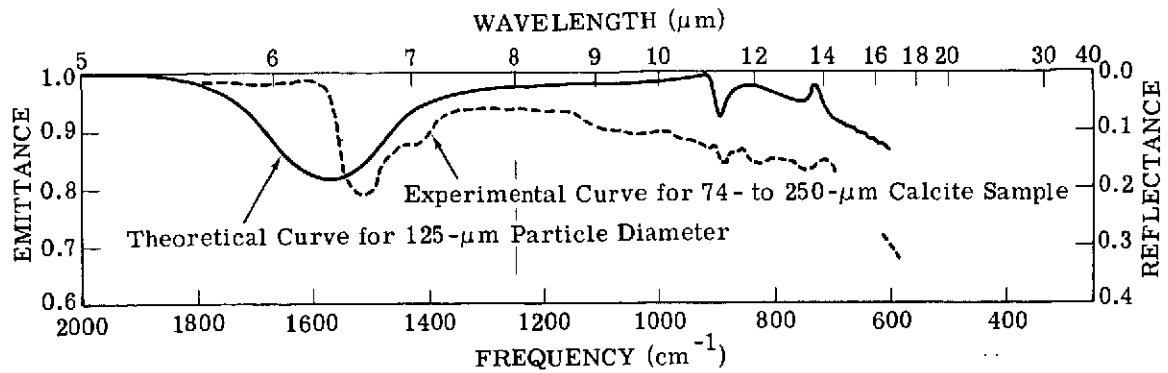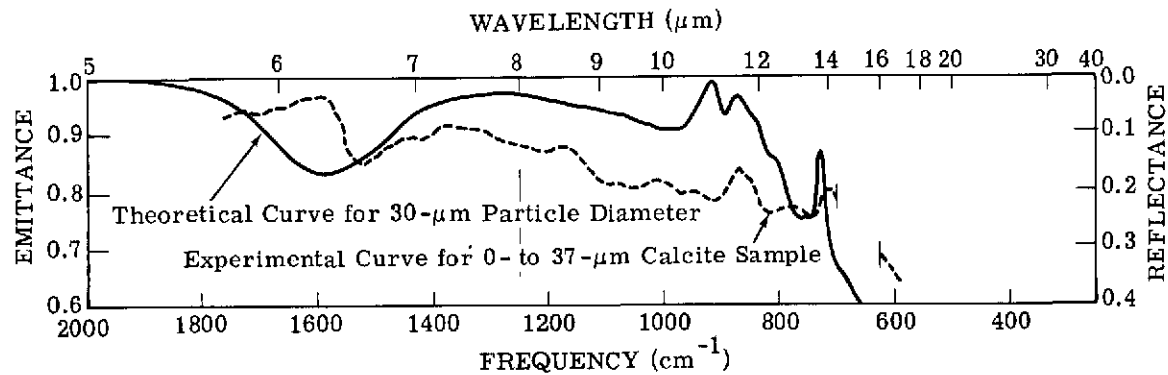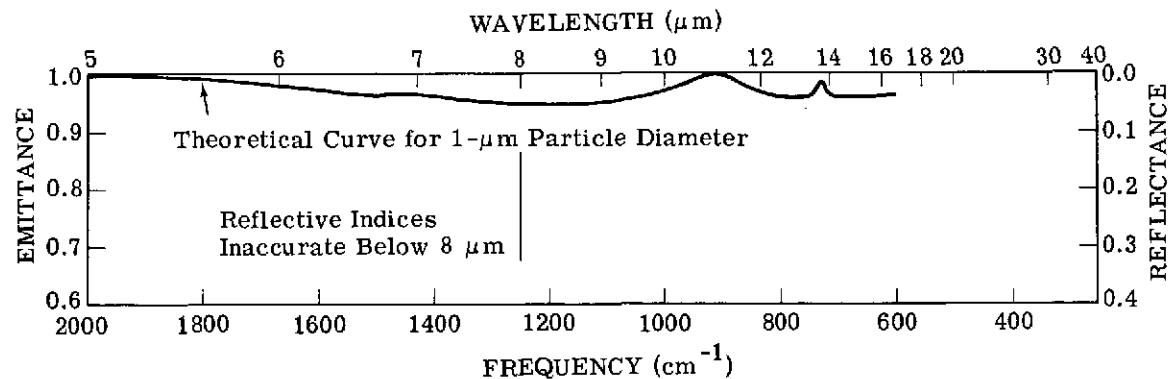
(c) Diameter = 1.0 μm

FIGURE 9. THEORETICAL SPECTRAL EMITTANCES OF MANITOU LIMESTONE (3 PARTICLE DIAMETERS) AND EXPERIMENTAL REFLECTANCES OF CALCITE (2 PARTICLE DIAMETERS)
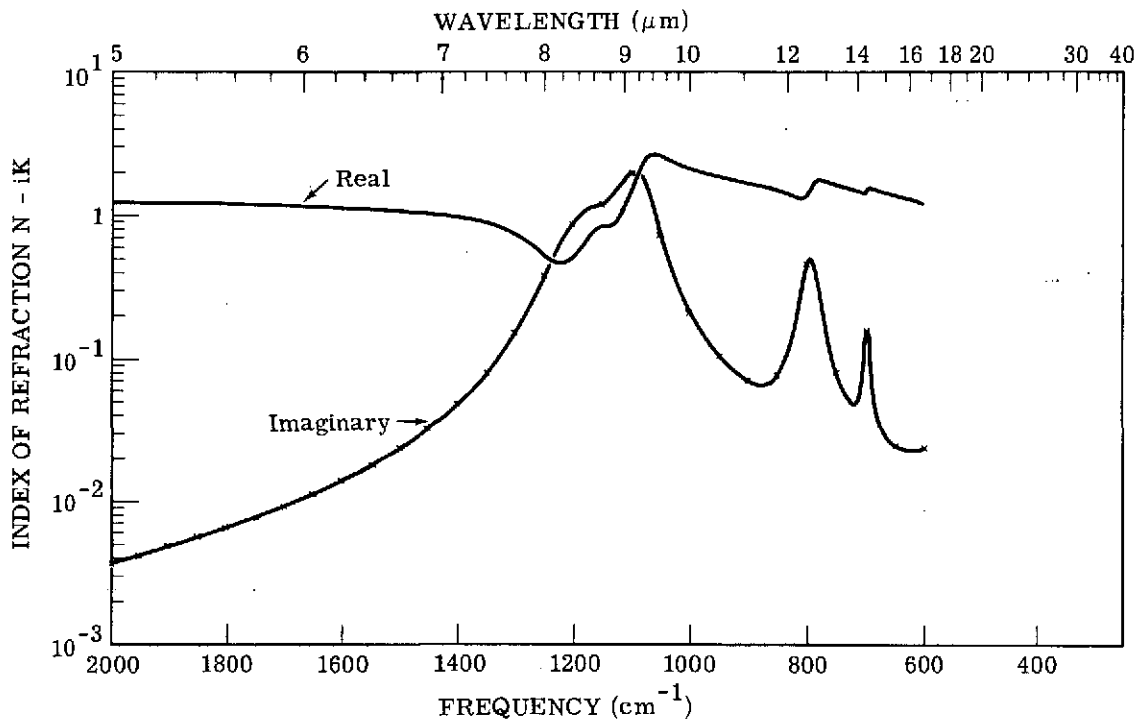
FIGURE 10. EFFECTIVE COMPLEX INDEX OF REFRACTION FOR CHERT

WAVELENGTH (μm)

Experimental Curve for 74- to 250-μm Quartz Sample

Theoretical Curve for 125-μm Particle Diameter

FREQUENCY (cm^{-1})

(a) Diameter = 125.0 μm

WAVELENGTH (μm)

Experimental Curve for 0- to 37-μm Quartz Sample

Theoretical Curve for 30-μm Particle Diameter

FREQUENCY (cm^{-1})

(b) Diameter = 30.0 μm

WAVELENGTH (μm)

Theoretical Curve for 1-μm Particle Diameter

FREQUENCY (cm^{-1})
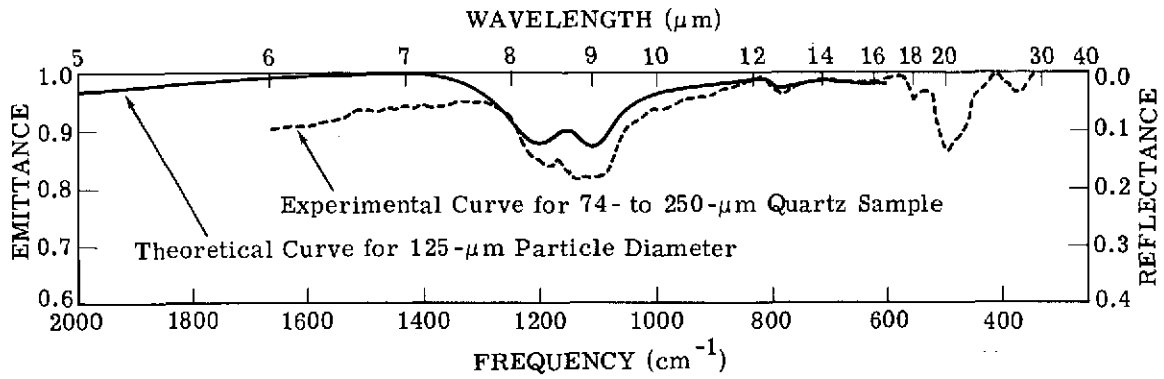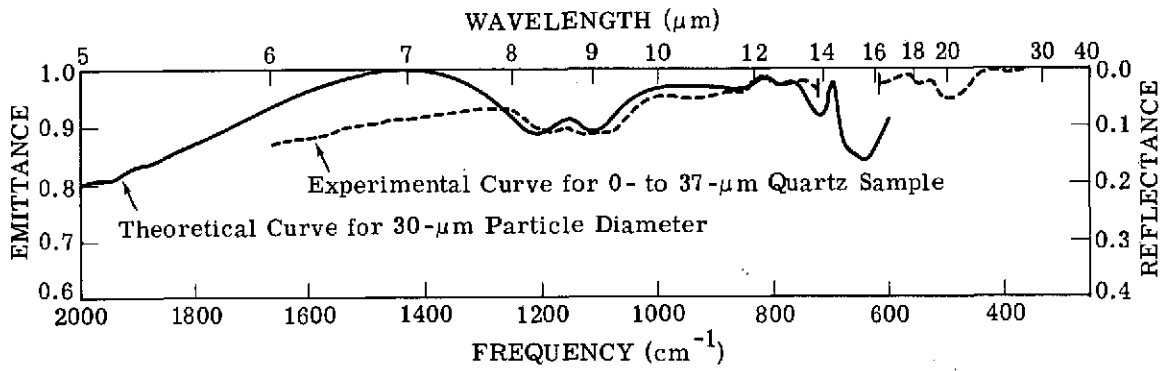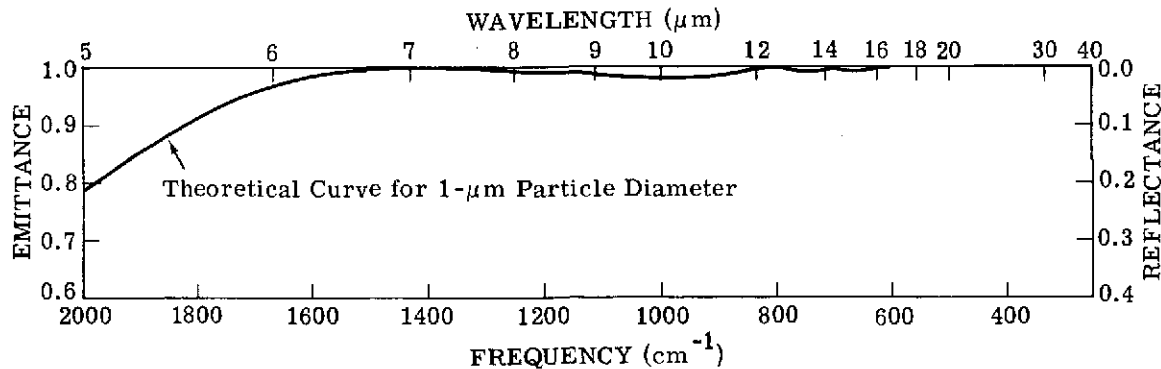
(c) Diameter = 1.0 μm

FIGURE 11. THEORETICAL SPECTRAL EMITTANCES OF CHERT (3 PARTICLE
DIAMETERS) AND EXPERIMENTAL EMITTANCES OF QUARTZ (2 PARTICLE
DIAMETERS)

partly a dolomite, seems the most plausible because the spectral positions of those two features in Figure 7 (before the theoretical model was implemented) occur at lower wavelengths than the experimental calcite (125 μm particle size) features. The model did not introduce the wavelength position discrepancy of those features.

More complex rocks were attempted next. Dunite (an ultrabasic, monomineralic rock composed of olivine, a biaxial mineral) and andesite (an intermediate, multimineralic rock) were run through the same procedure as chert and limestone. The spectral reflectivity curves of polished samples of each are shown in Figure 12 [4], though the reflection measurements were made at 30° from normal incidence. This source of error is negligible for purposes of this report. The indices of refraction for dunite and andesite resulting from the classical oscillator fitting program are given in Figures 13 and 14, respectively. The calculated spectral emittances are shown in Figure 15 for both rocks.

A comparison of calculated curves with experimental emittance spectra [4] of dunite are shown in Figure 16. The experimental curves, which are not quantitatively accurate in terms of absolute emittance, show the 40-80 μm dunite dust as having more spectral contrast than the 150-300 μm dunite sand in the major reststrahlen region, which is unlike any other laboratory measurement of silicate rocks from the same reference, making these data highly suspect. The 30 μm theoretical curve shows most of the features of the 40-80 μm experimental curve in the 9.0 to 12.0 μm wavelength region, but is more exaggerated than the experimental curve. The results for the 125 μm particle diameter are poorly correlated with measured values for dunite sand, and the 1 μm results are only slightly similar to the 10 μm powder experimental curve. If these experimental curves should represent true emittances of dunite powders, the theoretical model is a failure on complex rocks.

These results, coupled with the fact that no experimental curves of this type are available for andesite, make evaluation of this model incomplete for complex rocks. Further testing is required to provide a proper test of the model. If the model is valid for complex rocks, however, at least one implication of these results is pertinent to geological remote sensing. Note in Figure 15 that for both dunite and andesite, there is relatively little change in calculated spectral emittance between 125 μm and 30 μm particle diameter curves in the vicinity of the major reststrahlen bands, whereas the 1 μm curves display significantly less contrast than the others. Most naturally occurring rock surfaces are composed of particles considerably larger than 30 μm. Therefore, Figure 15 would imply that unless a silicate rock surface is coated by particles on the order of a few micrometers in diameter, surface texture will have much less effect than rock composition on spectral emittance. Chert also seems to exhibit this behavior in its major reststrahlen region from 8 to 10 μm.

The same conclusion could not be extended to limestone. In fact some of the texturally induced spectral changes in carbonates may eventually become useful for deducing surface rough-
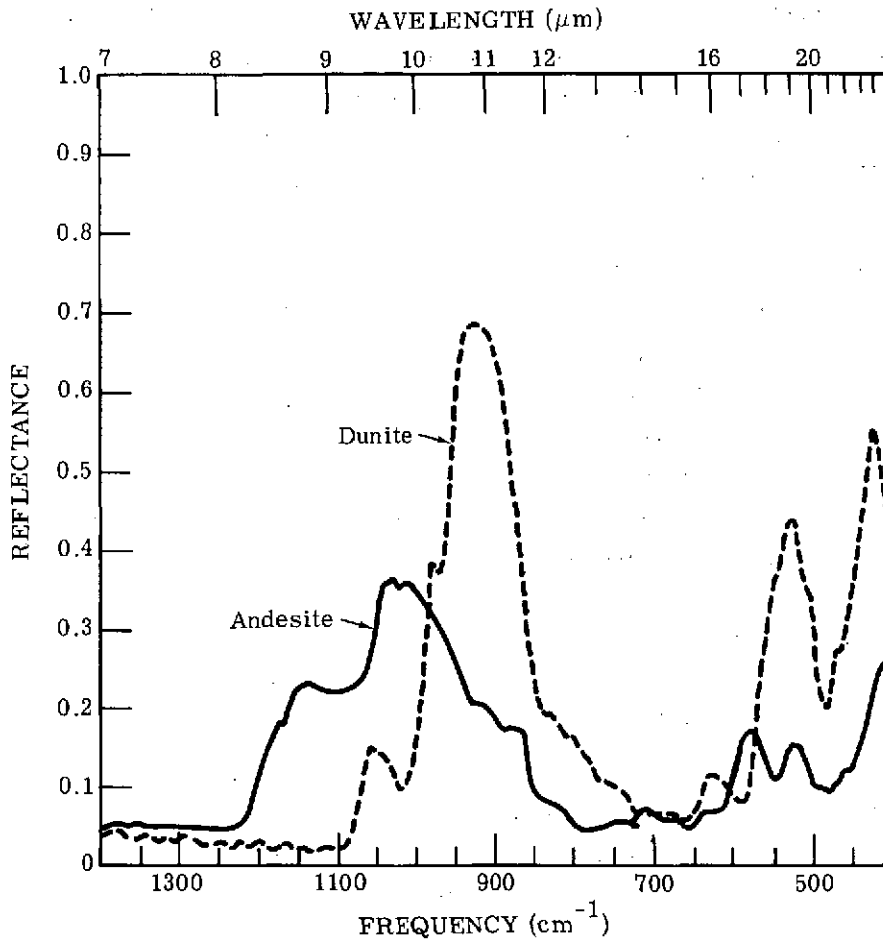
FIGURE 12. EXPERIMENTAL REFLECTIVITIES OF POLISHED SURFACES OF DUNITE
AND ANDESITE [4]

WAVELENGTH (μm)
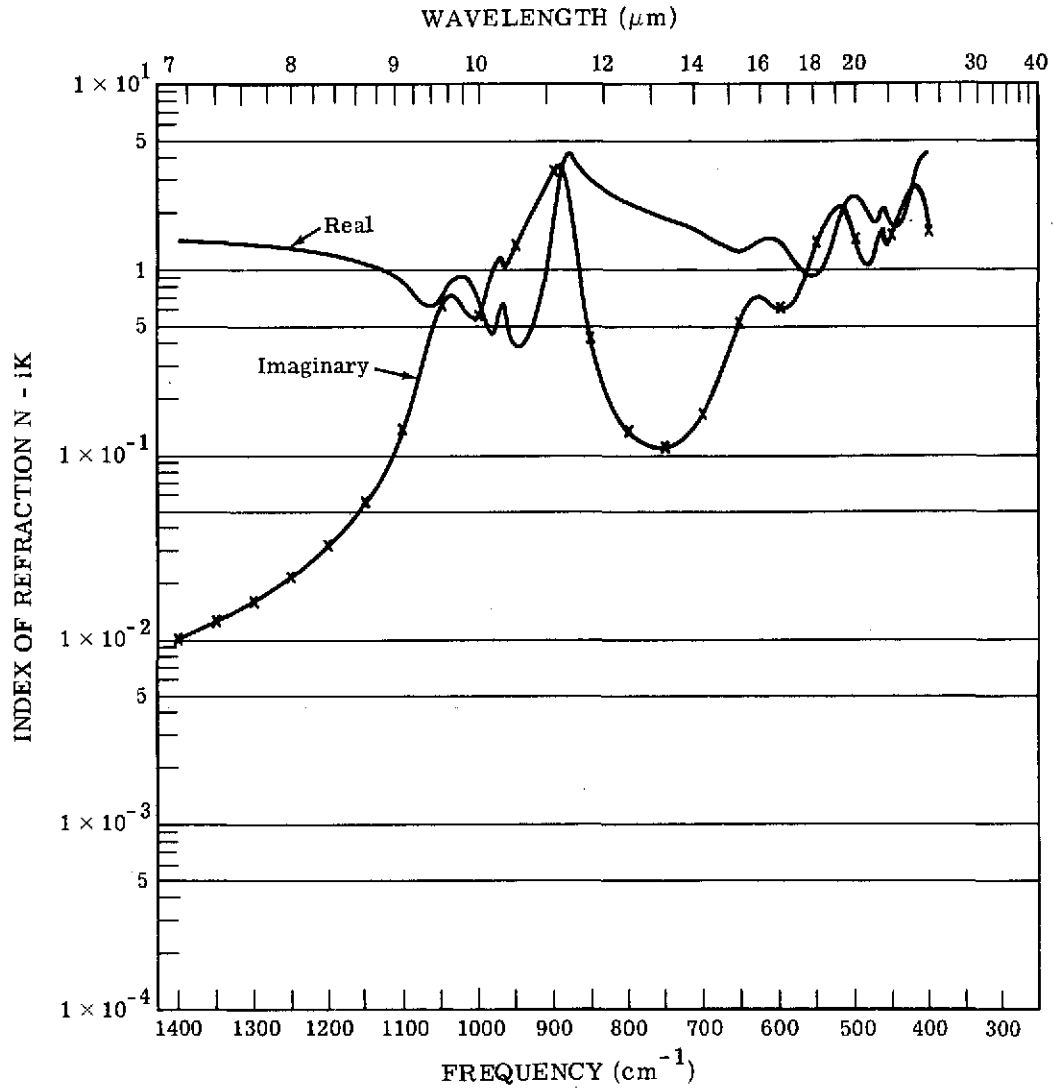
FIGURE 13. EFFECTIVE COMPLEX INDEX OF REFRACTION OF DUNITE

37
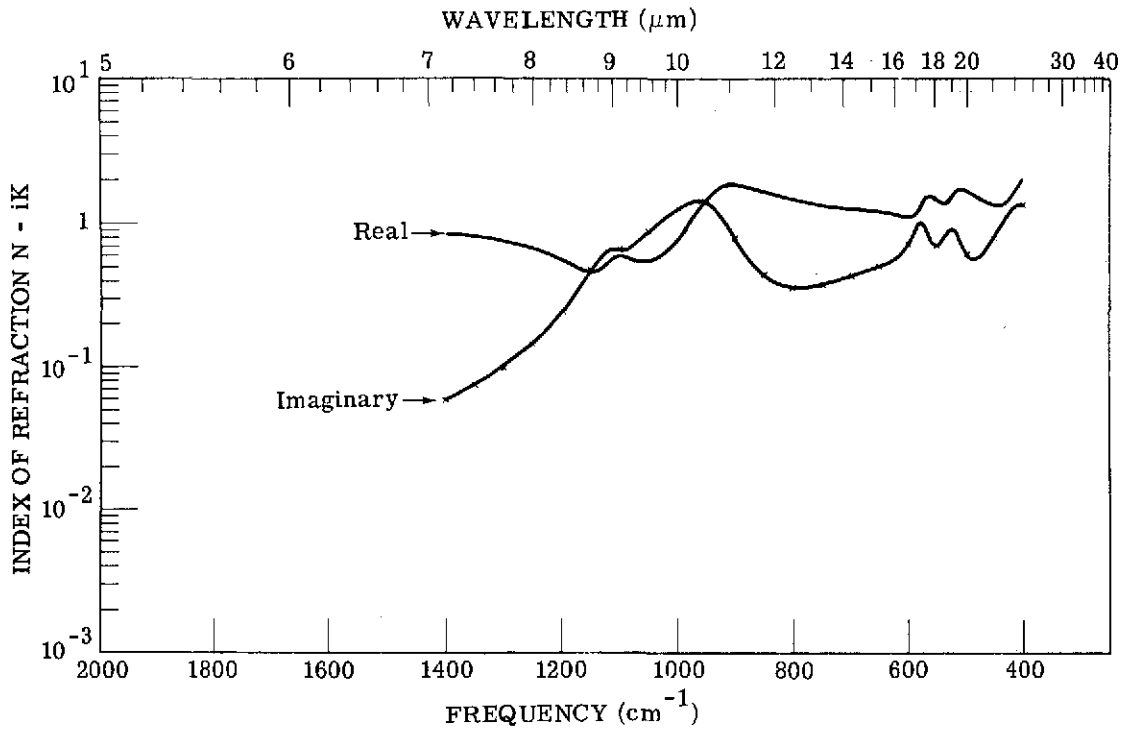
FIGURE 14. EFFECTIVE COMPLEX INDEX OF REFRACTION OF ANDESITE

WAVELENGTH (μm)

Dunite

FREQUENCY (cm^{-1})

WAVELENGTH (μm)

Andesite

FREQUENCY (cm^{-1})
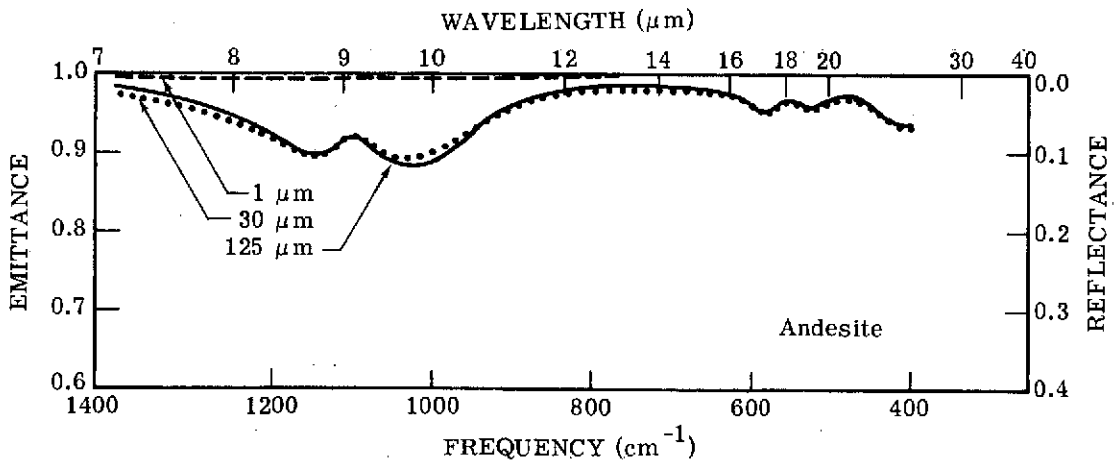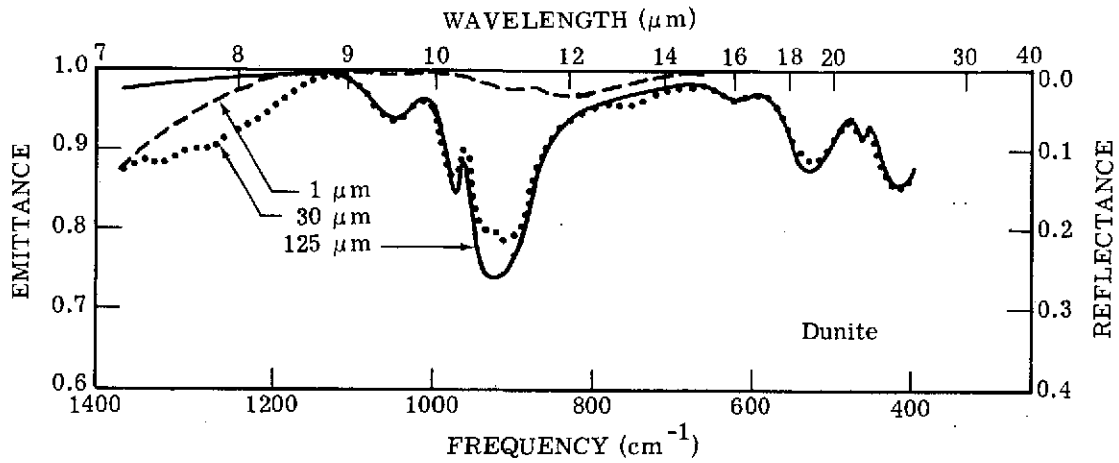
FIGURE 15. CALCULATED SPECTRAL EMITTANCES OF DUNITE AND ANDESITE FOR THREE PARTICLE DIAMETERS

39
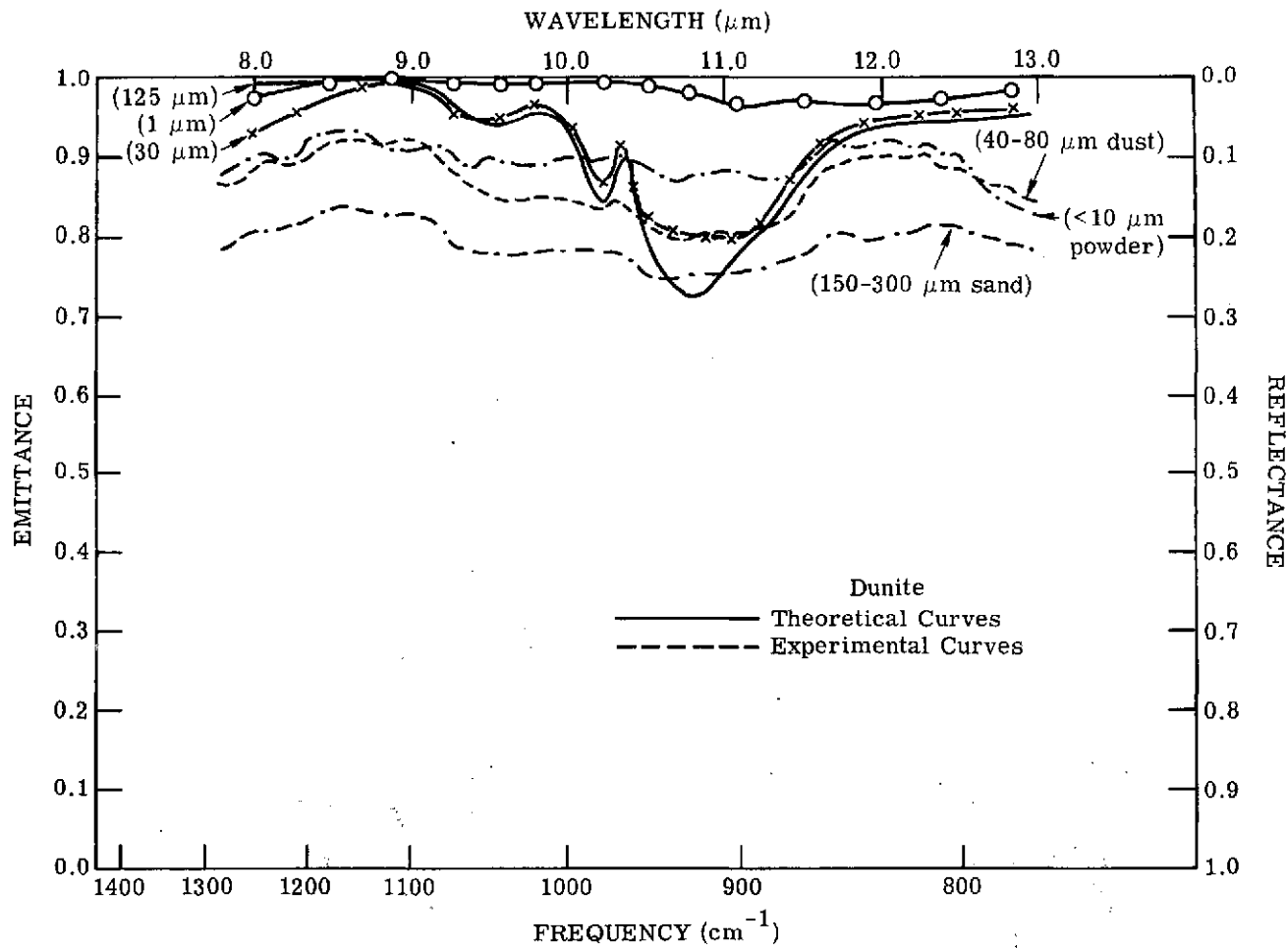
FIGURE 16. COMPARISON OF THEORETICAL AND EXPERIMENTAL SPECTRAL EMITTANCE CURVES
OF DUNITE

40

ness by remote sensing methods. However, Figures 9, 11, and 15 show that there is no difficulty discriminating carbonates from silicates for almost any particle diameter.

Since the oscillator parameters calculated in this section may be useful to atmosphericists for aerosol modeling, Table 2 lists them for the Manitou limestone (possibly dolomite), chert, dunite, and andesite. These parameters should be used with caution, since the spectral reflectivity curves from which they were calculated (Figures 7 and 12) came from different sources, and probably none were measured with the care ordinarily given to measurements for this purpose.

3.4 CONCLUSIONS

Two methods have been discussed for modeling the spectral emittance of irregular rock surfaces. The method described in Section 3.2 can be used only for simple, monomineralic rocks consisting of uniaxial crystals. The method of Section 3.3, which can be applied to any kind of rock, is simpler than the more rigorous method of Section 3.2. More laboratory data are required to evaluate the accuracy of both methods, though the Section 3.3 method is preferred on the basis of its slightly better correlation with laboratory spectra and its simpler procedure.

The spectral emittances of two minerals (quartz and calcite) and four rocks (limestone, chert, dunite, and andesite) were calculated. The results indicate that for silicate rock surfaces, texture* does not control spectral emittance as much as chemical composition, as long as the diameters of particles comprising the surface are on the order of $30 \mu m$ or greater — which is the case for most rocks not covered with products of weathering. The relevance of these results to geological remote sensing is that variations of texture indigenous to silicate rock genesis most likely will not mask the effect of rock composition on spectral emittance in the 8-14 μm wavelength region. Still other effects could seriously impair compositional remote sensing of silicate rocks in the thermal infrared wavelength region; these might arise, for example, from layers or coatings of weathering products, which in some cases can be an optically thick covering composed of very fine particles. The effects of such coverings on the spectral emittance of naturally-exposed rock surfaces have not been adequately investigated; the model just discussed in Section 3.3 would no doubt be useful in such a study. For carbonate rocks, textural effects on spectral emittance can be appreciably large, though not of such a nature as to cause misidentification of carbonates as non-carbonates. These effects may eventually be helpful for determining the effective particle sizes of remote carbonate target surfaces, which in some cases may exhibit meaningful spatial patterns. For instance, coral beach sands are composed primarily of $CaCO_3$, and are sometimes graded into well-ordered particle size distributions by wave action. The production of infrared ratio images for one spectral channel in the 11.1-11.6 μm region and another in the 10.6-11.1 μm region may not only be useful for identifying the presence of carbonates, but possibly for also mapping grada-

*Texture here refers to size of crystals or other particles composing the rock.

TABLE 2. EFFECTIVE OSCILLATOR PARAMETERS OF MANITOU
LIMESTONE (DOLOMITE), CHERT, DUNITE, AND ANDESITE

Rock Name	Effective Oscillator Parameters			
	$\nu_0 (cm^{-1})$	$4\pi\rho$	γ	ε_∞
Manitou Limestone	727.89	0.00098	0.01345	1.6148
	888.78	0.07415	0.01417	
	1469.80	0.45990	0.05173	
Chert	393.93	0.31095	0.00709	1.8066
	449.73	0.74778	0.00951	
	696.85	0.00633	0.01248	
	792.03	0.06176	0.04004	
	1080.70	0.40093	0.04897	
	1161.00	0.060291	0.06086	
	1225.40	0.01127	0.16826	
Dunite	413.21	0.05411	0.05007	2.9303
	463.81	0.01035	0.01239	
	512.80	0.67690	0.02692	
	839.61	0.17015	0.10213	
	885.72	0.69532	0.08104	
	968.94	0.09393	0.02961	
	1031.80	1.73020	0.08772	
Andesite	396.17	0.92410	0.18422	1.3302
	520.38	0.12561	0.07174	
	573.87	0.08494	0.05188	
	659.90	0.48928	0.55569	
	940.43	0.44104	0.11233	
	1109.10	0.01436	0.05062	

tions in particle sizes. Laser scanners of the future most likely will be additionally useful for discriminating among carbonate rocks on the basis of the spectral position of the sharp feature near 11.4μm.

The irregular rock surface models presented in this report should also be useful to atmosphericists interested in modeling the effects of aerosols on atmospheric absorption and scattering in the 8-14 μm wavelength region. For such models, a knowledge of the effective refractive indices of aerosol constituents is necessary, and these can be provided by the procedure of Section 3.3, after further experimental laboratory work defines the accuracy of this procedure.

Before either of the models in this report can be made quantitatively useful, however, a laboratory program is needed whereby samples are polished, measured for spectral reflectivity, ground up to various particle sizes, and carefully measured again. This would make possible the comparison of calculated emittances with lab spectra of the same rock samples. Should this produce positive results, the models would then need to be expanded to permit the calculation of spectral emittances and transmittances of aerosol clouds or irregular rock surfaces with a range of particle diameters, instead of using one effective particle diameter to describe the cloud or rock surface. After these two steps, attempts could then be made to make the models quantitatively accurate.

4
SELECTION OF OPTIMUM FILTERS FOR IMPLEMENTING TWO-CHANNEL INFRARED RATIO IMAGE DISCRIMINATION AMONG SILICATE ROCK TYPES

Over the past two years a thermal infrared ratio imaging technique, developed under this NASA task [1, 3, 12, 13], has been applied to infrared scanner data gathered from two sites, Mill Creek, Oklahoma [1, 14], and Pisgah Crater, California [3, 15]. Heretofore, a prototype two-element thermal infrared detector has been used to produce ratio images which permit discrimination among silicate rocks differing greatly in %SiO$_2$ content. This section describes an effort to select optimum filters for implementing this technique, i.e., to determine what better spectral regions than the two employed by the existing two-element detector could be chosen for this purpose.

4.1 CALCULATION PROCEDURE

From References [3] and [14], the equation which describes the total spectral radiance received by an airborne detector from a geological target on the ground is

$$L_\lambda = \left[\epsilon_\lambda L_{bb_\lambda}(T) + \rho_\lambda L_{sky_\lambda}\right]\tau_{A_\lambda} + L_{V_\lambda} = \left\{\epsilon_\lambda\left[L_{bb_\lambda}(T) - L_{sky_\lambda}\right] + L_{sky_\lambda}\right\}\tau_{A_\lambda} + L_{V_\lambda} \qquad (12)$$

where

L_λ = total spectral radiance of wavelength λ arriving at the detector

$\epsilon_\lambda = 1 - \rho_\lambda$ = rock spectral emittance taken from laboratory data (ρ_λ = spectral reflectance)

$L_{bb_\lambda}(T)$ = spectral radiance of a blackbody at same temperature T as rock

L_{sky_λ} = spectral radiance from sky incident on diffuse rock surface

τ_{A_λ} = spectral atmospheric transmissivity

L_{V_λ} = spectral radiance from emission and scattering into the beam by the atmosphere in the path between rock and detector

---

13. Vincent, R. K., and F. Thomson, Spectral Compositional Imaging of Silicate Rocks, J. of Geophys. Res., Vol. 77, 1972, pp. 2465-71.

14. Vincent, R. K., F. Thomson, and K. Watson, Recognition of Exposed Quartz Sand and Sandstone by Two-Channel Infrared Imagery, J. of Geophys. Res., Vol. 77, 1972, pp. 2473-77.

15. Vincent, R. K., and F. Thomson, Rock Type Discrimination from Ratioed Infrared Scanner Images of Pisgah Crater, California, Science, Vol. 175, 1972, pp. 986-88.

The atmospheric parameters L_{sky_λ}, τ_{A_λ}, and L_{V_λ} were calculated from a clear, dry atmosphere model developed at ERIM (then Willow Run Laboratories) [16]. The altitude of the aircraft in all subsequent calculations is assumed to be 1 km above ground.

For two selected filters and an assumed rock temperature, Eq. 12 can be integrated over the respective spectral regions, and a ratio of radiances in the two spectral channels for each of the laboratory samples can be calculated. The ratio is then given by

$$
R_{12} = \frac{L_{\Delta\lambda_1}(T)}{L_{\Delta\lambda_2}(T)} = \frac{\int_0^\infty f_1(\lambda)L_\lambda(T)d\lambda}{\int_0^\infty f_2(\lambda)L_\lambda(T)d\lambda}
\tag{13}
$$

where $f_1(\lambda)$ and $f_2(\lambda)$ are the filter spectral responses in the two respective channels. If all of the rock samples are assumed to be at a temperature of $300^\circ K$ and atmospheric parameters for an altitude of 1 km are used, the radiances calculated from Eq. (12) can be substituted into Eq. (13) to yield a ratio for each sample, as measured by this specific detector filtered by $f_1(\lambda)$ and $f_2(\lambda)$ at an altitude of 1 km.

The spectral data used for a test case came from a collection of silicate rocks on which laboratory measurements have been made for the U.S. Bureau of Mines [17]. These spectral data, which have been added to the NASA Earth Resources Spectral Information System in the latest supplement [18], are summarized in Table 3. Only 22 of the available 26 rocks from the total suite were used for this study because three of the samples (granites) contain some mineral grains larger than the spot size of the laboratory spectrometer, and one sample is a peridotite. (Peridotite is an ultrabasic rock [very low %SiO_2] that is not expected to be included in

16. Anding, D., R. Kauth, and R. Turner, Atmospheric Effects on Infrared Multispectral Sensing of Sea Temperature from Space, Report No. 2676-5-F, Willow Run Laboratories of the Institute of Science and Technology, The University of Michigan, Ann Arbor, 1970.

17. Wagner, T., R. K. Vincent, B. Drake, R. Mitchell, and P. Jackson, Tunnel-Site Selection by Remote Sensing Techniques, Report No. 10018-13-F, U.S. Bureau of Mines Contract H0210041, Willow Run Laboratories of the Institute of Science and Technology, The University of Michigan, Ann Arbor, 1972.

18. Vincent, R. K., The NASA Earth Resources Spectral Information System: A Data Compilation - Second Supplement, Report No. 31650-156-T, NASA Contract NAS9-9784, Environmental Research Institute of Michigan, Ann Arbor, 1973.

the $\%SiO_2$ range of linear correlation coefficients for an infrared ratio.) The chemical parameter data [19] were supplied by rapid rock analysis. Also included in Table 3 is a listing of $\%SiO_2$ and $\%(SiO_2 - Al_2O_3)$ content (weight percent) and two chemical parameters for which high correlations have been found with the infrared ratios of the current two-element detector [19].

A computer program, LTOTAL6, (described in more detail in Appendix A) was written to calculate the radiance ratios from Eqs. (12) and (13) for three types of filters: square window, Hamming window (sine), and individual user-specified filters. Locomotion (moving the filter along at specified wavelength increments) of the first two types of filters is possible in LTOTAL6, but not with user-specified types. Only square window filters were utilized for this study.

4.2 CALCULATED RESULTS AND CONCLUSIONS

The first chemical parameter tested was $\%SiO_2$. The initial square filter width implemented on LTOTAL6 was $0.5\,\mu$m, incremented at 0.5μm wavelength intervals. All permutations of radiance ratios for that spectral width and wavelength increment were calculated between the wavelength limits of 8.0μm and 13.0μm. Smaller increments for the 0.5μm filters were not calculated for two reasons: the narrow filters are not as favored by signal-to-noise considerations as wider filters, and it would have been expensive to calculate the 0.5μm filter results for 0.1μm increments. Table 4 shows the resulting linear correlation coefficients between $\%SiO_2$ and infrared ratios of all 22 silicate rocks in Table 3 for the highest correlated 0.5μm-wide filters only. [Note: For this and all following tables in this section, only the highest filter pair correlation coefficients will be shown. The data not shown for all filter cases range down to correlation coefficients on the order of 0.1. Also, all correlations for this and following tables are negative, but the minus sign is suppressed.] About the best filter combination is the 8.0-$8.5\,\mu$m numerator and 11.5-$12.0\,\mu$m denominator, which produces a ratio that has a 0.8871 linear correlation coefficient with $\%SiO_2$ for the 22 silicate rocks in the test suite.

The next filter-width implemented was 1.5μm, with a 0.1μm increment between the limits of 8.0μm and 13.0μm. Table 5 shows those results. The best filter combination for this filter width appears to be a numerator of 8.3-$9.8\,\mu$m and a denominator of 9.50-$11.00\,\mu$m, which produces a ratio that has a 0.8801 linear correlation with $\%SiO_2$ for the same 22-sample rock suite.

Table 6 shows the results for 2.0μm-wide filters incremented at 0.1μm and Table 7 for 2.5μm-wide filters incremented at 0.1μm. The best pair of 2.0μm-wide filters would employ 8.2-$10.2\,\mu$m in the numerator and 9.2-$11.2\,\mu$m in the denominator, for a ratio that has a linear

19. Vincent, R. K., T. Wagner, B. Drake, and P. Jackson, Geologic Reconnaissance and Lithologic Identification by Remote Sensing, Report No. 191700-8-F, U.S. Bureau of Mines Contract H0220064, Environmental Research Institute of Michigan, Ann Arbor, 1973.

TABLE 3. ROCK SUITE USED FOR FINDING OPTIMUM FILTERS FOR A
TWO-CHANNEL RATIO IMAGE METHOD

Rock Name	$\%SiO_2$	$\%(SiO_2 - Al_2O_3)$	ERSIS Curve No.
Granite (A119)	66.2	49.7	B09019 2
Rhyolite (SA-49)	75.1	63.6	B09019 4
Syenite (E83A)	61.4	41.1	B09019 6
Trachyte	68.3	50.6	B09019 7
Nepheline Syenite	58.3	38.6	B09019 8
Granodiorite (A117)	53.6	34.9	B09019 9
Granodiorite (A127)	62.8	46.8	B09019 10
Dacite (E12A)	65.7	50.7	B09019 11
Monzodiorite Por-			
phyry (2A1)	66.9	51.6	B09019 12
Monzonite (2B5)	67.0	51.0	B09019 13
Diorite (A129)	61.0	44.6	B09019 14
Diorite (E47C)	56.2	38.8	B09019 15
Andesite (E55A)	57.8	42.6	B09019 16
Rhyodacite (2A3)	67.9	53.4	B09019 17
Gabbro (E80A)	50.6	34.9	B09019 18
Basalt (1A8)	47.5	31.2	B09019 19
Basalt (WI-1-104)	48.0	32.9	B09019 20
Basalt (S95)	48.4	31.8	B09019 21
Basalt (5B4)	48.3	31.8	B09019 22
Basalt (1A3)	47.8	30.9	B09019 23
Anorthosite (AN)	49.7	21.4	B09019 24
Diabase	52.4	37.4	B09019 25

TABLE 4. CORRELATION BETWEEN $\%SiO_2$
AND RATIOS OF 0.5μm-WIDE FILTERS FOR
0.5μm INCREMENTS*

Numerator (μm) Denominator (μm)	8.00-8.50	8.50-9.00
10.00-10.50	–	–
10.50-11.00	–	.8712
11.00-11.50	–	.8668
11.50-12.00	.8871	–
12.00-12.50	.8775	–

*Filter pairs with low correlation coefficients are
omitted.

TABLE 5. CORRELATION BETWEEN %SiO$_2$ AND RATIOS OF 1.5µm-WIDE FILTERS[†]
FOR 0.1µm INCREMENTS

Numerator (µm)→ / Denominator (µm)↓	8.00-9.50	8.10-9.60	8.20-9.70	8.30-9.80	8.40-9.90	8.50-10.00	8.60-10.10	8.70-10.20
9.50-11.00	.8657	.8714	.8770	.8801	.8792	.8755	.8698	.8632
9.60-11.10	.8698	.8731	.8769	.8780	.8755	.8703	.8631	–
9.70-11.20	.8722	.8736	.8760	.8755	.8716	.8650	–	–
9.80-11.30	.8751	.8747	.8758	.8737	.8686	.8609	–	–
9.90-11.40	.8768	.8751	.8751	.8717	.8655	–	–	–
10.00-11.50	.8780	.8749	.8737	.8691	.8619	–	–	–
10.10-11.60	.8781	.8739	.8717	.8658	–	–	–	–
10.20-11.70	.8768	.8716	.8684	.8614	–	–	–	–
10.30-11.80	.8742	.8683	.8645	–	–	–	–	–
10.40-11.90	.8714	.8650	.8606	–	–	–	–	–
10.50-12.00	.8694	.8625	–	–	–	–	–	–
10.60-12.10	.8681	.8608	–	–	–	–	–	–
10.70-12.20	.8670	–	–	–	–	–	–	–
10.80-12.30	.8656	–	–	–	–	–	–	–
10.90-12.40	.8635	–	–	–	–	–	–	–
11.00-12.50	.8601	–	–	–	–	–	–	–

[†] Filter pairs with low correlation coefficients are omitted.

TABLE 6. CORRELATION BETWEEN %SiO$_2$ AND RATIOS OF 2.0µm-WIDE FILTERS[†]
FOR 0.1µm INCREMENTS

*N (µm)→ / ↓*D (µm)	8.0-10.	8.1-10.1	8.2-10.2	8.3-10.3	8.4-10.4	8.5-10.5	8.6-10.6	8.7-10.7	8.8-10.8	8.9-10.9	9.0-11.
8.6-10.6	–	–	–	–	.8703	.8770	0	–	–	–	–
8.7-10.7	–	–	–	.8667	.8765	.8741	–	–	–	–	–
8.8-10.8	–	–	–	.8760	.8768	.8696	–	–	–	–	–
8.9-10.9	–	–	.8740	.8808	.8774	.8693	–	–	–	–	–
9.0-11.0	–	.8712	.8813	.8840	.8794	.8722	–	–	.8686	.8752	0
9.1-11.1	.8695	.8790	.8850	.8853	.8802	.8736	.8682	.8666	.8699	.8727	.8689
9.2-11.2	.8772	.8831	.8862	.8846	.8789	.8723	.8670	–	.8666	.8670	–
9.3-11.3	.8815	.8845	.8845	.8821	.8755	.8686	–	–	–	–	–
9.4-11.4	.8823	.8830	.8822	.8774	.8699	–	–	–	–	–	–
9.5-11.5	.8803	.8796	.8778	.8720	–	–	–	–	–	–	–
9.6-11.6	.8778	.8763	.8739	.8674	–	–	–	–	–	–	–
9.7-11.7	.8745	.8720	.8688	–	–	–	–	–	–	–	–
9.8-11.8	.8719	.8685	–	–	–	–	–	–	–	–	–
9.9-11.9	.8689	–	–	–	–	–	–	–	–	–	–

*Numerator
*Denominator

[†] Filter pairs with low correlation coefficients are omitted.

correlation of 0.8862 with $\%SiO_2$. Likewise, as seen from Table 7, the best pair of $2.5\,\mu$m-wide filters have a numerator of either 8.0-10.5 μm or 8.1-10.6 μm and denominator of 9.2-11.7 μm, which produces a ratio that has a linear correlation coefficient of 0.8830 with $\%SiO_2$.

This optimization procedure was also implemented with the chemical parameter $\%(SiO_2 - Al_2O_3)$ for the three widest filter combinations. The results are shown in Tables 8, 9, and 10. The best filter combinations from all the previous tables are summarized in Table 11.

4.3 CONCLUSIONS

Five conclusions can be derived from the data in Tables 4-11. First, the best linear correlations between $\%SiO_2$ or $\%(SiO_2 - Al_2O_3)$ and the infrared ratios are significantly high for the 22-rock test suite. Second, the widest filters ($1.5\,\mu$m, $2.0\,\mu$m, and $2.5\,\mu$m widths) yield ratios that are correlated practically as well as the ratios from $0.5\,\mu$m-wide filters with $\%SiO_2$. The use of $0.1\,\mu$m increments for the $0.5\,\mu$m filters would not change this conclusion, even if it increased the correlations to 0.95, which would be unlikely. The primary reason for this is that the silicate reststrahlen spectral features of silicates are fairly broad. Third, the best wide-filter pairs all display spectral overlap between numerator and denominator, with more than $0.7\,\mu$m overlap in the best $2.5\,\mu$m-wide pair. Fourth, the spectral location of the wider filters near the optimum spectral position is not critical, as can be noted by the slow drop-off of correlation as filters are displayed a few tenths of a micron from the optimum position. Finally, the filter pairs best correlated with $\%(SiO_2 - Al_2O_3)$ are slightly different from the filter pairs best correlated with $\%SiO_2$. In both cases, $2.0\,\mu$m seems to be the most optimum width, because even though the $0.5\,\mu$m-wide filter had a very slightly higher correlation with $\%SiO_2$, engineering design greatly favors the wider filter for its significantly higher signal-to-noise capabilities. Further, the $2.0\,\mu$m-wide optimum filters for both $\%SiO_2$ and $\%(SiO_2 - Al_2O_3)$ discrimination are located in almost the same spectral region. Therefore, the final conclusion of this investigation is that from an aircraft altitude of 1 km, 8.1-10.1 μm and 9.2-11.2 μm are the optimum square filters for implementing the two-channel infrared ratio imaging method to discriminate among silicate rocks on the basis of chemical parameters.

TABLE 7. CORRELATION BETWEEN %SiO$_2$ AND RATIOS OF 2.5μm-WIDE FILTERS FOR 0.1μm INCREMENTS †

Numerator (μm)→ ↓ Denominator (μm)	8.00-10.50	8.10-10.60	8.20-10.70	8.30-10.80	8.40-10.90	8.50-11.00
8.60-11.10	–	–	–	–	.8671	.8690
8.70-11.20	–	–	–	.8668	.8681	.8655
8.80-11.30	–	–	.8676	.8695	.8674	–
8.90-11.40	.8671	.8718	.8733	.8726	.8686	–
9.00-11.50	.8762	.8789	.8782	.8760	.8711	–
9.10-11.60	.8816	.8828	.8807	.8774	.8719	–
9.20-11.70	.8830	.8830	.8799	.8757	.8659	–
9.30-11.80	.8813	.8804	.8766	.8717	.8650	–
9.40-11.90	.8767	.8752	.8709	.8653	–	–
9.50-12.00	.8712	.8692	.8648	–	–	–
9.60-12.10	.8663	.8642	–	–	–	–

† Filter pairs with low correlation coefficients are omitted.

TABLE 8. CORRELATION BETWEEN %(SiO$_2$ - Al$_2$O$_3$) AND RATIOS OF 1.5μm-WIDE FILTERS FOR 0.1μm INCREMENTS †

Numerator (μm)→ ↓ Denominator (μm)	8.00-9.50	8.10-9.60	8.20-9.70	8.30-9.80	8.40-9.90	8.50-11.00	8.60-11.10
9.50-11.00	.9168	.9201	.9215	.9207	.9175	.9123	.9059
9.60-11.10	.9217	.9226	.9223	.9198	.9151	.9084	–
9.70-11.20	.9233	.9223	.9209	.9168	.9108	–	–
9.80-11.30	.9241	.9214	.9188	.9133	.9059	–	–
9.90-11.40	.9234	.9195	.9159	.9091	–	–	–
10.00-11.50	.9213	.9161	.9116	–	–	–	–
10.10-11.60	.9177	.9115	.9061	–	–	–	–
10.20-11.70	.9129	.9058	–	–	–	–	–
10.30-11.80	.9075	–	–	–	–	–	–

† Filter pairs with low correlation coefficients are omitted.

TABLE 9. CORRELATION BETWEEN %(SiO$_2$ - Al$_2$O$_3$) AND RATIOS OF 2.0μm-WIDE FILTERS FOR 0.1μm INCREMENTS †

Numerator (µm)→ Denominator(µm)↓	8.00-10.00	8.10-10.10	8.20-10.20	8.30-10.30	8.40-10.40	8.50-10.50
8.60-10.60	-	-	-	-	.9146	.9173
8.70-10.70	-	-	-	.9136	.9183	.9124
8.80-10.80	-	-	.9114	.9201	.9162	-
8.90-10.90	-	.9103	.9206	.9214	.9136	-
9.00-11.00	.9107	.9203	.9245	.9217	.9132	-
9.10	.9203	.9254	.9262	.9216	.9129	-
9.20-11.20	.9245	.9273	.9257	.9196	.9106	-
9.30	.9271	.9264	.9230	.9155	-	-
9.40-11.40	.9254	.9227	.9179	.9092	-	-
9.50-11.50	.9213	.9174	.9119	-	-	-
9.60-11.60	.9171	.9125	-	-	-	-
9.70-11.70	.9109	-	-	-	-	-

† Filter pairs with low correlation coefficients are omitted.

TABLE 10. CORRELATION BETWEEN %(SiO$_2$ - Al$_2$O$_3$) AND RATIOS OF 2.5μm-WIDE FILTERS FOR 0.1μm INCREMENTS †

Numerator (µm)→ Denominator(µm)↓	8.00-10.50	8.10-10.60	8.20-10.70	8.30-10.80	8.40-10.90	8.50-11.00	8.60-11.10
8.40-10.90	-	-	-	.9000	0	-	-
8.50-11.00	-	-	.9003	.9080	.9088	0	-
8.60-11.10	-	.8987	.9095	.9107	.9067	.8995	0
8.70-11.20	.9027	.9087	.9114	.9079	.8966	-	-
8.80-11.30	.9095	.9119	.9097	.9027	-	-	-
8.90-11.40	.9128	.9125	.9073	.8980	-	-	-
9.00-11.50	.9145	.9124	.9056	.8952	-	-	-
9.10-11.60	.9148	.9114	.9037	-	-	-	-
9.20-11.70	.9128	.9085	.9004	-	-	-	-
9.30-11.80	.9088	.9039	.8955	-	-	-	-
9.40-11.90	.9027	.8974	-	-	-	-	-
9.50-12.00	.8962	-	-	-	-	-	-

† Filter pairs with low correlation coefficients are omitted.

TABLE 11. SUMMARY OF OPTIMUM FILTER SELECTIONS FOR THE TWO-CHANNEL RATIO IMAGE METHOD

Filter Width (μm)	Increment	%SiO₂ vs. Ratio		%(SiO₂ − Al₂O₃) vs. Ratio	
		Best Filter Combin. (μm)	Linear Correl. Coefficient	Best Filter Combin. (μm)	Linear Correl. Coefficient
0.5	0.5	$\frac{8.0-8.5}{11.5-12.0}$	0.8871	–	–
1.5	0.1	$\frac{8.3-9.8}{9.5-11.0}$	0.8801	$\frac{8.0-9.5}{9.8-11.3}$	0.9241
2.0	0.1	$\frac{8.2-10.2}{9.2-11.2}$	0.8862	$\frac{8.1-10.1}{9.2-11.2}$	0.9273
2.5	0.1	$\frac{8.0-10.5 \text{ or } 8.1-10.6}{9.2-11.7}$	0.8830	$\frac{8.0-10.5}{9.1-11.6}$	0.9148

5

RATIO CODES OF LABORATORY DATA FOR SELECTED RATIOS OF THE NASA/ERIM M-7 AIRBORNE SCANNER CHANNELS

As will be explained in Section 6, it is possible to process multispectral scanner data from either aircraft or satellites such that a ratio of radiances in two channels of scanner data can be made either directly proportional to or equal to the actual ratio of reflectances of the targets of interest, within an approximate 10% standard error. This opens the possibility that laboratory or field spectra of natural inorganic materials can be used to (1) determine which ratios of scanner data best enhance the target of interest, (2) search for false alarm candidates or look-alikes of the target, (3) interpret ratio images, and (4) possibly replace in-scene training sets in the future. However, to use large numbers of laboratory spectra as references is difficult for either manual or computer operations because of the great amount of information storage required, especially since the laboratory spectra must be searched at least once for each target of interest. Compression of the spectra into a shorter, more usable format is therefore needed.

5.1 CREATION OF M-7 RATIO CODES

To meet this need, the M-7 aircraft scanner ratio signatures for some of the laboratory reflectance spectra of natural materials recorded in the NASA Earth Resources Spectral Information System (ERSIS) were transformed into ratio codes in the following manner. The spectral curves (approximately 235 of them) used from ERSIS were initially selected on the basis of being continuous throughout the 0.4 - 2.5 μm wavelength region, except that most of the vegetation curves which met this criterion were omitted because laboratory spectra of plant components cannot easily be correlated with field spectra of the whole plant. Grass and conifers should show more correlation between lab and field spectra than most other vegetative types because their texture is relatively fine. After being called from the data bank, the curves were run through a computer program (DATFIX) that produced equal spacing between reflectance data points in each laboratory spectrum. This placed the data into the proper format for another computer program, ARAGAL (described in Appendix B), which calculated the average reflectance in nine selected ERIM M-7 scanner channels for each curve. A 50% sine filter was used to approximate the spectral shapes of the M-7 scanner channels. ARAGAL also calculated eleven selected ratios from the nine channels. These ratios were selected after inspection of lab data. If the symbol for the i-th channel reflectance divided by the j-th channel reflectance is taken to be R_{ij}, these eleven ratios were R_{98}, R_{95}, R_{85}, R_{76}, R_{75}, R_{65}, R_{62}, R_{61}, R_{54}, R_{53}, and R_{21}, where the spectral limits of each channel are as shown in Table 12.

Each ratio was divided into ten intervals, each containing on the order of 10% of the 235 spectral curves taken from ERSIS, as determined from a histogram plot of R_{ij} versus the number

TABLE 12. M-7 AIRBORNE SCANNER CHANNELS USED TO DETERMINE RATIO CODES

Channel Number	Spectral Limits	Ratios Calculated with this Channel
1	.43-.47 μm	R_{61}, R_{21}
2	.49-.51 μm	R_{62}, R_{21}
3	.53-.56 μm	R_{53}
4	.59-.63 μm	R_{54}
5	.63-.67 μm	R_{95}, R_{85}, R_{75}, R_{65}, R_{54}, R_{53}
6	.70-.90 μm	R_{76}, R_{65}, R_{62}, R_{61}
7	1.0-1.4 μm	R_{76}, R_{75}
8	1.5-1.8 μm	R_{98}, R_{85}
9	2.0-2.5 μm	R_{98}, R_{95}

of curves having an R_{ij} in a given interval ΔR_{ij}. Each of the ten ΔR_{ij} intervals was then assigned a digit from 0 to 9. Table 13 shows the ten intervals, with their assigned digits, for each of the eleven ratios. In this manner an eleven-digit number, one digit for each R_{ij}, with the order of ratio digits from left to right as given above, was created for each of the 235 curves. For example, the granodiorite spectrum in ERSIS has the following reflectance ratios: R_{98} = 1.13, R_{95} = 1.64, R_{85} = 1.45, R_{76} = 1.02, R_{75} = 1.32, R_{65} = 1.29, R_{62} = 1.50, R_{61} = 1.61, R_{54} = 1.04, R_{53} = 1.12, and R_{21} = 1.07. Therefore, the R_{98} value falls into the interval assigned to the digit 8, R_{95} into the digit 5 interval, etc. For this granodiorite spectrum the resulting eleven-digit number, hereinafter referred to as the M-7 ratio code, is 85322433443. Thereby, the entire granodiorite spectrum in the 0.4-2.5 μm wavelength region is reduced to an eleven-digit number.

Table 14 gives the ratio codes for 19 soil types (35 spectra), 82 minerals (174 spectra), 15 rock types (22 spectra), and 2 types of vegetation (4 spectra), calculated from ERSIS spectra. The documents from which the spectra originate, listed in Table 15, provide more information about these data. Although ratio codes for mineral and rock powders of 0-74 μm and 0-5 μm grain sizes were calculated, they are not reported here because they are unrealistic for most rocks and minerals in the natural state.

Another computer program, KOLEKT (described in Appendix C) was written to perform searches among the 235 laboratory spectra for user-specified targets, on the basis of the eleven-digit ratio codes produced by ARAGAL. The program KOLEKT makes use of Table 14. In addition to the tape from ARAGAL, it needs a title and a range of values for each of the eleven digits in order to perform its searches. The title is arbitrary and the ranges of values can be found by looking in Table 14 for one or more spectra of the desired material. KOLEKT takes the ranges of values and finds every curve in the 235-curve ratio data bank that has all its digits within the proper ranges. In this way all curves with signatures similar to the material searched for are pulled out to give a list of which materials can be mistaken for the desired one. KOLEKT has been designed to search for up to three different materials simultaneously. It also has the options of performing as many of these "three-at-a-time" searches as desired during one run on the computer. The results of searches for five iron oxides are given in Table 16. It is encouraging to see that iron oxides, which are important for mineralogical exploration, can be distinguished from all the other curves in the ratio data bank as it now stands.

5.2 CONCLUSIONS

The M-7 ratio code data bank produced by ARAGAL can be used in three principal ways:

(1) In feature selection to determine which ratios are best for discriminating a given target from all other targets in the data bank (look for a ratio with a 9 or 0 digit and the

TABLE 13. RATIO INTERVALS FROM ELEVEN-DIGIT M-7 RATIO CODE

Code   Ratio Intervals

Code	1st Digit (R_{98})	2nd Digit (R_{95})	3rd Digit (R_{85})	4th Digit (R_{76})	5th Digit (R_{75})	6th Digit (R_{65})
0	0- .424	0- .600	0-1.240	0- .957	0-1.185	0-1.148
1	.425- .636	.601- .970	1.241-1.334	.958-1.006	1.186-1.275	1.149-1.224
2	.637- .770	.971-1.200	1.335-1.400	1.007-1.044	1.276-1.344	1.225-1.257
3	.771- .840	1.201-1.320	1.401-1.500	1.045-1.070	1.345-1.432	1.258-1.288
4	.841- .920	1.321-1.470	1.501-1.650	1.071-1.120	1.433-1.550	1.289-1.352
5	.921- .970	1.471-1.690	1.651-1.800	1.121-1.183	1.551-1.710	1.353-1.402
6	.971-1.015	1.691-1.940	1.801-2.070	1.184-1.260	1.711-1.950	1.403-1.514
7	1.016-1.070	1.941-2.370	2.071-2.550	1.261-1.370	1.951-2.350	1.515-1.650
8	1.071-1.170	2.371-3.370	2.551-3.170	1.371-1.600	2.351-2.800	1.651-1.900
9	1.171-90.0	3.371-90.0	3.171-90.0	1.601-90.0	2.801-90.0	1.901-90.0

Code   Ratio Invervals

Code	7th Digit (R_{62})	8th Digit (R_{61})	9th Digit (R_{54})	10th Digit (R_{53})	11th Digit (R_{21})
0	0-1.133	0-1.255	0- .960	0- .955	0-1.018
1	1.134-1.273	1.256-1.379	.961-1.002	.956-1.021	1.019-1.044
2	1.274-1.380	1.380-1.483	1.003-1.015	1.022-1.049	1.045-1.072
3	1.381-1.502	1.484-1.700	1.016-1.031	1.050-1.095	1.073-1.114
4	1.503-1.720	1.701-2.125	1.032-1.050	1.096-1.160	1.115-1.171
5	1.721-2.150	2.126-2.900	1.051-1.076	1.161-1.263	1.172-1.230
6	2.151-3.000	2.901-4.000	1.077-1.125	1.264-1.450	1.231-1.303
7	3.001-4.000	4.001-5.670	1.126-1.175	1.451-1.692	1.304-1.383
8	4.001-6.500	5.671-9.990	1.176-1.280	1.693-1.933	1.384-1.556
9	6.501-90.0	9.991-90.0	1.281-90.0	1.934-90.0	1.557-90.0

TABLE 14. M-7 SCANNER RATIO CODES FOR SELECTED LABORATORY DATA
FROM THE NASA EARTH RESOURCES SPECTRAL INFORMATION SYSTEM (ERSIS)

Category	Name and Description	ERSIS Curve Number	M-7 Ratio Code
Soils	Clay		
	Alonso type (Puerto Rico)		
	dry	B00830203	753 257 776 76
	wet	205	531 058 878 95
	Quibdo (Gravelly)		
	dry	B00830001	222 234 666 85
	wet	003	333 456 888 97
	Loam (Unspecified)		
	Clarion (Iowa)		
	dry	B00830017	599 998 667 66
	wet	019	299 999 666 54
	Colt's Neck type (New Jersey)		
	dry	B00830049	378 876 886 86
	wet	051	147 766 887 88
	Greenville type (Louisiana)		
	dry	B00830159	257 677 998 99
	wet	161	148 986 988 97
	Loam (Clay Type)		
	Aiken Clay (Oregon)		
	dry	B00830029	444 346 787 79
	wet	031	754 246 776 77
	Blakely Clay (Georgia)		
	dry	B00830183	588 778 888 98
	wet	185	488 777 777 85
	Moaula Light Clay (Hawaii)		
	dry	B00830037	356 467 888 89
	wet	039	158 689 998 98
	Naalehu Heavy Clay (Hawaii)		
	dry	B00830151	345 357 888 89
	wet	153	278 888 889 96
	Loam (Silt Type)		
	Aguan Silt (Honduras)		
	dry	B00830025	555 456 666 68
	wet	027	335 257 655 56
	Herradura Pure Silt (Cuba)		
	dry	B00830021	235 544 785 79
	wet	023	531 346 885 89
	Loam (Silt Type)		
	Zanesville Silt (Indiana)		
	dry	B00830041	466 655 665 69
	wet	043	126 765 675 69
	Loam (Sandy Type)		
	Black Volcanic Sandy (Guatemala)		
	dry	B00830191	478 788 777 77
	wet	193	389 898 666 62
	Ruston Sandy (Georgia)		
	dry	B00830053	267 975 988 96
	wet	055	137 986 888 94

56

TABLE 14. M-7 SCANNER RATIO CODES FOR SELECTED LABORATORY DATA
FROM THE NASA EARTH RESOURCES SPECTRAL INFORMATION SYSTEM
(ERSIS) (Continued)

Category	Name and Description	ERSIS Curve Number	M-7 Ratio Code
Soils	Santa Barbara Gravelly Fine Sandy (Cuba)		
	dry	B00830163	356 765 776 79
	wet	165	113 655 887 98
	Sand		
	Windthorst Type (Oklahoma)		
	dry	B00830199	887 777 777 87
	wet	201	267 888 888 98
	Light Tan Sand with Some Grass (Ft. Walton, Fla.)	A02010101	388 888 778 88
	Gray Sand (Ft. Walton, Fla.)	A02012101	676 666 655 55
	Gray, Washed Pit Sand (Ann Arbor, Michigan)	A02013101	356 555 554 55
Minerals	Silicates		
	Amphibole (Tremolite, St.Lawrence Cty, N.Y.)		
	74- 250 μm	B09000003	321 211 111 12
	250-1200 μm	04	213 111 111 12
	74- 250 μm	07	211 112 213 21
	250-1200 μm	08	410 200 000 03
	Amphibole (Actinolite, Chester, Vermont)		
	74- 250 μm	B09000011	356 740 010 07
	250-1200 μm	12	279 863 130 06
	Amphibole (Actinolite, San Bernardino, Calif.)		
	74- 250 μm	B09000015	367 751 231 15
	250-1200 μm	16	168 850 010 06
	Amphibole (Hornblende, Brewster, N.Y.)		
	74- 250 μm	B09000019	489 875 342 15
	250-1200 μm	20	299 986 445 25
	Amphibole (Hornblende, Clintonville, N.Y.)		
	74- 250 μm	B09000023	899 971 120 05
	250-1200 μm	24	998 741 000 03
	Amphibole (Hornblende, Gore Mountain, N.Y.)		
	74- 250 μm	B09000027	899 975 553 56
	250-1200 μm	28	899 864 333 32
	Andalusite (Australia)		
	74- 250 μm	B09000031	554 544 554 55
	250-1200 μm	32	356 555 555 55
	Anorthoclase (Larvik, Norway)		
	74- 250 μm	B09000035	766 555 554 46
	250-1200 μm	36	876 655 554 46
	Beryl (Maine)		
	74- 250 μm	B09000039	543 531 113 22
	250-1200 μm	40	008 988 999 91
	Biotite (Bancroft, Ontario, Canada)		
	250-1200 μm	B09000043	997 641 340 26
	Chabazite (Colorado)		
	74- 250 μm	B09000045	212 444 444 43

TABLE 14. M-7 SCANNER RATIO CODES FOR SELECTED LABORATORY DATA
FROM THE NASA EARTH RESOURCES SPECTRAL INFORMATION SYSTEM
(ERSIS) (Continued)

Category	Name and Description	ERSIS Curve Number	M-7 Ratio Code
Minerals	Silicates		
	Chlorite (Colorado)		
	74- 250 μm	B09000048	577 764 443 35
	Chlorite (Calaveras County, Calif.)		
	74- 250 μm	B09000052	278 930 000 07
	250-1200 μm	50	455 610 000 05
	Danburite (New York)		
	74- 250 μm	B09000055	864 421 443 45
	250-1200 μm	56	975 411 341 36
	Dumortierite (Pershing County, Nevada)		
	74- 250 μm	B09000059	344 445 435 50
	250-1200 μm	60	225 567 647 60
	Kaolinite (Mesa Alta, New Mexico)		
	74- 250 μm	B09000062	111 112 232 33
	250-1200 μm	63	001 112 392 39
	Kaolinite (Macon, Georgia)		
	74- 250 μm	B09000070	111 123 343 34
	250-1200 μm	71	112 124 444 44
	Montmorillonite (Polkville, Mississippi)		
	74- 250 μm	B09000073	000 113 552 58
	250-1200 μm	74	000 135 676 69
	Montmorillonite (Amory, Mississippi)		
	74- 250 μm	B09000077	346 544 664 68
	250-1200 μm	78	125 533 664 66
	Muscovite (Effingham Township, Ontario, Canada)		
	74- 250 μm	B09000081	225 444 333 34
	Olivine (Forsterite, Crestmore, Calif.)		
	74- 250 μm	B09000089	422 322 332 33
	250-1200 μm	90	322 211 222 23
	Olivine (Fayalite, Jackson County, N.C.)		
	74- 250 μm	B09000093	224 100 131 16
	250-1200 μm	94	433 000 011 16
	Orthoclase (Ruggles Mine, N.H.)		
	74- 250 μm	B09000102	543 234 334 32
	250-1200 μm	103	432 234 434 43
	Plagioclase (Albite, Amelia, Va.)		
	74- 250 μm	B09000106	742 223 223 21
	250-1200 μm	107	642 323 223 31
	Plagioclase (Oligoclase, Norway)		
	74- 250 μm	B09000110	641 222 211 12
	250-1200 μm	111	641 212 222 23
	Plagioclase (Andesine, Montana)		
	74- 250 μm	B09000114	764 444 444 44
	250-1200 μm	115	765 544 444 44
	Plagioclase (Labradorite, New York)		
	74- 250 μm	B09000118	753 421 111 13
	250-1200 μm	119	753 311 111 13

TABLE 14. M-7 SCANNER RATIO CODES FOR SELECTED LABORATORY DATA
FROM THE NASA EARTH RESOURCES SPECTRAL INFORMATION SYSTEM
(ERSIS) (Continued)

Category	Name and Description		ERSIS Curve Number	M-7 Ratio Code
Minerals	Silicates			
	Plagioclase (Bytownite, Minnesota)			
		74- 250 μm	B09000122	654 421 121 13
		250-1200 μm	123	644 101 110 14
	Pyroxene (Augite, Canada)			
		74- 250 μm	B09000126	665 530 120 15
		250-1200 μm	127	777 630.010 05
	Pyroxene (Diopside, New York)			
		74- 250 μm	B09000130	852 400 000 04
		250-1200 μm	131	963 200 000 06
	Pyroxene (Hedenburgite, Montana)			
		74- 250 μm	B09000134	998 776 554 56
		250-1200 μm	135	997 543 342 44
	Pyroxene (Hypersthene, Canada)			
		74- 250 μm	B09000137	975 766 557 65
		250-1200 μm	138	986 976 668 66
	Pyroxene (Bronzite, N.C.)			
		74- 250 μm	B09000141	930 830 234 45
		250-1200 μm	142	930 930 022 47
	Quartz	250-1200 μm	B09000145	742 222 333 33
	Quartz (Milky)			
		149- 250 μm	B09000146	741 322 211 12
		250- 420 μm	147	543 334 334 33
	Serpentine (Missouri)			
		250-1200 μm	B09000155	421 211 000 03
	Talc (North Carolina)			
		74- 250 μm	B09000066	117 378 999 91
		250-1200 μm	67	014 433 997 91
	Oxides and Hydroxides			
	Brucite (Lodi, Nevada)			
		74- 250 μm	B09005003	112 322 223 32
		250-1200 μm	04	001 211 222 33
	Cassiterite (Nigeria)			
		74- 250 μm	B09005007	754 168 779 86
		250-1200 μm	08	521 036 558 62
	Chrysoberyl (South Dakota)			
		74- 250 μm	B09005011	432 333 223 32
		250-1200 μm	12	324 444 344 34
	Corundum (Transvaal, Africa)			
		74- 250 μm	B09005017	321 444 244 32
		250-1200 μm	18	223 655 335 43
	Cuprite (Butte, Montana)			
		74- 250 μm	B09005019	112 777 446 43
		250-1200 μm	20	688 888 768 81
	Diaspore (Rosebud, Missouri)			
		74- 250 μm	B09005024	223 666 556 55
		250-1200 μm	25	113 777 555 55

59

TABLE 14. M-7 SCANNER RATIO CODES FOR SELECTED LABORATORY DATA
FROM THE NASA EARTH RESOURCES SPECTRAL INFORMATION SYSTEM
(ERSIS) (Continued)

Category	Name and Description	ERSIS Curve Number	M-7 Ratio Code
Minerals	Silicates		
	Gibbsite (Brazil)		
	74- 250 μm	B09005028	114 555 556 54
	250-1200 μm	29	000 345 545 54
	Goethite (Biwabik, Minnesota)		
	74- 250 μm	B09005032	987 753 662 66
	250-1200 μm	33	975 432 663 69
	Hematite (Irontown, Minnesota)		
	74- 250 μm	B09005036	888 998 768 80
	Ilmenite (Norway)		
	74- 250 μm	B09005039	975 666 436 40
Minerals	Oxides and Hydroxides		
	Limonite (Tuscaloosa County, Alabama)		
	250-1200 μm	B09005042	389 996 898 99
	Magnetite (Farmington County, Colorado)		
	74- 250 μm	B09005045	963 003 434 50
	Magnetite (Michigan)		
	74- 250 μm	B09005048	985 300 000 00
	Psilomelane (Magdalena, New Mexico)		
	74- 250 μm	B09005050	984 135 436 40
	250-1200 μm	51	984 323 212 10
	Pyrolusite (Villa Grove, Calif.)		
	74- 250 μm	B09005053	577 875 445 45
	250-1200 μm	54	577 863 344 44
	Pyrolusite (Brazil)		
	74- 250 μm	B09005057	998 877 556 51
	250-1200 μm	58	998 877 656 61
	Rutile (Mexico)		
	74- 250 μm	B09005060	676 667 775 78
	250-1200 μm	61	788 689 768 72
	Rutile (Georgia)		
	74- 250 μm	B09005063	488 987 888 97
	250-1200 μm	64	499 998 768 74
	Zincite (Plus Franklinite, N.J.)		
	74- 250 μm	B09005067	999 777 897 89
	250-1200 μm	68	998 568 768 84
	Carbonates		
	Azurite (Bisbee, Arizona)		
	74- 250 μm	B09008003	499 992 000 04
	250-1200 μm	04	289 990 000 00
	Calcite (Mexico)		
	74- 250 μm	B09008006	421 311 101 10
	250-1200 μm	07	531 222 222 22
	Calcite (Cherokee Co., Kan.)		
	74- 250 μm	B09008010	531 212 112 11
	250-1200 μm	12	631 322 222 22

TABLE 14. M-7 SCANNER RATIO CODES FOR SELECTED LABORATORY DATA
FROM THE NASA EARTH RESOURCES SPECTRAL INFORMATION SYSTEM
(ERSIS) (Continued)

Category	Name and Description		ERSIS Curve Number	M-7 Ratio Code
Minerals	Carbonates			
	Dolomite (Mass.)			
		74- 250 μm	B09008015	531 211 111 10
		250-1200 μm	16	321 211 101 10
	Dolomite (New York)			
		74- 250 μm	B09008019	432 222 212 21
		250-1200 μm	20	222 211 212 21
	Magnesite (California)			
		74- 250 μm	B09008023	421 223 223 22
		250-1200 μm	24	310 222 222 23
	Magnesite (Norway)			
		74- 250 μm	B09008026	422 111 221 13
		250-1200 μm	27	222 001 122 23
	Malachite (Arizona)			
		74- 250 μm	B09008030	888 950 000 08
		250-1200 μm	31	666 820 000 07
	Rhodochrosite (Argentina)			
		74- 250 μm	B09008033	532 013 445 54
		250-1200 μm	34	322 003 445 65
	Siderite (Conn.)			
		74- 250 μm	B09008036	988 026 667 77
		250-1200 μm	37	988 004 556 65
	Smithsonite (New Mexico)			
		74- 250 μm	B09008039	432 410 001 12
		250-1200 μm	40	210 200 001 02
	Strontianite (Westphalia)			
		74- 250 μm	B09008041	100 100 000 03
		250-1200 μm	42	333 433 334 33
	Witherite			
		74- 250 μm	B09008044	531 222 223 22
		250-1200 μm	45	422 322 221 23
	Sulphur, Sulfates, and Sulfides			
	Alunite (Utah)			
		74- 250 μm	B09009003	110 333 333 42
		250-1200 μm	04	005 289 999 90
	Arsenopyrite (Utah)			
		74- 250 μm	B09009007	742 321 211 21
		250-1200 μm	08	743 344 324 30
	Barite (Colorado)			
		74- 250 μm	B09009011	765 554 554 64
		250-1200 μm	12	765 655 654 65
	Celestite (Mexico)			
		74- 250 μm	B09009015	543 445 325 31
		250-1200 μm	16	654 456 436 31
	Chalcocite (Montana)			
		74- 250 μm	B09009020	876 830 000 04
		250-1200 μm	21	853 610 000 04

TABLE 14. M-7 SCANNER RATIO CODES FOR SELECTED LABORATORY DATA
FROM THE NASA EARTH RESOURCES SPECTRAL INFORMATION SYSTEM
(ERSIS) (Continued)

Category	Name and Description		ERSIS Curve Number	M-7 Ratio Code
Minerals	Sulphur, Sulfates, and Sulfides			
	Chalcopyrite (Canada)			
		74- 250 µm	B09009024	851 322 555 57
		250-1200 µm	25	741 433 456 59
	Cinnabar (Nevada)			
		74- 250 µm	B09009027	677 677 989 92
		250-1200 µm	28	566 666 879 91
	Cobaltite (Canada)			
		74- 250 µm	B09009031	852 322 213 20
		250-1200 µm	32	854 433 222 12
	Enargite (Peru)			
		74- 250 µm	B09009035	588 984 435 41
		250-1200 µm	36	566 864 332 32
	Galena (Kansas)			
		74- 250 µm	B09009039	951 500 000 00
	Gypsum (Italy)			
		74- 250 µm	B09009042	110 112 212 22
		250-1200 µm	43	100 112 212 21
	Gypsum (Utah)			
		74- 250 µm	B09009046	110 112 111 10
		250-1200 µm	47	000 001 251 19
	Gypsum (New York)			
		74- 250 µm	B09009050	210 212 212 21
		250-1200 µm	51	100 113 213 21
	Jamesonite (Bolivia)			
		74- 250 µm	B09009058	999 876 546 53
		250-1200 µm	59	677 556 546 53
	Jarosite (Nevada)			
		Rough Surface	B09009060	687 876 546 53
	Marcasite (Oklahoma)			
		74- 250 µm	B09009063	886 642 231 14
		250-1200 µm	64	865 642 232 14
	Molybdenite (Utah)			
		74- 250 µm	B09009066	799 998 544 21
		250-1200 µm	67	589 998 546 30
	Niccolite (Canada)			
		74- 250 µm	B09009069	875 555 445 42
		250-1200 µm	70	875 654 432 41
	Proustite (Colorado)			
		74- 250 µm	B09009072	799 899 667 50
		250-1200 µm	73	677 788 657 50
	Pyrargyrite (Nevada)			
		74- 250 µm	B09009075	666 765 323 21
		250-1200 µm	76	654 654 322 21
	Pyrite (Colorado)			
		74- 250 µm	B09009079	765 322 454 48
		250-1200 µm	80	631 101 444 54

TABLE 14. M-7 SCANNER RATIO CODES FOR SELECTED LABORATORY DATA
FROM THE NASA EARTH RESOURCES SPECTRAL INFORMATION SYSTEM
(ERSIS) (Continued)

Category	Name and Description		ERSIS Curve Number	M-7 Ratio Code
Minerals	Sulphur, Sulfates, and Sulfides			
	Pyrrhotite (Canada)			
		74- 250 µm	B09009083	887 678 779 84
		250-1200 µm	84	887 776 657 66
	Realgar (Nevada)			
		74- 250 µm	B09009086	766 566 996 91
		250-1200 µm	87	776 567 998 91
	Sphalerite (Colorado)			
		74- 250 µm	B09009089	114 433 343 36
	Stibnite (Mexico)			
		74- 250 µm	B09009092	899 999 877 40
		250-1200 µm	93	899 999 876 30
	Sulphur (Nevada)			
		74- 250 µm	B09009096	754 444 353 39
		250-1200 µm	97	764 545 475 49
	Thenardite (California)			
		74- 250 µm	B09009101	642 344 324 31
		250-1200 µm	102	642 344 324 31
Rocks	Igneous			
	Andesite (Hornblende, California)			
		420- 500 µm	B09012026	720 100 213 32
	Andesite (Porphyry, Colorado)			
		420- 500 µm	B09012021	830 101 333 42
	Basalt (Oregon)			
		420- 500 µm	B09012028	720 001 001 00
	Basaltic Lava			
		Broken Surface	B09004013	854 444 201 00
	Basaltic Lava			
		Iron Oxide Stained	B09004010	224 135 432 34
	Basaltic Lava		B14004084	970 200 005 40
	Basaltic Lava		A01697001	610 000 001 00
	Diorite (Hornblende, Mass.)			
		420- 500 µm	B09012016	841 101 111 12
	Diorite (Porphyry, Canada)			
		420- 500 µm	B09012018	420 001 212 22
	Felsite (Porphyry, Mass.)			
		420- 500 µm	B09012025	765 543 333 43
	Gabbro (Bytownite, Minn.)			
		420- 500 µm	B09012024	630 101 101 12
	Granite (Biotite, Rhode Island)			
		420- 500 µm	B09012029	865 544 443 53
	Granite (Hornblende, Mass.)			
		420- 500 µm	B09012020	865 543 222 22
	Granodiorite (Minn.)			
		420- 500 µm	B09012017	853 224 334 43

TABLE 14. M-7 SCANNER RATIO CODES FOR SELECTED LABORATORY DATA
FROM THE NASA EARTH RESOURCES SPECTRAL INFORMATION SYSTEM
(ERSIS) (Concluded)

Category	Names and Description		ERSIS Curve Number	M-7 Ratio Code
Rocks	Igneous			
	Obsidian (Oregon)			
		420- 500 μm	B09012022	940 000 001 14
	Peridotite (Mica-augite, Arkansas)			
		420- 500 μm	B09012023	322 101 111 13
	Peridotite (Serpentinite, New York)			
		420- 500 μm	B09012030	410 001 001 12
	Pumice	Broken Surface	B09004011	554 445 555 67
	Rhyolite (Gray, Colorado)			
		420- 500 μm	B09012019	841 114 333 32
	Rhyolite (Pink, Colorado)			
		420- 500 μm	B09012027	853 334 545 54
	Sedimentary and Metamorphic			
	Chert		A00263001	444 555 554 55
	Greenstone		A00261001	246 310 000 04
Vegetation	Grass and Moss			
	Grass (Coarse)		B09004007	119 499 980 07
	Coniferous Trees			
	Pine (Needles)		B09004009	199 399 990 06
	Pine (Red, needles)		B03449007	002 199 999 88
	Pine (Jack, bark)		B01818027	299 999 879 86

TABLE 15. SOURCE DOCUMENTS FOR ERSIS LABORATORY SPECTRA

Document Number	Reference
B00830	Hopkins: Reflectance Curves of Various Soils, USAERDL, Ft. Belvoir, Virginia, ca.1955 (unpublished)
B01175	Derksen, Monahan: A Reflectometer for Measuring Diffuse Reflectance in the Visible and Infrared Regions, J.Opt.Soc.Am., Vol.42, No.4, 1952
B01818	Kronstein: Research, Studies, and Investigations on Spectral Reflectances and Absorption Characteristics of Camouflage Paint Materials and Natural Objects, Final Report, Contract DA-44-009 ENG-1447, New York University, N.Y., March 1955
B03559	Barbrow: Calibration on the Spectral Directional Reflectance of Six Samples of Red Pine Needles, NBS, Test No.G-35201-1, Agricultural Research Center, Beileville, Md., Nov.1964, (unpublished)
B04803	Cooper, Derksen: Spectral Reflectance and Transmittance of Forest Fuel Materials (Final Report), Material Lab., New York Naval Shipyard, Brooklyn, N.Y., March 1952
B09000	Hunt, Salisbury: "Visible and Near-Infrared Spectra of Minerals and Rocks: I. Silicate Minerals," Mod.Geol., Vol.I, 1970, pp.283-300
B09004	Hunt, Ross: "A Bidirectional Reflectance Accessory for Spectroscopic Measurements," Appl.Opt., Vol.6, No.10, Oct.1967, pp.1687-1690
B09005	Hunt, Salisbury: "Visible and Near-Infrared Spectra of Minerals and Rocks: III. Oxides and Hydroxides," Mod.Geol., Vol.II, 1971, pp.195-205
B09008	Hunt, Salisbury: "Visible and Near-Infrared Spectra of Minerals and Rocks: II. Carbonates," Mod.Geol., Vol.II, 1971, pp.23-30
B09009	Hunt, Salisbury: "Visible and Near-Infrared Spectra of Minerals and Rocks: IV. Sulphides and Sulphates," accepted by Mod.Geol. for 1971
B09012	Ross, Adler, Hunt: "A Statistical Analysis of the Reflectance of Igneous Rocks from 0.2 to 2.65 Microns," Icarus, Vol.11, 1969, pp.46-54
A00261	Measured at Environmental Research Institute of Michigan
A00263	Measured at Environmental Research Institute of Michigan
A01521	Measured at Environmental Research Institute of Michigan
A01697	Measured at Environmental Research Institute of Michigan
A01952	Measured at Environmental Research Institute of Michigan
A02010	Measured at Environmental Research Institute of Michigan
A02011	Measured at Environmental Research Institute of Michigan
A02012	Measured at Environmental Research Institute of Michigan
A02013	Measured at Environmental Research Institute of Michigan

TABLE 16. RESULTS OF SEARCHES FOR MATERIALS INSEPARABLE FROM
SEVERAL IRON OXIDES BY M-7 SCANNER RATIO METHODS

Subject of the Search

Name	Curve No.	Ranges of 11-Digit Ratio Code
Goethite (Minnesota)	B09005032 B09005033	9-9,7-8,5-7,4-7,3-5,2-3,6-6,6-6,2-3,6-6,6-9
Hematite (Minnesota)	B09005036	8-8,8-8,8-8,9-9,9-9,8-8,7-7,6-6,8-8,8-8,0-0
Magnetite (Colorado) (Michigan)	B09005045 B09005048	9-9,6-8,3-5,0-3,0-0,0-3,0-4,0-3,0-4,0-5,0-0
Ilmenite (Norway)	B09005039	9-9,7-7,5-5,6-6,6-6,6-6,4-4,3-3,6-6,4-4,0-0
Limonite (Alabama)	B09005042	3-3,8-8,9-9,9-9,9-9,6-6,8-8,9-9,8-8,9-9,9-9

No Objects were found with which the oxides could be confused.

target can be discriminated from approximately 90% of the other materials by a simple threshold in that ratio) or from another specific target (look for the ratio with maximum difference in digits for the two materials to be discriminated).

(2) For predicting false alarm candidates. Once a target ratio code is known and a range of each ratio digit has been selected (to account for sample variability), a search can be made with KOLEKT to determine what materials in the data bank will be confused with the target.

(3) To produce completely automatic recognition maps, these ratio codes can be stored in a computer and used to automatically identify scene elements in scanner imagery.

The major drawback to this collection of M-7 ratio codes is the scarcity of spectral curves in ERSIS which span the whole 0.4-2.5 μm wavelength region and account for large numbers of rocks, minerals, and soils. The ratio codes are quite useful, even if used only to predict which ratio images are best to make a given target the brightest or darkest target in the scene. This is a strong argument for future SR&T support to expand the ERSIS data bank, especially for in-organic natural targets. The expansion,to be of maximum use, should include new measurements of spectral reflectance of such targets from 0.4 to 14 μm. Similar ratio codes have also been calculated for ERTS MSS data with a program called ERAGAL [20].

20. Thomson, F. J., ERIM Progress Report on Use of ERTS-1 Data, Summary of Ten Tasks, Type II Progress Report, Report No. NASA-CR-133556, NTIS No. E73-10899/WR, Environmental Research Institute of Michigan, Ann Arbor, 1973.

6

DESCRIPTION OF A RATIO-GATING LOGIC SYSTEM FOR FUTURE
GEOLOGICAL REMOTE SENSING

The ultimate goal of remote sensing research in several disciplines is to produce a completely automatic system capable of producing automatic recognition maps with little or no
a priori knowledge of the scene being mapped. For some types of remote sensing problems,
as in season-dependent vegetation mapping, this may never be achieved. For some problems,
however, such a system may be achievable in time for use on the space shuttle in the late 1970's.
Many geological targets are practically time-invariant, are more Lambertian than vegetative
canopies, and exhibit spectral features sufficiently unique to warrant the attempt of producing
a completely automatic system.

This section describes a hypothetical logic system, called ratio-gating logic (RAGAL), which
utilizes sequential binary decisions. These binary decisions are based on spectral ratios of
scanner channels that can be made proportional to or equal to ratios of target reflectance spectra measured by laboratory or field spectrometers. Ratio preprocessing will be discussed first,
followed by general descriptions of a preprocessor and automatic recognition map processor
which may be useful for automatic data processing aboard space shuttles or aircraft of the
future.

6.1 RATIO-PREPROCESSING THEORY

The purpose of preprocessing is to suppress spectral effects not related to the chemical
or mineralogical composition of the geological target. Consider first the 0.4-2.5 μm spectral
region, in which most of the radiation exiting from a target on the earth's surface is reflected
solar radiation. For simplicity, geological targets are assumed to be Lambertian (diffuse) reflectors. The spectral radiance of a target measured by a multispectral scanner can be expressed as [21, 22]:

21. Turner, R., W. Malila, and R. Nalepka, Importance of Atmospheric Scattering on Remote Sensing, Or, Everything You've Always Wanted to Know About Remote Sensing but Were Afraid to Ask, Proc., 7th International Symposium on Remote Sensing of Environment, Report No. 10259-1-X, Willow Run Laboratories of the Institute of Science and Technology, The University of Michigan, Ann Arbor, 1971.

22. Vincent, R. K., An ERTS Multispectral Scanner Experiment for Mapping Iron Compounds, Proc., 8th International Symposium on Remote Sensing of Environment, Report No. 195600-1-X, Willow Run Laboratories of the Institute of Science and Technology, The University of Michigan, Ann Arbor, 1972.

ERIM

$$L_\lambda = \frac{1}{\pi}\left[SE_{\lambda_{direct}} + E_{\lambda_{diffuse}}\right]\tau(\lambda)\rho(\lambda) + L_\lambda(path) \tag{14}$$

where L_λ = measured spectral radiance

S = shadow and slope factor (1.0 for no shadow in instantaneous field of view and target surface normal parallel to sun-target direction)

$E_{\lambda_{direct}}$ = direct spectral irradiance of the sun (impinging upon target)

$E_{\lambda_{diffuse}}$ = diffuse spectral irradiance of solar radiation incident on the target from directions other than sun-target direction

$\tau(\lambda)$ = atmospheric transmittance

$\rho(\lambda)$ = spectral reflectance of target

$L_\lambda(path)$ = spectral path radiance (caused by atmospheric scattering)

In Eq. (14), the approximation is made that the target is quasi-Lambertian, with the angular (slope-angle) dependence of the bidirectional reflectance approximately the same for all wavelengths, i.e., S is wavelength-independent. The S-factor also accounts for the amount of shadow in the instantaneous field of view. The $L_\lambda(path)$ term represents path radiance caused when light that has not encountered the target is scattered into the beam between target and detector.

Whenever the $L_\lambda(path)$ term is negligible, as it can be with low altitude aircraft scanner data on a clear dry day, all of the environmental factors are multiplicative. From satellite altitudes, however, $L_\lambda(path)$ cannot generally be neglected. To eliminate most or all of this term, one can take the purely empirical approach of dark object subtraction. A dark material in shadow will be approximately equal to $L_\lambda(path)$, which would represent the lowest possible radiance in the scene. For a given spectral channel, the value of the lowest radiance measured within the scene can be subtracted from all other spatial resolution elements in the scene to approximately correct for path radiance. If all multispectral channels are assumed to be spectrally narrow in the 0.4-2.5 μm wavelength region, the radiance in i-th channel can be given by

$$L(i) \approx L_{\lambda i}\Delta\lambda_i \tag{15}$$

where λ_i is the median wavelength and $\Delta\lambda_i$ is the spectral width (at 50% response points) of the i-th channel. After dark object subtraction, the ratio of the i-th and j-th channels will be approximately equal [20, 21] to:

$$R_{i,j} = \frac{L(i)}{L(j)} \approx \frac{[SE(direct, i) + E(diffuse, i)]\tau(i)\rho(i)}{[SE(direct, j) + E(diffuse, j)]\tau(j)\rho(j)} \tag{16}$$

In Eq. (16), the only terms which should vary widely over most geological test sites are S and $\rho(i)/\rho(j)$, the spectral reflectance ratio of the target. On a clear day of 23 km visibility [21],

69

E(direct, i) is approximately 2.7 times larger than E(diffuse, i) at 0.55μm. For longer wave-lengths, particularly those greater than 0.7μm, the direct illumination term is much more pre-dominant. The smaller the diffuse illumination term, the less does the S-factor, controlled primarily by topographic variations, affects $R_{i,j}$. When the diffuse term is negligible, as it can be for reflective infrared and sometimes for red spectral channels, the S-factor essentially is canceled from the $R_{i,j}$ expression in Eq. (16). Because of this, the $R_{i,j}$ ratio is much more independent of topographic variations across the scene than is the single-channel radiance of Eq. (15).

Although $R_{i,j}$ should be relatively invariant with topographic changes across the scene, it still may not be invariant for a given type of target in two data sets collected at different times in different places. For a further suppression of environmental factors [E(sun, i) = SE(direct, i) + E(diffuse, i), τ(i), and L(path, i)] one can measure the spectral reflectance of a known target within the test area and use it as a reference, for which the scanner-measured ratio would be:

$$(R_{i,j})_{reference} = \frac{E(sun, i)}{E(sun, j)} \frac{\tau(i)}{\tau(j)} \left[\frac{\rho(i)}{\rho(j)}\right]_{reference} \tag{17}$$

A division of Eq. (16) by Eq. (17) yields, after rearrangement, the corrected ratio

$$R_{i,j}^{c} = \left[\frac{R_{i,j}}{(R_{i,j})reference}\right]\left[\frac{\rho(i)}{\rho(j)}\right]_{reference} = \frac{\rho(i)}{\rho(j)} \tag{18}$$

which is equal to the spectral reflectance ratio of the target, almost independently of environmental factors. The "almost" is included in the foregoing statement because the degree of environmental independence is a function of how well the dark object subtraction succeeds in suppressing the path radiance term. If shadows are present over materials of varying bright-ness, a more vigorous determination of L_λ(path) can be made, but with greater cost in time and human interaction [23].

ERTS-1 data [24] have been used to show experimentally that both $R_{i,j}$ (uncorrected) and $R_{i,j}^{c}$ are more independent of atmospheric and solar illumination effects than single-channel radiances. With the same data it was also shown that sky and sun effects produce a standard deviation in $R_{i,j}^{c}$ of approximately 10% or less. Appendix D is a reprint of the part of Reference [24] that addresses these points. A recent study with aircraft data [24] successfully used laboratory spectra as training sets for geologic mapping; and another investigation [25] showed that Equa-

23. Piech, K. R., and J. E. Walker, Interpretation of Soils, Photogram. Engin., Vol. XL, 1974, pp. 87-94.

24. Thomson, F. J., ERIM Progress Report on Use of ERTS-1 Data, Summary of Ten Tasks, Type I, Report No. 193300-24-L, NASA Contract NAS5-21783, Environmental Research Institute of Michigan, Ann Arbor, 1973.

25. Dillman, R. and R. K. Vincent, Unsupervised Mapping of Geologic Features and Soils in California, Proc. of the Ninth Symp. for Remote Sens. of Environ., Ann Arbor, Mich., 1974, (In Press).

tion (18) produced, between six ratios calculated from laboratory spectra and ratios computed from ERTS MSS data [26], an agreement of better than 10% for four exposed geologic targets (hematitic red beds, granite, greenstone, and magnetite) in Wyoming.

Concerning aircraft data, another task (Signature Extension) in this NASA contract has shown [27] that ratios of adjacent channels are more extendible in time and space than un-transformed single-channel radiances. The ratio normalization step of Eq. 18 is useful for extending recognition results in time and space, but does not help discrimination among targets on a relative basis within a given flight line or ERTS frame. However, normalization is necessary for absolute ratio work, where laboratory data are used as training sets. It is possible in the future that the multiplicative atmospheric terms in Eq. (17) can be estimated from an atmospheric model, alleviating the need for ratio normalization via Eq. (18).

The methods described above for suppressing environmental "noise" will also suppress both additive and multiplicative electronic offset and gain variations between sets of data gathered at different times and places, which can occur even when the same scanner system is employed for each data collection mission. For these reasons, the preprocessing requirements for geological remote sensing in the 0.4 to 2.5 μm region are dark object subtraction (for satellite and high altitude aircraft data) and ratio normalization for all data, if either absolute ratio values or extension of recognition results over data sets separated in space and time are called for.

Now consider the 8-14 μm wavelength region, in which most of the radiation exiting from a target on the earth's surface is emitted by the target itself. The reasons for ratio preprocessing in the thermal wavelength region are more complicated. A ratio of two infrared channels has been found [3] to suppress temperature variations across the scene and to show emittance variations indicative of silicate rock type. To make an estimation [28] of how greatly temperature is suppressed, two rocks will be assumed to have emittance differences $\Delta\epsilon(\lambda_1)$ and $\Delta\epsilon(\lambda_2)$ at the center wavelengths (λ_1 and λ_2) of a two-channel infrared scanner. The temperature difference (ΔT) between two spectrally identical rocks which would be confused with these emittance differences will be determined for both a single channel and for a ratio of two channels. Consider Wien's approximation of Planck's law which, for $T \approx 300^\circ K$, comes to within 2% of the spectral radiance at wavelength λ for a target of temperature T, omitting atmospheric effects:

$$L_\lambda(T) = \epsilon(\lambda)\frac{2hc^2}{\lambda^5}\exp\left(-\frac{hc}{\lambda kT}\right) \tag{19}$$

26. Salmon, B. and R. K. Vincent, Surface Compositional Mapping in the Wind River Range and Basin, Wyoming by Multispectral Techniques Applied to ERTS-1 Data, Proceedings of the Ninth Symposium for Remote Sensing of Environment, Ann Arbor, Mich., 1974 (In Press).

27. Vincent, R. K., G. Thomas, and R. Nalepka, Signature Extension Studies, Report No. 190100-26-T, NASA Contract NAS9-9784, Environmental Research Institute of Michigan, Ann Arbor, (In Press).

28. R. K. Vincent, A Thermal Infrared Ratio Imaging Method for Mapping Compositional Variations Among Silicate Rock Types, Ph.D. Dissertation, Department of Geology and Mineralogy, The University of Michigan, Ann Arbor, 1973.

where c is velocity in light, h is Planck's constant, and k is Boltzmann's constant. The change in spectral radiance caused by changes in T and $\epsilon(\lambda)$ can be found by taking the differential of $L_\lambda(T)$ to yield

$$\Delta L_\lambda(T) = \frac{2hc^2}{\lambda^5} \exp\left(-\frac{hc}{kT\lambda}\right)\left[\Delta\epsilon(\lambda) + \epsilon(\lambda)\frac{hc}{\lambda kT}\frac{\Delta T}{T}\right] \qquad (20)$$

To find what temperature difference ΔT between two spectrally identical targets is equivalent to a difference $\Delta\epsilon(\lambda)$ in emittance between two spectrally dissimilar targets of the same temperature, $\Delta L_\lambda(T)$ must be set to zero:

$$\Delta T_{\text{Single Channel}} = -\frac{\Delta\epsilon(\lambda)}{\epsilon(\lambda)}\frac{kT^2}{hc}\lambda \qquad (21)$$

This is the answer sought for a single channel.

Consider now the ratio of spectral radiances at two wavelengths:

$$R_{1,2} = \frac{L_{\lambda_1}(T)}{L_{\lambda_2}(T)} \cong \frac{\epsilon(\lambda_1)}{\epsilon(\lambda_2)}\left[\left(\frac{\lambda_2}{\lambda_1}\right)^5 \exp\left\{\frac{hc}{kT}\left(\frac{1}{\lambda_2} - \frac{1}{\lambda_1}\right)\right\}\right] \qquad (22)$$

A similar procedure will be followed, i.e., the differential of $R_{1,2}$ will be determined and set to zero. The differential of $R_{1,2}$ is given by

$$\Delta R_{1,2} = \frac{1}{\epsilon(\lambda_2)}\left(\frac{\lambda_2}{\lambda_1}\right)^5 \exp\left\{\frac{hc}{kT}\left(\frac{1}{2} - \frac{1}{\lambda_1}\right)\right\}\left[\Delta\epsilon(\lambda_1) - \frac{\epsilon(\lambda_1)}{\epsilon(\lambda_2)}\Delta\epsilon(\lambda_2) - \frac{hc}{kT^2}\Delta T\epsilon(\lambda_1)\left(\frac{1}{\lambda_2} - \frac{1}{\lambda_1}\right)\right] \qquad (23)$$

Setting $\Delta R_{1,2}$ to zero yields

$$\Delta T_{\text{Ratio}} = \frac{kT^2}{hc}\frac{\lambda_1\lambda_2}{\lambda_1 - \lambda_2}\left[\frac{\Delta\epsilon(\lambda_1)}{\epsilon(\lambda_1)} - \frac{\Delta\epsilon(\lambda_2)}{\epsilon(\lambda_2)}\right] \cong \frac{kT^2}{hc}\frac{\Delta\epsilon(\lambda_1)}{\epsilon(\lambda_1)}\frac{2\lambda_1\lambda_2}{\lambda_1 - \lambda_2} \qquad (24)$$

where it has been assumed that $[\Delta\epsilon(\lambda_2)/\epsilon(\lambda_2)] = [\Delta\epsilon(\lambda_1)/\epsilon(\lambda_1)]$, because silicate rocks generally differ from one another approximately in this manner, i.e., the emittance minimum occurs at longer wavelengths for more mafic rocks, which cause a mafic rock to have a lower emittance at λ_2 and a higher emittance minimum at λ_1 than a felsic rock.

To get a comparison between single channel and ratio capabilities for mapping emittance variations in the presence of temperature variations across the second scene, Eq. 24 can be divided by Eq. 21 and the quotient solved for ΔT_{Ratio} to yield

$$\Delta T_{Ratio} = \frac{2\lambda_2}{\lambda_1 - \lambda_2} \Delta T_{Single\ Channel} \tag{25}$$

This equation states that for the same percentage variation in emittance at λ_1, $[\Delta \epsilon (\lambda_1)/\epsilon (\lambda_1)]$ (with an equal but negative emittance variation at λ_2), the ratio would require a temperature difference that is larger by a factor of $2\lambda_2/(\lambda_1 - \lambda_2)$ than the single-channel temperature difference required to mask the same emittance variation. From Eq. 24, it would take a $10.4^{\circ}K$ (or larger) difference in temperature between two identical targets to mask a 1% emittance difference, where

$$\frac{\Delta \epsilon (\lambda_1)}{\epsilon (\lambda_1)} = -\frac{\Delta \epsilon (\lambda_2)}{\epsilon (\lambda_1)} = 0.01$$

between two rocks that are both at a temperature of $300^{\circ}K$ in an $R_{1,2}$ ratio, where the center wavelengths of $9.5\mu m$ and $10.7\mu m$ were used to approximate channels 1 and 2 of ERIM's two-channel infrared detector. This 1% emittance difference is estimated to be on the order of 10% of the total range of $\Delta \epsilon (\lambda_1)/\epsilon (\lambda_1)$ for silicate rocks. From Eq. (21) it takes a ΔT of only $0.6^{\circ}K$ to mask the same 1% emittance difference between two targets in a single channel at $9.5\mu m$. Therefore, $R_{1,2}$ suppresses temperature variations across the scene for silicate rocks by a factor of approximately $2\lambda_2/(\lambda_1 - \lambda_2)$, which for channels 1 and 2 is about a factor of 18 better than a single-channel radiance. Although these results are for narrow spectral channels at λ_1 and λ_2, integration over broader spectral regions was found to yield approximately the same numerical results.

For the case where atmospheric effects in the thermal spectral region are negligible (such as with low-altitude aircraft data collected on a clear, dry day), a ratio of radiances in the two spectral bands greatly suppresses target temperature, and depends only on emittance variations. Under other conditions, the ratio of radiances still tends to suppress variations in target temperature across the scene. Therefore, a ratio of radiances is useful for enhancing compositional variations among silicates, even in the presence of limited temperature variations ($\Delta T \leq 10^{\circ}K$) from rock to rock.

Even though a ratio of two infrared channels suppresses temperature variations across the scene, there is still a need to correct $R_{1,2}$ for temperature, if absolute values of $R_{1,2}$ are important. A method for doing this [28] has been developed for low altitude aircraft data, which utilizes the fact that the spectral emittances of almost all silicate rocks in the 11.75-13.75 μm region are approximately equal. An infrared channel in this wavelength region can be used to estimate the temperature of the instantaneous field of view within $\pm 5^{\circ}K$. The correction factor to be multiplied times $R_{1,2}$ is determined from a table look-up, once the radiance in the

11.75-13.75 μm region is known. Therefore, the preprocessing requirements for thermal infrared data are to form ratios of radiances for various pairs of available infrared scanner channels, determine a multiplicative correction factor from radiance detected by a 11.75-13.75 μm channel, and multiply the ratio times the correction factor to obtain a temperature-corrected ratio [28]. For satellite data it would be necessary, because of the long atmospheric path, to correct the single-channel radiances before forming the ratio. For this case, which will be discussed in the next section, it could be argued that ratios lose their advantage of temperature suppression over single-channel radiances. However, ratios of thermal infrared channels and ratios of 0.4-2.5 μm channels are more compatible than single-channel radiances from the emissive and reflective wavelength channels. Also, some evidence exists [26] that ratios are better than single-channel radiances in the 8-14 μm region for separating igneous rocks, even if all are at the same temperature, possibly because of the suppression of textural effects by the ratios.

6.2 GENERAL DESCRIPTION OF PREPROCESSOR

A preprocessor that could perform ratio preprocessing automatically from future satellites and high altitude aircraft platforms is suggested in Figure 17. The ideas covered below are general, but the termination of this NASA SR&T task warrants their discussion. Further research would be required to make them more specific.

VISIBLE-REFLECTIVE IR SIGNALS FROM MULTISPECTRAL SCANNER
Raw signals from the reflective channels are input to the preprocessor.

ELECTRONIC GAIN AND OFFSET CORRECTION FOR REFLECTIVE CHANNELS
The signals are converted to radiances and enter the detectors via calibration lamps. [Note: This step is required only by the modules entitled "Determination of Ratio Normalization Factors" and "Atmospheric Model for Thermal Corrections" of Figure 17 as discussed below.]

SEARCH FOR DARK OBJECT RADIANCES
After editing for noisy data points, the IFOVs (instantaneous fields of view) in the scene with the minimum sum of radiances detected in all reflective channels for a portion of the scanned scene are selected as the darkest objects. The lowest radiance in each channel from the minimum-sum IFOVs becomes the dark object radiance for that channel. [Better methods than the minimum sum should be sought.]

```
┌─────────────────────┐   ┌───────────┐   ┌─────────────────────┐
│ Visible-Reflective IR│   │ Ancillary │   │ Thermal Signals     │
│ Signals from Multi- │   │ Data      │   │ from Multi-         │
│ spectral Scanner    │   │           │   │ spectral Scanner    │
└─────────────────────┘   └───────────┘   └─────────────────────┘
          │                     │                     │
          ▼                     │                     ▼
┌─────────────────────┐         │         ┌─────────────────────┐
│ Electronic Gain and │         │         │ Electronic Gain     │
│ Offset Corrections  │         │         │ Corrections for     │
│ for Reflective      │         │         │ Thermal Channels    │
│ Channels            │         │         │                     │
└─────────────────────┘         │         └─────────────────────┘
          │                     │                     │
          ▼                     ▼                     ▼
┌─────────────────┐   ┌──────────────────┐  ┌─────────────┐
│ Search for Dark │──▶│ Atmospheric Model│─▶│ Atmospheric │
│ Object Signals  │   │ for Thermal      │  │ Correction  │
│                 │   │ Corrections      │  │             │
└─────────────────┘   └──────────────────┘  └─────────────┘
          │                                        │
          ▼                                        ▼
┌─────────────────┐  ┌────────────────┐  ┌──────────────────┐  ┌─────────────┐
│ Dark Object     │─▶│ Ratio Normaliza-│  │ Radiance-Versus  │─▶│ Temperature │
│ Subtraction and │  │ tion Factor    │  │ Temperature Table│  │ Correction  │
│ Formation of    │  │ Determination  │  │                  │  │             │
│ Ratios          │  │                │  └──────────────────┘  └─────────────┘
└─────────────────┘  └────────────────┘                               │
          │                 │                                         ▼
          ▼                 │                                  ┌─────────────┐
┌─────────────────┐◀────────┘                                 │ Ratio       │
│ Ratio           │◀────────────────────────────────────────  │             │
│ Normalization   │                                           └─────────────┘
└─────────────────┘
                    ┌──────────────────┐
                    │ Corrected Ratios │
                    └──────────────────┘
```
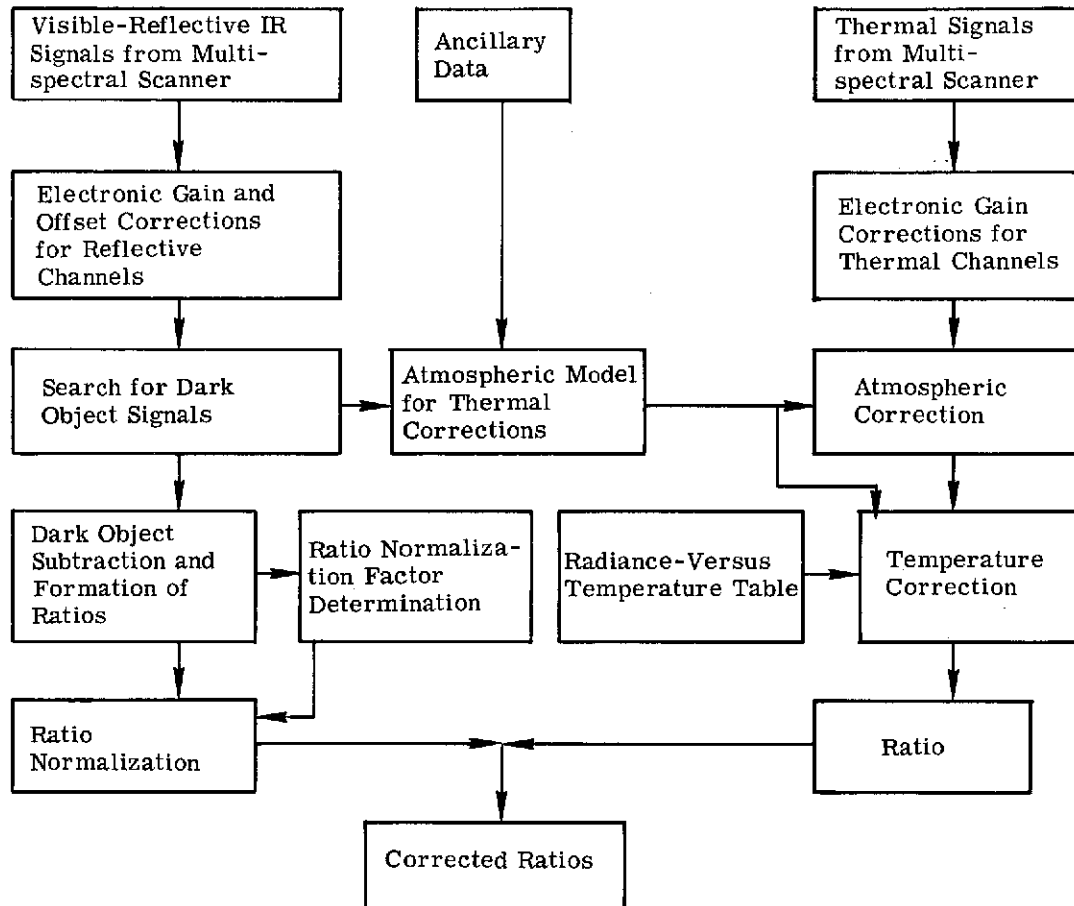
FIGURE 17. SCHEMATIC OF RATIO PREPROCESSOR

DARK OBJECT SUBTRACTION AND FORMATION OF RATIOS

The dark object radiance is subtracted from radiances of all IFOVs for each channel, and all possible ratios of channel pairs are calculated.

DETERMINATION OF MULTIPLICATIVE RATIO NORMALIZATION FACTORS

While each instantaneous field of view (IFOV) is undergoing ratioing (after dark object subtraction), the resulting ratios should be checked for qualitative ratio patterns similar to ratio patterns of common, but fairly unique targets. For instance, hematite (a common iron oxide) may have one or more ratios formed by the particular scanner system of interest that is much higher than the average ratio across the scene. (Note: This is the case for several M-7 scanner ratios, as shown in the previous section). If the pattern for several IFOVs compared with the average signal in the scene matches that of hematite, the stored ratios for hematite (from lab or field spectra) can be used to normalize the ratios calculated from the previous step to absolute values of target reflectance ratios for those IFOVs. The normalization (multiplicative) factors required to do this would then become inputs to the next step. The determination of ratio normalization factors could probably best be determined by a priori knowledge of part of the scanned scene. This would require man-machine interface and would slow the preprocessing steps, but may be necessary for accuracy. Accuracy of the purely automatic method may be improved if more than one distinctive target can be selected. The process then becomes a bootstrapping one to determine the best normalization factors.

RATIO NORMALIZATION

Each ratio is multiplied by the ratio normalization factor to yield a corrected ratio equal to the ratio of target reflectances in the two channels comprising the ratio.

ANCILLARY DATA

The altitude of the aircraft or spacecraft, solar zenith angle with respect to the target, and thermal profile of the atmosphere as measured by thermal channels in atmospheric absorption bands are recorded.

THERMAL SIGNALS FROM MULTISPECTRAL CHANNELS

Raw signals from the thermal infrared channels are input to the preprocessor.

ELECTRONIC GAIN AND OFFSET CORRECTION FOR THERMAL CHANNELS

The signals are converted to radiances entering the detectors by means of hot and cold calibration plates.

ERIM

ATMOSPHERIC MODEL FOR THERMAL CORRECTIONS

With the ancillary data and atmospheric path radiances determined from dark object sub-traction in the reflective wavelength regions as inputs, an atmospheric model may be used to calculate atmospheric path radiance, L(path, i), sky irradiance, E(sky, i), and transmittance, $\tau(i)$, in each of the i thermal channels being used for target monitoring (in atmospheric windows). Although an atmospheric model exists [16] which can predict these thermal infrared parameters for given atmospheric conditions, it currently cannot use the suggested ancillary data and re-flective channel path radiance to assess atmospheric conditions. This is a needed research effort.

ATMOSPHERIC CORRECTION

For the i-th channel, the detected target radiance, L''(i, T), is input from the "Electronic Gain and Offset Corrections for Thermal Corrections" module. The detected radiance in the i-th channel for a Lambertian target can be written as

$$L''(i, T) = \int_0^\infty L_\lambda''(T)f(i, \lambda)d\lambda = \int_0^\infty \tau(\lambda)\left[\epsilon(\lambda)\left\{L_\lambda(bb, T) - \frac{E_\lambda(sky)}{\pi}\right\} + \frac{E_\lambda(sky)}{\pi}\right]f(i, \lambda)d\lambda$$

$$+ \int_0^\infty L_\lambda(path) f(i, \lambda)d\lambda \approx \tau(i)\left[L(bb, i, T) - \frac{1}{\pi}E(sky, i)\right]\int_0^\infty \epsilon(\lambda)f(i, \lambda)d\lambda \quad (26)$$

$$+ \frac{E(sky, i)}{\pi}\tau(i) + L(path, i)$$

where $f(\lambda, i)$ is the spectral responsivity of the i-th channel

$L_\lambda(bb, T)$ is the blackbody spectral radiance at target temperature T at wavelength λ, and the assumption has been made that $L_\lambda(bb, T)$, $E_\lambda(sky)$, $\tau(\lambda)$, and $L_\lambda(path)$ are slowly varying functions of λ over the bandwidths ($\approx 1\mu m$ suggested) of the thermal channels, such that they can be approximated by their averages [L(bb, i, T), E(sky, i), $\tau(i)$, and L(path, i)] over the i-th bandwidth

The atmospheric parameters from the atmospheric model module can be · ed to subtract the last two terms from Eq. (26) to yield

$$L'(i, T) = \frac{1}{\tau(i)}[L''(i, T) - L(path, i)] - \frac{E(sky, i)}{\pi} = \left[L(bb, i, T) - \frac{E(sky, i)}{\pi}\right]\int_0^\infty \epsilon(\lambda)f(i, \lambda)d\lambda$$

$$(27)$$

Equation (27) is the algorithm for this module.

RADIANCE VERSUS TEMPERATURE TABLE LOOK-UP

This table relates L(bb, m, T), the radiance of a blackbody at temperature T in the m-th thermal channel (to be defined in the next module), to L(bb, i, T), the radiance of a blackbody at the same temperature in another i-th thermal channel. The L(bb, m, T) and L(bb, i, T) are calculated from Planck's equation:

$$L(bb, i, T) = 2c^2 h \int_0^\infty \frac{f(i, \lambda)}{\lambda^5 [e^{-(hc/\lambda 1 T)} - 1]} d\lambda \qquad (28)$$

where c is velocity of light, h is Planck's constant, and k is Boltzmann's constant. This equation provides the necessary L(bb, m, T) versus T and L(bb, i, T) versus T relationships to form the table look-up.

TEMPERATURE CORRECTION

In some spectral regions in the thermal infrared, spectral emittances, $\epsilon(\lambda)$, of silicates (the most common rocks and soils) are practically uniform [28]. If the m-th thermal channel encompasses one of those regions, where $\epsilon(\lambda) \approx \epsilon_c$ = constant for most rocks and soils, Equation (27) can be solved for L(bb, m, T) for each IFOV in the scene to yield

$$L(bb, m, T) = \frac{L'(m, T)}{\epsilon_c} + \frac{E(sky, m)}{\pi} \qquad (29)$$

Since L'(m, T) comes from the atmospheric correction module, E(sky, m) comes from the atmospheric model module, and ϵ_c is known from laboratory data, L(bb, m, T) can be calculated from Eq. (29). The Radiance-Temperature Table is used to determine L(bb, i, T) for the i-th channel. Since E(sky, i) is known from the atmospheric model module, the finally corrected radiance in the i-th channel is given by

$$L(i) = \frac{L'(i, T)}{\left[L(bb, i, T) - \frac{E(sky, i)}{\pi} \right]} = \int_0^\infty \epsilon(\lambda) f(i, \lambda) d\lambda \qquad (30)$$

This is the algorithm for the "Temperature Correction" module. As shown in Section 6.1, the temperature correction need only be good to within approximately 5°K to be useful for thermal ratioing.

RATIO

All possible thermal ratios are formed, of the type represented by the equation

$$R_{ij} = \frac{L(i)}{L(j)} \qquad (31)$$

which is the corrected ratio. The R_{ij} of the thermal and reflective channels are compatible and fully corrected at this stage.

6.3 GENERAL DESCRIPTION OF THE AUTOMATIC RECOGNITION MAP PROCESSOR

Figure 18 shows a schematic of a suggested, automatic recognition map processor with stored ratio code training sets. Except for the Preprocessor, discussed in the previous section, each box in the schematic is briefly discussed below. There are two paths through the Automatic Recognition Map Processor: one for remote sensing experiments in which a set of pre-selected target classes is to be mapped and the other for mapping groups of materials in the scene which can be discriminated from one another, with identification of each group subsequent to the mapping procedure.

RATIO CODE STORAGE

Ratio codes are described in Section 5. This module, which stores the ratio codes calculated from reflectance and emittance ratios of laboratory or field spectra, is the heart of the Automatic Recognition Map Processor because it feeds both routes of logic. If the multispectral scanner has n channels, then $[n(n - 1)]/2$ non-reciprocal ratios can be calculated for each possible target material. Therefore the ratio codes will be in the form of $[n(n - 1)]/2$-digit numbers. Each digit position ranges from 0 to 9 as suggested in Section 5, but if greater accuracy were justified, the ratio code could be doubled in length to give each ratio a 0 to 99 code range.

USER SELECTION OF TARGETS

For the pre-selected target route, the user specifies the targets for which he is searching. [Note: this should be especially useful for mineralogical exploration.] The user would also specify the general type of terrain, i.e., arid, tropical, urbanized, etc.

HIERARCHY SELECTOR

The purpose of the Hierarchy Selector is to find the most efficient sequence of binary decisions. For a given target preselected by the user, the ratio code for that target is scanned from left to right to search for the first ratio with a code of 9 or 0, which would mean that simple thresholding of that ratio would separate the desired target from 90% of the other materials represented in the Ratio Code Storage. For each remaining ratio the target class code (or range of ratio codes) is compared with the codes of the false alarm candidates not eliminated by the first ratio. The ratio which eliminates the most remaining false alarm candidates is chosen second. This procedure is iterated on the false alarm candidates not eliminated by the previously chosen ratios.
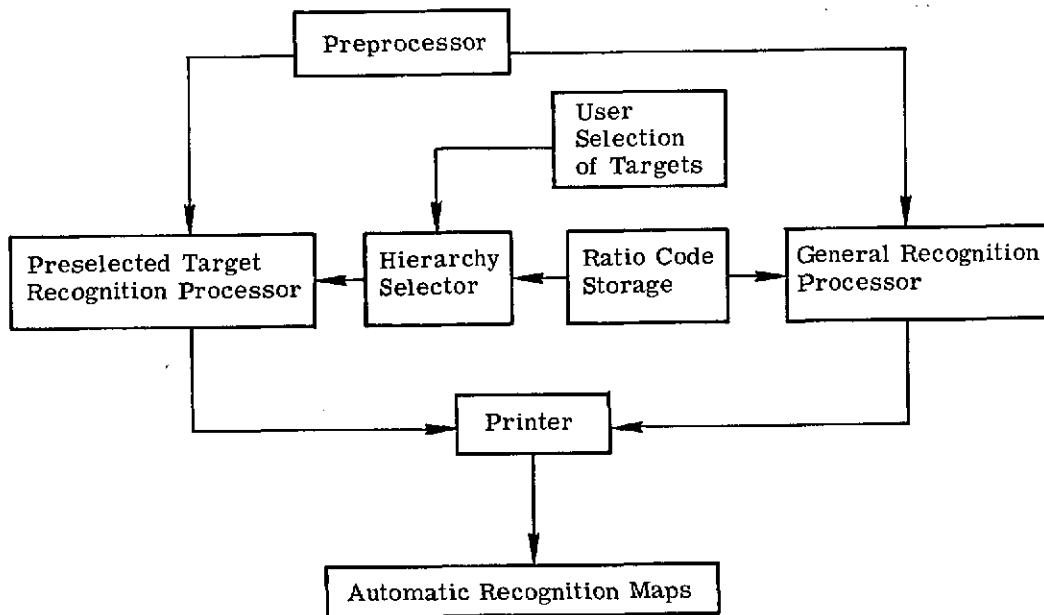
FIGURE 18. SCHEMATIC OF AUTOMATIC RECOGNITION MAP PROCESSOR WITH STORED
RATIO CODE TRAINING SETS

the remaining "look-alikes" of the selected target, if any, are communicated to the user, who decides whether they are acceptable false alarms. The ratios (and their thresholding or gating limits) become the logic hierarchy for that target. The other preselected targets are treated similarly. If any two preselected targets are false alarm candidates for each other, this is communicated to the user, who must eliminate one or the other.

Priorities for the final sequence of ratio thresholds and gates for each target are set according to the probability of occurrence* for each target in the scene to be mapped; the target expected to be encountered most is placed first, etc. The resulting hierarchy is one of the most efficient sequence of binary decisions available. Different ratios can be used for different targets. Thresholding is preferred to gating, whenever possible, because the setting of only one boundary should result in fewer false alarms. An example of how the logic hierarchy might appear is shown in Table 17. At some expense in classifying time, all ratios for which the target class exhibits a code of 9 or 0 could be exhausted before the difference of the means was invoked as a ratio selection device.

PRESELECTED TARGET RECOGNITION PROCESSOR

The logic sequence determined in the Hierarchy Selector becomes the logic algorithm for the Preselected Target Recognition Processor module. For each IFOV in the scene, those ratios called for in the logic sequence for target 1 are tested to see if they comply with the target 1 ratio ranges. If so, that IFOV is recognized as target 1 and the next IFOV is processed. If the first IFOV does not comply with any one of the ratio ranges for target 1, however, it is tested for compliance with target 2, etc. If it complies with no preselected targets, it is labeled "Unrecognized." This recognition processor is a sequence of binary decisions based on ratio gating; hence, it is called ratio gating logic (RAGAL).

GENERAL RECOGNITION PROCESSOR

For mapping unknown terrain with no preselection of targets, the General Recognition Processor would be used. There are three likely candidates for logic algorithms. The first is RAGAL, which could operate in the following manner. For each IFOV, a reflective infrared to visible red ratio would be thresholded to separate vigorous vegetation (high ratio) from dormant vegetation and non-vegetation targets (low ratio). If geological targets are of primary interest, the vigorous vegetative targets would all be classified as one group. If the IFOV is not vigorous vegetation, one of the thermal infrared ratios composed of channels inside and outside the emittance minimum region (8-12 μm) of silicates, would be used to decide whether the material was silicate. If so, a ratio composed of two channels inside the silicate emittance minimum

*This could come from the user's general description of the scene and stored weighting factors, which are normalized probable frequencies of occurrence in the scene, as determined from theoretical models of various scene categories.

region would be used to determine whether the target is felsic, intermediate, mafic, or ultramafic. The next step might be thresholding of a red-to-green ratio to separate out rocks with appreciable surface area covered by ferric oxides (a high red-to-green ratio). Further subdivision of the silicate rocks should become possible as more studies of laboratory spectra are conducted. The non-silicates, separated from silicates in the first step above, could be tested for large surface area coverage by ferric oxides with the red-to-green ratio and then for carbonate or non-carbonate composition via two ratios—one a thermal ratio involving the 11.0-11.5 μm wavelength region and another thermal channel (12.0-12.5 μm, for instance), and the other ratio involving 2.0-2.2 μm and 2.2-2.5 μm reflective infrared channels. These ratios would capitalize on a carbonate emittance minimum in the 11.3μm region and two carbonate reflectance minima in the 2.2-2.5 μm wavelength region. More laboratory studies should result in further specific categorizations of non-silicate geologic targets.

A second logic algorithm possibility for the General Recognition Processor is a combination of unsupervised clustering and ratio code identification. Unsupervised clustering discriminates among targets with different spectral properties. If this clustering were done in ratio space, i.e., on the basis of ratio inputs, the means and standard deviations of the resulting clusters could be assigned ratio codes and the ratio code storage could be searched for geologic targets that have the same codes as each of the target clusters. The disadvantage of unsupervised clustering is that the user has little or no control over what target clusters will evolve. Though the clustering addresses the question "What target classes provide the greatest spectral contrasts among themselves?" the question of perhaps greatest interest to the user is "What meaningful targets can be uniquely discriminated?" Both questions have their place in remote sensing problems, however, and it may be wiser to include both unsupervised clustering and RAGAL in the General Recognition Processor.

A third candidate for a logic algorithm is what may be called ratio parameterization. It involves the linear combination of various spectral ratios to predict a parameter that is physically meaningful to the user. Some theoretical work has already been accomplished along these lines. In a recent thesis [28], a mineralogical parameter was defined (called V_7) which corresponds well with an accepted igneous rock chart by Travis [29]. This parameter varies continuously between 100 and 0 as one moves from left to right across the rock chart. Table 18 shows the ranges of V_7 associated with ten rock classifications on Travis' chart. The 8-14 μm

29. R. B. Travis, Classification of Rocks, Quarterly of the Colorado School of Mines, Vol. 50, No. 1, 1955, p. 12.

TABLE 17. HYPOTHETICAL EXAMPLE OF A LOGIC SEQUENCE
CHOSEN BY THE HIERARCHY SELECTOR

Target No.	Normalized Probable Frequency of Occurrence in Scene	Logic Sequence
1	0.90	(1A) $R_{41} \geq 2.20$
		(1B) $R_{52} \leq 0.42$
		(1C) $R_{97} \leq 0.21$
		(1D) $2.10 \geq R_{65} \leq 2.40$
2	0.62	(2A) $R_{62} \geq 3.12$
		(2B) $R_{31} \geq 4.23$
3	0.21	(3A) $R_{75} \leq 0.18$
4	0.05	(4A) $0.85 \leq R_{84} \leq 1.10$
		(4B) $1.20 \leq R_{63} \leq 1.30$
		(4C) $1.9 \leq R_{76} \leq 2.04$

TABLE 18. LIMITS OF V_7 FOR ROCK GROUPS
(Based on Travis' Igneous Rock Chart)

Name	Group Equigranular Member	V_7 Limits
A	Granite	100-84
B	Syenite	84-81
C	Nepheline Syenite	81-80
D	Quartz Monzonite	80-67
E	Monzonite	67-66
F	Nepheline Monzonite	66-65
G	Granodiorite	65-47
H	Quartz Diorite and Diorite	47-37
I	Gabbro, Diabase, and Theralite	37-18
J	Peridotite	18-0

wavelength region was arbitrarily divided into twelve hypothetical 0.5μm-wide "channels" and, with laboratory spectra of twenty-six igneous rocks as a basis, a linear combination of seventeen emittance ratios from eleven of these channels was found which predicts V_7 within a standard error of 7.10 out of a possible range of 0 to 100. That result was probably not optimum, and it did not make use of wavelength regions outside 8-14 μm. However, it demonstrated that ratio parameterization methods can be useful for identifying geologic targets.

PRINTER

The output of both recognition processors would be used to print color automatic recognition maps.

6.4 CONCLUSIONS

A possible system for producing automatic recognition maps aboard space-shuttle and high-altitude aircraft has been outlined. Ratio preprocessing steps were described for both reflective and thermal infrared scanner channels. The reflective channel signals would undergo dark object subtraction and ratio normalization to an easily identifiable reference in the scene. Thermal infrared channel signals inside atmospheric windows would be corrected for atmospheric effects by an atmospheric model, with atmospheric conditions assessed by dark object radiances determined for the reflective channels and atmospheric thermal profiles measured by infrared channels outside atmospheric windows. A thermal channel in a spectral region where silicate targets show little emittance contrast and an atmospheric model would be used to correct the single-channel thermal radiances for temperature variations across the scene. Corrected spectral ratios for both reflective and thermal channels would result from these preprocessing steps.

Different data processing methods were recommended for two different types of remote sensing problems. When targets of interest are preselected by the user, a ratio-gating logic (RAGAL) procedure is suggested. A method is also described for finding the most efficient logic sequence for RAGAL Stored laboratory and field spectra of target materials would be used for training sets. For the type of remote sensing problem where there are no preselected targets, three types of logic were suggested—all of which entail the use of laboratory and field spectra as training sets. One is RAGAL, performed in reverse to the preselected target case. A second is unsupervised clustering in ratio space, with stored lab and field spectra used to identify the clustered targets. The third is a parameterization method whereby a linear combination of ratios is used to predict a physically meaningful index related to target composition.

ERIM

REFERENCES

1. Vincent, R. K., R. Horvath, F. Thomson, and E. Work, Remote Sensing Data-Analysis Projects Associated with the NASA Earth Resources Spectral Information System, Report No. 31650-26-T, NASA Contract NAS9-9784, Willow Run Laboratories of the Institute of Science and Technology, The University of Michigan, Ann Arbor, 1972.

2. Suits, G., R. K. Vincent, H. Horwitz, and J. Erickson, Optical Modeling of Agricultural Fields and Rough-Textured Rock and Mineral Surfaces, Report No. 31650-78-T, NASA Contract NAS9-9784, Environmental Research Institute of Michigan, Ann Arbor, November 1973.

3. Vincent, R. K., Rock-Type Discrimination from Ratio Images of Pisgah Crater, California, Report No. 31650-77-T, NASA Contract NAS9-9784, Willow Run Laboratories of the Institute of Science and Technology, The University of Michigan, Ann Arbor, 1972.

4. Lyon, R. J. P., Evaluation of IR Spectrophotometry for Compositional Analysis of Lunar and Planetary Soils: Rough and Powdered Surfaces, Final Report, Part II, NASA Contract NASr-49(04), Stanford Research Institute, Menlo Park, 1964.

5. Vincent, R. K. and G. R. Hunt, Infrared Reflectance from Mat Surfaces, Applied Optics, Vol. 7, 1968, p. 53.

6. Conel, J. E., Infrared Emissivities of Silicates: Experimental Results and a Cloudy Atmosphere Model of Spectral Emission from Condensed Particulate Mediums, J. Geophys. Res., Vol. 74, 1969, p. 1614.

7. Vincent, R. K., Emission Polarization Study on Quartz and Calcite, Applied Optics, Vol. 11, 1972, pp. 1942-45.

8. Peterson, J. T. and J. A. Weinman, J. Geophys. Res., Vol. 74, 1969, p. 6947.

9. Raman, C. V. and K. S. Viswanathan, Proc., Ind. Acad. Sci., Vol. I, 1955, p. 37; reprinted in Handbuch der Physik, Vol. XXV, Ed., S. Flügge, Chapter 8, Crystal Optics; Diffraction, p. 122.

10. Conel, J. E., Jet Propulsion Laboratory, Pasadena, Private Communication to R. K. Vincent, Willow Run Laboratories of the Institute of Science and Technology, The University of Michigan, Ann Arbor, 1970.

11. Spitzer, W. G., and D. A. Kleinman, Infrared Lattice Bands of Quartz, Phys. Rev., Vol. 121, 1961, p. 1324-35.

12. Martin Marietta Corp., Application of Remote Sensor Data to Geologic and Economic Analysis of the Bonanza Test Site, Colorado, First Year Summary Report, Denver, 1970.

13. Vincent, R. K., and F. Thomson, Spectral Compositional Imaging of Silicate Rocks, J. of Geophys. Res., Vol. 77, 1972, pp. 2465-71.

14. Vincent, R. K., F. Thomson, and K. Watson, Recognition of Exposed Quartz Sand and Sandstone by Two-Channel Infrared Imagery, J. of Geophys. Res., Vol. 77, 1972, pp. 2473-77.

15. Vincent, R. K., and F. Thomson, Rock Type Discrimination from Ratioed Infrared Scanner Images of Pisgah Crater, California, Science, Vol. 175, 1972, pp. 986-88.

16. Anding, D., R. Kauth, and R. Turner, Atmospheric Effects on Infrared Multi-spectral Sensing of Sea Temperature from Space, Report No. 2676-5-F, Willow Run Laboratories of the Institute of Science and Technology, The University of Michigan, Ann Arbor, 1970.

17. Wagner, T., R. K. Vincent, B. Drake, R. Mitchell, and P. Jackson, Tunnel-Site Selection by Remote Sensing Techniques, Report No. 10018-13-F, U.S. Bureau of Mines Contract HO210041, Willow Run Laboratories of the Institute of Science and Technology, The University of Michigan, Ann Arbor, 1972.

18. Vincent, R.K., The NASA Earth Resources Spectral Information System: A Data Compilation - Second Supplement, Report No. 31650-156-T, NASA Contract NAS9-9784, Environmental Research Institute of Michigan, Ann Arbor, 1973.

19. Vincent, R. K., T. Wagner, B. Drake, and P. Jackson, Geologic Reconnaissance and Lithologic Identification by Remote Sensing, Report No. 191700-8-F, U.S. Bureau of Mines Contract HO220064, Environmental Research Institute of Michigan, Ann Arbor, 1973.

20. Thomson, F. J., ERIM Progress Report on Use of ERTS-1 Data, Summary of Ten Tasks, Type II Progress Report, Report No. NASA-CR-133556, NTIS No. E73-10899/WR, Environmental Research Institute of Michigan, Ann Arbor, 1973.

21. Turner, R., W. Malila, and R. Nalepka, Importance of Atmospheric Scattering on Remote Sensing, or, Everything You've Always Wanted to Know About Remote Sensing but Were Afraid to Ask, Proc., 7th International Symposium on Remote Sensing of Environment, Report No. 10259-1-X, Willow Run Laboratories of the Institute of Science and Technology, The University of Michigan, Ann Arbor, 1971.

22. Vincent, R. K., An ERTS Multispectral Scanner Experiment for Mapping Iron Compounds, Proc., 8th International Symposium on Remote Sensing of Environment, Report No. 195600-1-X, Willow Run Laboratories of the Institute of Science and Technology, The University of Michigan, Ann Arbor, 1972.

23. Piech, K. R., and J. E. Walker, Interpretation of Soils, Photogram. Engin., Vol. XL, 1974, pp. 84-94.

24. Thomson, F. J., ERIM Progress Report on Use of ERTS-1 Data, Summary of Ten Tasks, Type I, Report No. 193300-24-L, NASA Contract NAS5-21783, Environmental Research Institute of Michigan, Ann Arbor, 1973.

25. Dillman, R. and R. K. Vincent, Unsupervised Mapping of Geologic Features and Soils in California, Proc. of the Ninth Symp. for Remote Sens. of Environ., Ann Arbor, Mich., 1974, (In Press).

26. Salmon, B. and R. K. Vincent, Surface Compositional Mapping in the Wind River Range and Basin, Wyoming by Multispectral Techniques Applied to ERTS-1 Data, Proceedings of the Ninth Symposium for Remote Sensing of Environment, Ann Arbor, Mich., 1974 (In Press).

27. Vincent, R. K., G. Thomas, and R. Nalepka, Signature Extension Studies, Report No. 190100-26-T, NASA Contract NAS9-9784, Environmental Research Institute of Michigan, Ann Arbor, (In Press).

28. R. K. Vincent, A Thermal Infrared Ratio Imaging Method for Mapping Compositional Variations Among Silicate Rock Types, Ph.D. Dissertation, Department of Geology and Mineralogy, The University of Michigan, Ann Arbor, 1973.

29. R. B. Travis, Classification of Rocks, Quarterly of the Colorado School of Mines, Vol. 50, No. 1, 1955, p. 12.

Appendix A

DOCUMENTATION FOR COMPUTER PROGRAM LTOTAL6

This is a documentation of LTOTAL6, implementation of which appears in Section 4. Following the discussion is a computer listing of the program as run on an IBM 360 computer.

A.1 GENERAL INDEX

Because of the variety of functions LTOTAL6 is capable of performing, this description has been subdivided to facilitate any operator's understanding of its various elements and their interaction. Cross-referencing between sections is provided. The order of presentation is as follows:

(1) General Index to·Program Segments

(2) Radiance Calculation Systems in LTOTAL6

(3) Filtration Systems in LTOTAL6

(4) Ratioing Systems in LTOTAL6

(5) Regression System in LTOTAL6

(6) Operation Procedure for LTOTAL6

(7) Output Information

Sections A.2 through A.5 present theoretical concepts and methods of manipulation for each of the individual segments of the program. Section A.6, covering operation procedure, supplies the operator with all input parameters necessary to run LTOTAL6. Section A.7 describes output parameters which may assist in the selection of proper input parameters.

A.2 RADIANCE CALCULATION SYSTEMS IN LTOTAL6

Integrated radiances in defined wavelength regions are calculated in LTOTAL6 according to the following formula:

$$\int_{\lambda_0}^{\lambda_1} L_\lambda \, d\lambda = \int_{\lambda_0}^{\lambda_1} \left\{ \left[\epsilon_\lambda \left\{ L_{bb_\lambda}(T) - L_{sky_\lambda} \right\} + L_{sky_\lambda} \right] \tau_{A_\lambda} + L_{v_\lambda} \right\} d\lambda$$

where

L_λ = total spectral radiance of wavelength λ

$\epsilon_\lambda = 1 - \rho_\lambda$ = rock emissivity

$L_{bb_\lambda}(T)$ = spectral radiance of a black body at the same temperature as the rock

L_{sky_λ} = spectral radiance from the sky incident on the diffuse rock surface

87

τ_{A_λ} = spectral atmospheric transmissivity

L_{v_λ} = spectral radiance from emission and scattering into the beam by the atmosphere in the path between rock and detector

The region of integrated radiance ($\lambda_0 - \lambda_1$) is defined by the filtration system (see Section A.3 below. The thermal state of the target is variable through a defined range and the atmospheric parameters are defined for a specific set of calculations. It is currently possible to include a dry atmosphere either 1 km or 50 km high (for general input parameters, see Section A.6, Operation Procedure).

A.3 FILTRATION SYSTEMS IN LTOTAL6

Currently there are three different filtration methods available in LTOTAL6. These are (1) SQFILT, (2) HAMFLT, (3) SPCFLT. Each will be discussed separately.

Subroutine SQFILT

This subroutine will construct square window filters over defined data intervals. Digitally, SQFILT will pass all data points between defined wavelength cutoffs; all values outside the closed interval will be set equal to zero. In this respect SQFILT acts as a bandpass filter operating in the frequency domain. By appropriate selection of cutoff points, it can act as a high pass or low pass filter, LTOTAL6 has been designed to handle a maximum of two square filter windows simultaneously.

In addition, by specifying proper intput parameters, either or both of the square window filters can be made to traverse the data-set at operator-controlled increments. By specifying initial boundary conditions for filtration, LTOTAL6 will construct a family of filter windows which cover equivalent wavelength spans but are incremented by a predetermined distance. The maximum number of filters of that type are thus constructed without running off the end of the data. Since the initial conditions of the two filter windows as well as the step increment are independent, it is possible to generate two families of filters that span differing widths and move at differing rates. Within each filter window, the total integrated radiance is calculated (see Section A.2, above). For operator limits on SQFILT procedure, see Filtration Specifications in Section A.6.

Subroutine HAMFLT

This subroutine constructs Hamming window (sine) filters over defined data intervals. Since all values outside the closed interval of the window are set to zero, there are no secondary harmonic effects to this filter construction. Digitally, HAMFLT adjusts data points within the filter interval by multiplying each point by an adjusted coefficient which depends on the sine interval 0 to π. Specifying the filter cutoff points automatically centers the $\pi/2$ filter location at

the center of the desired window. Unlike SQFILT, specification of initial window cutoff points
is not totally arbitrary since the window span must cover some even multiple of 0.05μm; this
is necessary to insure proper centering of the filter window. Similar to SQFILT, LTOTAL6
has been designed to handle a maximum of two sine filter windows simultaneously. Also, like
SQFILT, sine filter windows can be made to traverse the data-sets without exceeding the data
span. Radiances are then integrated with each of the filter windows generated. [See Radiance
Calculation Systems (Section A.2) and also Filtration Specifications in Section A.6.]

Subroutine SPCFLT

In addition to the two filtration methods previously mentioned, LTOTAL6 can be given spe-
cial filter parameters to match some given response curve. Unlike the two previous filtration
methods, SPCFLT has no capability for locomotion, but is instead fixed with respect to the data-
set. LTOTAL6 can handle a maximum of two filters of this type similtaneously. Use of SPCFLT
obviously requires special input parameters for the filter construction, but need not be at uniform
incremental spacing. SPCFLT will adjust input specifications to meet data spacing require-
ments. Once data is filtered, integrated radiances are computed within the bounds of the special
filter windows. [See Radiance Calculation Systems (Section A.2) and Filtration Specifications in
Section A.6.]

> Special Note: Mixed filtration modes have not been programmed into
> LTOTAL6 so comparison of, say, a square window and
> a sine window is impossible.

A.4 RATIOING SYSTEMS IN LTOTAL6

At present, three differant ratioing techniques have been incorporated into LTOTAL6. The
two most important techniques apply only to square-wave and sine-wave filters. Since both
HAMFLT and SQFILT have the capability of generating two families of filters, two methods of
ratioing have been programmed into LTOTAL6. In both technique 2 and 3 below, ratioing is
accomplished between filters of each family, but not within the family itself.

Technique 1: Case for SPCFLT

Technique 1 involves the input of two specified filters. SPCFLT, which does not have the
capability of motion, performs simple ratioing whereby the two input filter windows are ratioed.

Technique 2: General Case for HAMFLT or SQFILT

Technique 2 simply ratios every member of filter set 1 to every member of filter set 2.
If, for example, there are r filters in set 1 and m filters in set 2, then the maximum will be n^m
ratios. It is important to note that filters of type 1 always form the numerator while filters
of type 2 form the denominator. Once calculated, these ratios may be printed out or reserved

for a linear regression at the end. [See Output Information (Section A.7); Options and Specifications (in Section A.6); and also Regression System (Section A.5).]

Technique 3: Alternative Case for HAMFLT or SQFILT

An alternative technique for ratioing output radiances for HAMFLT or SQFILT is also provided. Unlike technique 2 which assumes an independence relationship between the two filtering families, technique 3 assumes the following dependency relationship between filter sets 1 and 2: only members of set 2 which have lower wavelength cutoff points at least as great as the lower wavelength cutoff points of the members of set 1 are permitted to be ratioed. In other words, as the first filter progresses through the data-set, fewer and fewer ratios are possible because of the dependency of the second filter set to the first. Still another difference from technique 2 is that estimation of the limited number of ratios done is more complex and depends not only on the window spans, but on initial location of each set and incrementing rates. If filter sets 1 and 2 cover the same spans, begin at the same locations, and are incremented at the same rates then the maximum number of ratios simplifies to the familiar $\binom{n}{m}$* number of ratios. This is the upper bound to the number of ratios probable. Once calculated, the ratios may be printed out or reserved for regressive fits. [See Output Information (Section. A.7); Options and Specifications (in Section A.6); and also Regression System (Section A.5, below).]

A.5 REGRESSION SYSTEM IN LTOTAL6

This particular system is of value only when the HAMFLT or SQFILT subroutines have been used with a sufficiently large data bank to make regression meaningful. If the operator specified that linear regressions are to be performed (see device code 2 specifications in Section A.6), then an equivalent data collection must be supplied with which to perform a regression (see also Regression Specifications in Section A.6). The ratios are then used as the X coordinates. A simple linear regression is then performed using each of the calculated ratios (see Ratioing Systems, Section A.4) with the specified regression parameters.

The following calculations are performed with each ratio setting:

$$B = \frac{\sum_{i=1}^{n} (x_i - \bar{x})(y_i - \bar{y})}{\sum_{i=1}^{n} (x_i - \bar{x})^2}$$

---

*$\binom{n}{m} = n(n-1)(n-2)...(n-m+1)/m!$

where B = slope of the regression line of the form $y = Bx + A$

$(x_i - x)$ = deviation of the i-th term of x from the mean of x

$(y_i - \bar{y})$ = deviation of the i-th term of y from the mean of y

$(x_i - \bar{x})^2$ = square of the x deviation from the mean of x

and

$$A = \bar{y} - B(\bar{x})$$

where A = y intercept of the regression line

$$\bar{y} = \sum_{i=1}^{n} y_i / n$$

B is as previously defined

$$\bar{x} = \sum_{i=1}^{n} x_i / n$$

In addition, the roles of y dependency are reversed and the same types of calculations then made for

$$BI = \frac{\sum_{i=1}^{n} (x_i - \bar{x})(y_i - \bar{y})}{\sum_{i=1}^{n} (y_i - \bar{y})^2}$$,

and

$$AI = \bar{x} - BI(\bar{y})$$

A, B, AI, and BI—as calculated above—are thus the linear regression coefficients.

Correlation coefficients are also calculated as

$$R = \sum_{i=1}^{n} (x_i - \bar{x})(y_i - \bar{y}) \Big/ \sum_{i=1}^{n} \left[\sqrt{(x_i - \bar{x})^2} \right]\left[\sqrt{(y_i - \bar{y})^2} \right]$$

where   R = correlation coefficient

$\sqrt{(x_i - \bar{x})^2}$ = square root of the sum of the squares of the deviation in the x-direction

$\sqrt{(y_i - \bar{y})^2}$ = square root of the sum of the squares of the deviation in the y-direction

And finally, standard errors of the regression coefficient are computed as:

$$SX = \sqrt{\frac{\sum_{i=1}^{n} \left[(y_i - \overline{y}) - R^2(y_i - \overline{y})/(A - 2) \right]}{\sum_{i=1}^{n}(x_i - \overline{x})^2}}$$

and

$$SY = \sqrt{\frac{\sum_{i=1}^{n} \left[(x_i - \overline{x}) - R^2(x_i - \overline{x})(n - 2) \right]}{\sum_{i=1}^{n}(y_i - \overline{y})^2}}$$

The number of such regressions is determined by the number of ratios originally calculated [see Ratioing Systems (Section A.4) and Output Information (Section A.7)].

A.6 OPERATION PROCEDURE FOR LTOTAL6

Program LTOTAL6, written in FORTRAN IV G language for the IBM 360-67 MTS system, requires two inputs: (1) Information which has been given input device code 2; this includes most of the operational switching codes, filter parameters, and regression information. (2) Data to be used in the calculations; given input device code 3, these data are on magnetic tape and include rock emissivity and sky parameters.

(1) Options and Specifications from Device 2.

The following is a listing of options and specifications supplied from Device 2.

Line 1: Format (2x, I4,2x,3(F6.2,2x),11(I2,1x))

(a,b,c,d,e,f,g,h,i,j,k,l,m,n,o)

Discussion of parameters:

a = altitude from which calculations are to be made. Either 1 km or 50 km if an atmosphere is included (or, without an atmosphere, can be anything).

b = Initial temperature of the sample in degrees Kelvin

c = temperature increment in degrees Kelvin. (To be used if the radiance through a range of temperatures is desired. Setting c = 0.0 suppresses looping by temperature.)

d = final temperature in degrees Kelvin of the sample if incrementing by temperature is desired. Must be a multiple of c from b, the initial temperature. Setting final temperature = b also suppresses the temperature loop. Note: If looping by temperature is desired, ratioing and regression cannot be performed.

e = switch to indicate whether atmospheric parameters are to be included. Set to 1 for an atmosphere, 0 for no atmosphere.

f = switch to indicate number of filters to be included. Setting this equal to 0 ends the program since no calculations can be made.

g = switch to indicate which ratioing technique is to be used: 0 results in technique 2; 1 results in technique 3. Important only SQFILT and HAMFLT usage.

h = switch to indicate which filter type is to be used: -1 = special filters, 0 = square filters, 1 = sine filters.

i = this and the succeeding statement determine the initial and final data sets to be used. This is possible since all data-sets on the tape have been given sequential block identification numbers. Parameter i is the initial data-set number.

j = switch indicating sky condition. 0 = wet sky (currently not available), 1 = dry sky. Notice that since "e" determined whether or not there was to be an atmosphere, if e = 0 then the setting of k is irrelevant.

ℓ = switch to indicate whether any numbered data-sets between the beginning and final sets are to be omitted: 0 = no omissions; 1 indicates that omissions will be specified.

m = switch to indicate that regression using all data-sets is to be performed: 0 = no, 1 = yes. If regression is to take place, parameters will be specified.

n = as a secondary switch to m, this controls the type of printout: -1 = all ratioed bands and corresponding ratios as well as regression data will be printed out.

o = one complete set of filter ratios will be printed out with the regression data.

1 = only regression data is printed.

O = switch to suppress printing of the filter channels and radiances. 0 = no suppression, 1 = print suppressed.

Line 2. Applies only if ℓ of line 1 equals 1. Format is (5x,I2,18(2x,I2)). This line determines which data-sets are not to be included (maximum is 20). The first integer field indicates the total number of data-sets to be omitted; the remaining integer fields are the indicator numbers of each data-set.

Filter Specifications

Line 3. If h = 0 or 1, format is (6(5x,F5.2)).
This card gives initial filter cutoff points. Parameters must be in multiples of 0.05 for h = 0, and must be even multiples of 0.05 for h = 1. These parameters are read in as follows: lower wavelength cutoff f_1, upper wavelength cutoff f_1, filter increment f_1, lower wavelength cutoff f_2, upper wavelength cutoff f_2, filter increment f_2. If either of the filter increments is set as 0.0, then that filter will remain fixed in the data framework at the initial specifications. Data range 8.00 to 14.00 μm.

Line 4. If h = -1, format is (I2,5(2x,F5.2,2x,F5.3)).

Specifying h of 1 equal to -1 requires that input parameters be specified for special filter construction. Consisting of x and y coordinates for specific points, these need not be at any particular spacing but must be defined by coordinate pairs at each location. A maximum of 50 input pairs is possible for each filter. The first integer field specifies the total number of coordinate pairs to be read. The remainder of the line is reserved for the actual coordinate pairs.

Regression Specifications

Line 4. Applies only if m of 1 equals 1. Format is (5A4,10x,I3/(8(5x,F5.2)).

This first 20 spaces are to identify the regression data. The title is then followed by an integer field to indicate the total number of input points; this must match the total number of data-sets which will be used in the initial calculations. This is the last input parameter which must be read from input device code 2.

(2) Data Input from Device 3.

Data input from Device 3 is on magnetic tape and includes rock emission data and dry sky parameters for 1 km and 50 km altitudes. To access this tape (which is kept at the computing center), it must first be mounted. This is done by the following MTS commands:

$RUN *MOUNT PAR=C2541 on 9TP PNAME=*M*, MODE= 800, VOL=MARTIN,'ODDJOB'
$ENDFILE.

The name of the file for pseudo Device 3 is thus *M*. T run LTOTAL6, the command is then:

$RUN LTOT 2=*SOURCE* 3=*M* 5=SINK*

Of course, if pseudo Device 2 is a file, the file name is specified instead.

A.7 OUTPUT INFORMATION

Several types of output information are possible from LTOTAL6. These have been partially described in Section A.6 on Operation Procedure. The purpose of this section is to help clarify which output information is desired.

General Block

For each data-set, a general block is written out. This includes identification code, zenith angle, altitude, atmospheric condition, and target temperature.

Specifying O = 1 (see Options and Specifications from Device 2, in Section A.6) results in the printing of each filter band and integrated radiance included for both filter families.

Specifying n = -1 or 0 results in the printing of the filter bands ratioed and the ratio of their integrated radiances. Note that the filter 2 family is always the denominator of the ratios.

Specifying m = 1 results in the printing of all regression calculations for each of the ratios computed.

IBM 360 COMPUTER LISTING OF LTOTAL6

```
C       PROGRAM LTOTAL6 IS THE SIXTH GENERATION OF A PROGRAM TO COMPUTE
C       THE IR RADIANCE IN WATTS/CM**2/STERRADIAN. IT COMPUTES RADIANCE
C       FROM TWO ALTITUDES,1 KM AND 50 KM, THROUGH A RANGE OF TARGET TEMP-
C       ERATURES,AND WITHIN A MAXIMUM OF 240 FILTER WINDOWS.IT WILL THEN
C       RATIO THE COMPUTED RADIANCES OF EVERY COMBINATIONAL PAIR OF WIN-
C       DOWS.
C       INPUT PARAMETERS ARE TAKEN FROM TAPE UNIT 2 AND INCLUDE
C       ALT = ALTITUDE OF RUN (I3) 1 OR 50 KILOMETERS
C       TEMP = BEGINNING TEMPERATURE ASSUMED FOR IR TARGET
C       TINC = TEMPERATURE INCREMENT
C       TEND = FINAL TEMPERATURE ASSUMED FOR IR TARGET
C       ATMOS = IF ATMOSPHERE USED ATMOS=1,IF NO ATMOSPHERE ATMOS=0
C       NF =NUMBER OF INITIAL FILTER GENERATORS
C       ISW = SWITCH ALLOWING RATIOING OF SECONDARY FILTERS HAVING CUTLW
C       ABOVE CUTLW OF PRIMARY FILTERS ONLY
C       SPECIFYING NF = 0 WILL BYPASS ANY FILTER WINDOW CONSTRUCTION
C       SPECIFYING TINC = 0 WILL PERMIT SAMPLING AT A SINGLE TEMPERATURE
C       SPECIFYING FILTINC(J) = 0 WILL CREATE ONE STATIONARY SQUARE FILTER
C       IF FTYPE = -1  NF SPECIAL FILTERS ARE READ IN FROM UNIT 2
C       IF FTYPE =  0  NF SQUARE FILTER PARAMETERS ARE READ IN FROM UNIT 2
C       IF FTYPE =  1  NF HAMMING WINDOW  PARAMETERS ARE READ IN FROM UN 2
C       NDATL =  FIRST DATA SET TO BE USED
C       NDATH =  LAST DATA SET TO BE USED
C       IF SC=0 SKY CONDITION = WET
C       IF SC=1 SKY CONDITION = DRY
C       IF DATSKIP = 1 DATA NUMBERS TO BE SKIPPED ARE READ IN FROM UNIT 2
C       IF RGSW1 = 1 LINEAR REGRESSION OF EACH RATIO FILTER PAIR WILL BE
C       PERFORMED USING THE ENTIRE DATA CATALOG READ IN.
C       IF RGSW2 = -1, ALL OF THE RATIOED BANDS AND CORRESPONDING RATIOS
C       AS WELL AS REGRESSION DATA WILL BE PRINTED OUT.
C       IF RGSW2 = 0, ONE COMPLETE SET OF FILTER RATIOS FOR THE ENTIRE DATA
C       SET AND ALL OF THE REGRESSION DATA IS PRINTED OUT.
C       IF RGSW2 = 1, NONE OF THE RATIOED BANDS OR RATIOS BUT ALL OF THE
C       REGRESSION DATA IS PRINTED OUT.
C       IF MSKIP=1 THE FILTER CHANNELS AND INTEGRATED RADIANCES ARE NOT
C       PRINTED OUT.
C       INPUT DATA ARE TAKEN FROM TAPE UNIT 3 AND MUST HAVE THE FOLLOWING
C       SPECIFICATIONS.
C       (1) DATA RANGE 8.00 TO 14.00 MICRONS
C       (2) DATA INCREMENTED BY 0.05 MICRONS I.E. UNIFORM DATA SPACING.
C       THIS CAN BE ACCOMPLISHED BY PASSING DATA FROM PROGRAM INTERP THRU
C       PROGRAM FIX.
        DIMENSION X(121),Y(121),LSKY(121),TA(121),LPATH(121),LTOT(121)
        DIMENSION CUTUW(2,51),CUTLW(2,51),FLTINC(2) ,LIM(2),RB(51,51),LC(2
       1,51),WIND(2),NDAT(20),PART(121),NN(2),FX(2,50),FY(2,50),LT(30,2,51
       2)
        DIMENSION   RATIO(30),REDAT(30),NDATA1(30)
        REAL   LTOT,LBB,LSKY,LPATH,LC,LT
        INTEGER ATMOS,FTYPE,ALT,SC,DATSKP ,RGSW1,RGSW2
        NUMB=0
C
C
C       ************************************************************************
      5 READ (2,10)ALT,TEMP,TINC,TEND,ATMOS,NF,ISW,FTYPE,NDATL,NDATH,SC,
       1DATSKP,RGSW1,RGSW2,MSKP
     10 FORMAT (2X,I4,2X,3(F6.2,2X),11(I2,1X))
        T1=TEMP
        T2=TINC
        T3=TEND
        IF (DATSKP.EQ.0) GO TO 14
```

95

```
C    READING DATA NUMBERS TO BE SKIPPED
C    ****************************************************************
  11 READ(2,12)(NSKIP,(NDAT(I),I=1,NSKIP))
  12 FORMAT (5X,I2,18(2X,I2))
  14 IF (FTYPE.EQ.-1) GO TO 35
     IF (NF) 20,100,20
C    ****************************************************************
  35 DO 37 J=1,NF
C    ****************************************************************
     READ (2,36) (M,(FX(J,I),FY(J,I)),I=1,M)
  36 FORMAT (I2,5(2X,F5.2,2X,F5.3))
     NN(J)=M
  37 CONTINUE
     LIM(1)=1
     LIM(2)=1
     GO TO 100
C    ****************************************************************
  20 READ (2,30)  (CUTLW(J,1),CUTUW(J,1),FLTINC(J),J=1,NF)
  30 FORMAT  (6(5X,F5.2))
  40 DO 90 J=1,NF
     NFILT=0
     WIND(J)=CUTUW(J,1)-CUTLW(J,1)
     DO 70 K=2,60
     NFILT=NFILT+1
     IF (FLTINC(J) .EQ.0.0) GO TO 80
     CUTUW(J,K)=CUTUW(J,K-1)+FLTINC(J)
     CUTLW(J,K)=CUTLW(J,K-1)+FLTINC(J)
     IF (CUTUW(J,K).GT.14.0) GO TO 80
  70 CONTINUE
  80 LIM(J)=NFILT
  90 CONTINUE
 100 CONTINUE
     MAX=LIM(1)
     MAX2=LIM(2)
     IF (RGSW1.EQ.0) GO TO 105
C    ****************************************************************
 101 READ(2,102)TITLE1,TITLE2,TITLE3,TITLE4,TITLE5,NNN,(REDAT(N),N=1,NN
    1N)
 102 FORMAT (5A4,10X,I3/(8(5X,F5.2)))
C    ****************************************************************
 105 READ (3,110) NPTS,ID1,ID2,ID3,NDATA
 110 FORMAT (I3,2X,A4,A2,A3,2X,I3)
     IF (NDATA.LT.NDATL)GO TO 111
     TEMP=T1
     TINC=T2
     TEND=T3
C    NDATA = DATA SET NUMBER ON TAPE
     DO 113   N=1,NSKIP
     IF (NDATA.EQ.NDAT(N)) GO TO 111
     GO TO 113
 111 CALL SKIP (0,121,3,400,400,400)
C    NOT... THE PREVIOUS COMMAND IS TO AN MTS SUBROUTINE FOR TAPES
     GO TO 105
 113 CONTINUE
     NUMB=NUMB+1
     NDATA1(NUMB)=NDATA
C    ----------------------------------------------------------------
     WRITE (5,112) NDATA,ID1,ID2,ID3,ALT
 112 FORMAT(///I3,5X,8HSAMPLE   ,A4,A2,A3,5X,39HZENITH ANGLE = 0.0,
    1SLANT RADIUS = ,I4,5H  KM.)
```

```
      IF (ATMOS.GT.0) GO TO 115
C     ------------------------------------------------------------------
      WRITE (5,114)
  114 FORMAT (13HNO ATMOSPHERE)
      GO TO 120
  115 IF (SC.EQ.0) GO TO 118
C  °  ------------------------------------------------------------------
      WRITE (5,117)
  117 FORMAT (14HDRY ATMOSPHERE)
      GO TO 150
C     ------------------------------------------------------------------
  118 WRITE (5,119)
  119 FORMAT (14HWET ATMOSPHERE)
      GO TO 150
  120 DO 140 I=1,NPTS
C     ****************************************************************
      READ(3,130) X(I),Y(I)
  130 FORMAT (2X,F6.3,2X,F6.4)
      LSKY(I)=0.0
      LPATH(I)=0.0
      TA(I)=1.0
  140 CONTINUE
      GO TO 200
  150 IF (ALT.GT.1) GO TO 180
C     ****************************************************************
  160 READ (3,170)(X(I),Y(I),LSKY(I),TA(I),LPATH(I),I=1,NPTS)
  170 FORMAT (2X,F6.3,2X,F6.4,2X,E10.3,2X,F7.5,2X,E10.3)
      GO TO 200
C     ****************************************************************
  180 READ (3,190)(X(I),Y(I),LSKY(I),TA(I),LPATH(I),I=1,NPTS)
  190 FORMAT (2X,F6.3,2X,F6.4,2X,E10.3,23X,F7.5,2X,E10.3)
C
C     SEGMENT 200 THROUGH 239 COMPUTES INTEGRATED RADIANCE FOR EACH
C     FILTER CHANNEL.
C
  200 DO 210 L=1,NPTS
C     COMPUTING BLACK BODY RADIANCE AT TEMPERATURE TEMP
      LBB=1.19E7/((X(L)**5)*((EXP(1.4399E4/(X(L)*TEMP)))-1.0))
      PART(L)=TA(L)*(Y(L)*LBB+(1.0-Y(L))*LSKY(L))+LPATH(L)
  210 CONTINUE
C     ------------------------------------------------------------------
      WRITE (5,201)TEMP
  201 FORMAT (21HTARGET TEMPERATURE = ,F6.2,10H DEGREES K)
      TH=X(2)-X(1)
      N=NPTS-1
      IF (NF.EQ.0) GO TO 400
      MM=MAX
      DO 240 J=1,NF
      DO 230 K=1,MM
      TOTAR=0.0
      IF (FTYPE)211,212,213
  211 CALL SPCFLT (  NN,FX,FY,PART,LTOT,X)
      GO TO 215
  212 CALL SQFILT (NPTS,CUTLW(J,K),CUTUW(J,K),PART,LTOT,X)
      GO TO 215
  213 CALL HAMFLT (NPTS,CUTLW(J,K),CUTUW(J,K),PART,LTOT,X)
  215 DO 220 I=1,N
      TM=(LTOT(I)+LTOT(I+1))/2.0
      AREA=TM*TH
      TOTAR=TOTAR+AREA
```

```
220 CONTINUE
    LC(J,K)=TOTAR
    LT(NUMB,J,K )=LC(J,K)
230 CONTINUE
    MM=MAX2
240 CONTINUE
239 IF (FTYPE) 245,241,241
241 IF (MSKP.EQ.1)  GO TO 249
    WRITE (5,242)
242 FORMAT (2X,4(11HFILTER BAND,4X,8HRADIANCE,6X))
    WRITE (5,243)
243 FORMAT (2X,4(10HIN MICRONS,4X,11HMW/CM**2*SR,4X))
C   WRITING OUT FILTER LIMITS AND INTEGRATED RADIANCE WITHIN FILTER
C   BANDS
    WRITE (5,244)(CUTLW(1,K),CUTUW(1,K),LC(1,K),K=1,MAX)
    WRITE (5,244)(CUTLW(2,K),CUTUW(2,K),LC(2,K),K=1,MAX2)
244 FORMAT (4(2X,F5.2,1H-,F5.2,4X,E9.4,4X))
249 IF (RGSW2)  252,325,325
C   -------------------------------------------------------------
245 WRITE (5,246)
246 FORMAT (14HFILTERBAND (1),5X,8HRADIANCE,5X,14HFILTERBAND (2),5X,8H
   1RADIANCE)
C   -------------------------------------------------------------
    WRITE (5,247)
247 FORMAT (19X,11HMW/CM**2*SR,21X,11HMW/CM**2*SR)
C   -------------------------------------------------------------
    WRITE (5,248) LC(1,1),LC(2,1)
248 FORMAT(19X,E9.4,23X,E9.4)
    GO TO 250
252 IF(CUTLW(1,1).EQ.CUTLW(2,1).AND.CUTUW(1,1).EQ.CUTUW(2,1).AND.FLTIN
   1C(1).EQ.FLTINC(2))GO TO 290
    IF (WIND(1).EQ.WIND(2).AND.FLTINC(1).EQ.FLTINC(2)) GO TO 290
    IF (ISW.EQ.1) GO TO 290
250 DO 270  K=1,MAX
    DO 260  N=1,MAX2
    RB(K,N)=LC(1,K)/LC(2,N)
260 CONTINUE
270 CONTINUE
    GO TO 321
290 DO 310  K=1,MAX
    DO 305  N=1,MAX2
    IF (CUTLW(2,N).LT.CUTLW(1,K)) GO TO 305
    RB(K,N)=LC(1,K)/LC(2,N)
305 CONTINUE
310 CONTINUE
C   WRITING OUT RATIOED FILTER CHANNELS
C   -------------------------------------------------------------
321 WRITE (5,323)
    WRITE(5,322)(( CUTLW(1,K),CUTUW(1,K),CUTLW(2,N),CUTUW(2,N),RB(K,N)
   1,N=1,MAX2),K=1,MAX)
322 FORMAT (3(2X,F5.2,1H-,F5.2,1H/,F5.2,1H-,F5.2,5X,F6.4,3X))
323 FORMAT (////2X,3(13HBANDS RATIOED,15X,5HRATIO,6X)//)
325 TEMP=TEMP+TINC
C   RECYCLING BY TEMPERATURE
    IF (TEMP.LT.TEND.OR.TINC.NE.0.0) GO TO 200
    NDATA=NDATA+1
    IF (NDATA.LE.NDATH) GO TO 105
326  IF (RGSW1.EQ.0) GO TO 400
C   -------------------------------------------------------------
329 WRITE (5,330) NUMB,TITLE1,TITLE2,TITLE3,TITLE4,TITLE5
```

98

C·2

```
  330 FORMAT  (//47HRESULTS OF LINEAR REGRESSION CALCULATIONS USING,1X,I
     13,1X,40HDATA SETS.  REGRESSION OF BAND RATIOS VS,3X,5(A4),///)
C     ----------------------------------------------------------------
      WRITE (5,331)
  331 FORMAT(5X,13HBANDS RATIOED,13X,23HREGRESSION COEFFICIENTS,6X,13HCO
     1RREL COEFF.,5X,32HSTANDARD REGRESSION COEFF. ERROR,/29X,28HRATIO I
     2NDEP  *   RATIO DEPEND 27X,6HX-AXIS,8X,6HY-AXIS/,30X,1HA,7X,1HB,7X,
     31HA,7X,1HB,57X,4HERR.,//)
  340 IF (ISW.EQ.0) GO TO 360
      DO 355 K=1,MAX
      MARK=0
      DO 351 N=1,MAX2
      MARK=MARK+1
      IF (CUTLW(2,N).GE.CUTLW(1,K)) GO TO 350
  351 CONTINUE
  350 DO 356  N=MARK,MAX2
  352 DO 353 NI=1,NUMB
      RATIO(NI)=LT(NI,1,K)/LT(NI,2  ,N)
  353 CONTINUE
      CALL REGRES (NUMB,RATIO,REDAT,A,B,AI,BI,SX,SY,R,IER)
C     ----------------------------------------------------------------
      WRITE (5,354) CUTLW(1,K ),CUTUW(1,K ),CUTLW(2,N ),CUTUW(2,N ),A,B,
     1AI,BI,R,SX,SY,IER
  354 FORMAT (2X,F5.2,1H-,F5.2,1H/,F5.2,1H-,F5.2,1X,2(E9.3)    ,2(F7.3,1X
     1)),3X,F7.4,12X,E10.5,4X,E10.5,5X,I2)
  356 CONTINUE
  355 CONTINUE
      GO TO 400
  360 DO 366  J=1,NF
      DO 365 K1=1,MAX
      DO 364 K2=1,MAX2
      DO 361 NI=1,NUMB
      RATIO(NI)=LT(NI,J,K1)/LT(NI,J+1,K2)
  361 CONTINUE
      CALL REGRES (NUMB,RATIO,REDAT,A,B,AI,BI,SX,SY,R,IER)
C     ----------------------------------------------------------------
      WRITE (5,354) CUTLW(J,K),CUTUW(J,K),CUTLW(J+1,N),CUTUW(J+1,N),A,B,
     1AI,BI,R,SX,SY,IER
  364 CONTINUE
  365 CONTINUE
  366 CONTINUE
C     ----------------------------------------------------------------
  400 WRITE (5,401)
  401 FORMAT (14HALIA JACTA EST)
      END
      SUBROUTINE  REGRES (N,X,Y,A,B,AI,BI,SX,SY,R,IER)
C     SUBROUTINE REGRES IS DESIGNED TO COMPUTE THE LINEAR REGRESSION
C     COEFFICIENTS FOR A GIVEN SET OF DATA. IT ALSO RETURNS THE STANDARD
C     ERRORS OF REGRESSION COEFFICIENTS.
      DIMENSION  X(30),Y(30), XX(30),YY(30)
      SUMX=0.0
      SUMY=0.0
      IER=0
      NN=0
      TII=0.0
      TJJ=0.0
      TIJ=0.0
C     SUMMING ALL X VALUES AND ALL Y VALUES.
      DO 10 I=1,N
      SUMX= SUMX + X(I)
```

```
      SUMY= SUMY + Y(I)
      NN=NN+1
   10 CONTINUE
      FN=NN
C     COMPUTING MEANS OF X AND Y DATA
      XBAR=SUMX/FN
      YBAR=SUMY/FN
      DO 20 J=1,N
C     COMPUTING DEVIATIONS OF EACH X AND Y VALUE FROM CALCULATED MEAN
      XX(J)=X(J)-XBAR
      YY(J)=Y(J)-YBAR
C     TII = SUM OF THE SQUARE OF THE DEVIATIONS FROM X
      TII=TII+XX(J)**2
C     TJJ = SUM OF THE SQUARES OF THE DEVIATIONS FROM Y
      TJJ=TJJ+YY(J)**2
C     TIJ = SUM OF THE CROSS PRODUCT OF SQUARE OF X AND Y VALUES
      TIJ=TIJ+XX(J)*YY(J)
   20 CONTINUE
      IF (TII.EQ.0.0) GO TO 22
   21 IF (TJJ.EQ.0.0) GO TO 23
      GO TO 24
   22 TII=1.0
      IER=1
      GO TO 21
   23 TJJ=1.0
      IER=IER+2
C     COMPUTING LINEAR REGRESSION COEFFICIENTS
   24 B=TIJ/TII
      A=YBAR-B*XBAR
      BI=TIJ/TJJ
      AI=XBAR-BI*YBAR
C     COMPUTE CORRELATION COEFFICIENTS
      R=TIJ/(SQRT(TII)*SQRT(TJJ))
      RR=R**2
C     COMPUTE STANDARD ERRORS OF REGRESSION COEFFICIENTS.
      SX=SQRT((TJJ-(TJJ*RR)/(FN-2))/TII)
      SY=SQRT((TII-(TII*RR)/(FN-2))/TJJ)
      RETURN
      END
      SUBROUTINE SQFILT (NPTS,CUTLW,CUTUW,Y,YY,X)
C     SQFILT CONSTRUCTS A FILTER WINDOW WITH SPECIFIED WAVELENGTH CUTOFF
C     POINTS
C     NPTS=NUMBER OF POINTS IN FILTER
C     CUTLW=LOWER WAVELENGTH CUTOFF
C     CUTUW=UPPER WAVELENGTH CUTOFF
C     X=INPUT X ARRAY
C     Y=INPUT Y ARRAY
C     YY=FILTERED OUTPUT ARRAY
C     CUTLW AND CUTUW MUST BE MULTIPLES OF 0.05 MICRONS
      DIMENSION  YY(121),X(121),Y(121)
      DO 25 I=1,NPTS
      IF (X(I).GE.CUTLW) GO TO 30
   20 YY(I)=0.0
   25 CONTINUE
   30 DO 40 J=I,NPTS
      IF (X(J).GT.CUTUW) GO TO 45
   35 YY(J)=Y(J)
   40 CONTINUE
   45 DO 50 K=J,NPTS
      YY(K)=0.0
```

100

```
  50 CONTINUE
     RETURN
     END
     SUBROUTINE SPCFLT   (N,FX,FY,Y,YY,X)
     DIMENSION FFX(121),FFY(121),YY(121),FFFY(121),X(121)
     IF(FX(1).EQ.X(1).AND.FX(N).EQ.X(121)) GO TO 80
  10 IF (FX(1).LE.X(1))   GO TO 40
  20 XA=FX(2)-FX(1)
     YA=FY(2)-FY(1)
     SLOPE=YA/XA
     B=FY(1)-SLOPE*FX(1)
     FFX(1)=8.00
     FFY(1)=SLOPE*8.00+B
     DO 30 J=1,N
     FFX(J+1)=FX(J)
     FFY(J+1)=FY(J)
     MM=J+1
  30 CONTINUE
  40 DO 50 J=1,N
     FFX(J)=FX(J)
     FFY(J)=FY(J)
     GO TO 60
  50 CONTINUE
     MM=J
C    MM = TOTAL NUMBER OF FILTER POINTS
C    CHECK TO SEE IF EXTRAPOLATION OF UPPER BOUND IS NECESSARY.
  60 IF (FFX(MM).GE.X(121))   GO TO 80
  70 XA=FFX(MM)-FFX(MM-1)
C    EXTRAPOLATING ENDPOINT AT X = 14.00
     YA=FFY(MM)-FFY(MM-1)
     SLOPE=YA/XA
     B=FFY(MM)-SLOPE*FFX(MM)
     FFX(MM+1)=X(121)
     FFY(MM+1)=SLOPE*X(121)+B
     MM=MM+1
     L=1
  80 DO 130 J=1,121
     DO 120 K=L,N
C    INTERPOLATING FILTER DATA POINTS TO MATCH DATA SPACING
     IF (FFX(K).LT.X(J)) GO TO 120
  90 IF (FFX(K).EQ.X(J)) GO TO 100
     XINT=FFX(K)-FFX(K-1)
     YINT=FFY(K)-FFY(K-1)
     XDIST=X(J)-FFX(K-1)
     YCOR=XDIST*YINT/XINT
     FFFY(J)=FFY(K-1)+YCOR
     L=K
     GO TO 130
 100 FFFY(J)=FFY(K)
     L=K
     GO TO 130
 120 CONTINUE
 130 CONTINUE
     DO 140 M=1,121
     YY(M)=Y(M)*FFFY(M)
C    CONVOLVING THE DATA WITH THE FILTER
 140 CONTINUE
     RETURN
     END
     SUBROUTINE HAMFLT (N,CL,CU,Y,YY,X)
```

```
      DIMENSION   FILT(121),YY(121),X(121),Y(121)
C     FILT = GENERATED FILTER WINDOW
      NPS=0
      XINC=0.0
      NN=0
      FM=(CU-CL)/2
      MF=FM
      FR=MF
      IF (FR.LT.FM.OR.FR.GT.FM) GO TO 45
   10 DO 20 I=1,N
      IF (X(I).GE.CL) GO TO 25
   15 FILT(I)=0.0
   20 CONTINUE
   25 CENT=CL+FM
      XDIST=CENT-CL
      INCR=XDIST/0.05
      FCENT=CENT-8.0000
      M=(FCENT/0.05)+1
      FILT(M)=1.0
      NPS=M
      NN=M
      DO 30 I=1,INCR
      XINC=XINC+0.05
      YF=SIN(1.57079632-(1.57079632*XINC/XDIST))
      NPS=NPS+1
      NN=NN-1
      FILT(NPS)=YF
      FILT(NN)=YF
   30 CONTINUE
      NPS=NPS+1
      DO 35 I=NPS,N
      FILT(I)=0.0
   35 CONTINUE
      DO 40  I=1,N
      YY(I)=Y(I)*FILT(I)
   40 CONTINUE
   45 CONTINUE
      RETURN
      END
```

459 LINES PRINTED

Appendix B

DOCUMENTATION FOR COMPUTER PROGRAM ARAGAL

ARAGAL uses five tape drives for input and output. Their use is as follows:

UNIT	FUNCTION	FORMAT	
2	input	11F6.3	These are the gate limits for the ratios. 1 card per ratio. The first value on each card should be zero and the last should be several times the highest expected ratio (we usually use 90.0).
3	input	(binary)	Data tape in ERSIS format containing the curves on which the program is to be run. All curves should have values from 0.4 to 2.5 microns, occurring every 0.21 μm.
5	input	1X,I3	Number of curves on the ERSIS tape which are not to be included for various reasons; maximum is 260.
		8(1X,A6,A3)	Curve numbers of the curves on the ERSIS tape that are to be deleted. Eight per card, for as many cards as necessary (the last card need not be completely filled).
4	output		This is for printed output. The user gets back his input gate limits (from unit 2). He also gets the curve number, title, eleven-digit number, single-channel values, and ratio values for each curve desired. At the end of list of curves is a histogram showing the distribution of digits for each ratio.
5	output		Data tape containing the eleven-digit number, curve number, ratio values, and title for all the desired curves (used as input for KOLEKT).

ARAGAL also has output on unit 9, consisting of the word END. This lets the user know that his job ran successfully when he is running it himself; it may be deleted from the deck without harm. The program writes an end-of-file on both output tapes before unloading them.

CDC 1604 COMPUTER LISTING OF ARAGAL

```
      PRCGRAM ARAGAL
C     ARAGA IS CESIGNEE TO COMPUTE AVERAGE RADIANCE IN NIME AIRCRAFT
C     CHANNELS WHICH ARE SINE FILTEREE. IT THEN RATIOS SEVERAL OF THE
C     CHANNELS  ANC COMPRESSES THE RATIO INFORMATION INTO AN 11 DIGIT NUMBER
      DIMENSICN IDA(26C),ICB(260),PCCNT(11,10)
      DIMENSICN  YSUM(9),RAT(15),I(11),EL(130)
      DIMENSICN PARID(101),PAR(101),SBJCD(17),TITLE(41),CMTS(81),X(251),
     1Y(251),X1(4,250),Y1(4,250),EKAS(20),C(20)
      CCMMCN NWCRDS,MAJOR,IC1,ID2,C15C,NCURV,YCODE1,REVI,RDAY,RMO,RYR,
     1RCM1,RCM2,RCM3,NPAR,PARID,PAR,NSBJCD,SBJCD,NTITLE,TITLE,NCMT,CMTS,
     2CURVN,YCODE2,XCODE,XMIN,XMAX,NPTS,LAMBDA,THETI,PHII,THETR,PHIR,X,
     3Y,X1,Y1,CPTS,IN,INPUT,CUT,OUTPUT, NMAJ, NRE3
      INTEGER      C15C,YCCCE1,REVI,RDAY,RMO,RYR,RCM1,RCM2,RCM3,PARID,
     1PAR,SCJCD,TITLE,CMTS,CURVN,YCODE2,XCODE,CPTS,OUTPUT,PUNCH,SCRACH
      INTEGER ECF,FCE
      REAC (2,200) (EL(I),I=1,121)
  200 FCRMAT (11(11F6.3,/))
      NENC=0
      ASSIGN 1000 TC FCE
      DC 220 I=1,11
      DC 210 J=1,10
      PCCNT(I,J)=0
  210 CCNTINUE
  220 CCNTINUE
      WRITE (4,1)
    1 FCRMAT (12(1CH*AIRCRAFT*))
      WRITE (4,2)
    2 FCRMAT (42HAIRCRAFT 50 PERCENT SINE LIMITS IN MICRONS)
      WRITE (4,3)
    3 FCRMAT (/5X,1CHR1=.43-.47,/5X,1CHR2=.49-.51,/5X,1CHR3=.53-.56,/5X,
     11CHR4=.59-.63,/5X,1CHR5=.63-.67,/5X,1CHR6=.70-.90,/5X,1CHR7=1.0-1.
     24,/5X,1CHR8=1.5-1.8,/5X,1CHR9=2.0-2.5,///)
      WRITE (4,45)
   45 FCRMAT (22HGATE LIMITS FCR RATIOS)
      WRITE (4,46)
   46 FCRMAT (/22X,1H0,9X,1H1,9X,1H2,9X,1H3,9X,1H4,9X,1H5,9X,1H6,9X,1H7,
     19X,1H8,9X,1H9)
      WRITE (4,47) ((EL(J+K),K=1,11),J=0,110,11)
   47 FCRMAT (/5X,5HR9/R811(4X,F6.3),/5X,5HR9/R511(4X,F6.3),/5X,5HR8/R51
     11(4X,F6.3),/5X,5HR7/R611(4X,F6.3),/5X,5HR7/R511(4X,F6.3),/5X,5HR6/
     2R511(4X,F6.3),/5X,5HR6/R211(4X,F6.3),/5X,5HR6/R111(4X,F6.3),/5X,5H
     3R5/R411(4X,F6.3),/5X,5HR5/R311(4X,F6.3),/5X,5HR2/R111(4X,F6.3))
      CALL SETECF (FOE)
      READ (5,150) NUTS,(IDA(I),ICB(I),I=1,NUTS)
  150 FCRMAT (1X,I3,/(   8(1X,A6,A3)))
    5 CALL READ (3,EOF,MAJSW)
    6 IF (MAJSW.EQ.1) 7,5
    7 CALL READ (3,ECF,MAJSW)
      DC 100  I=1,NUTS
      IF (IC1.EC.IDA(I).ANC.ID2.EC.IDB(I)) 5,100
  100 CCNTINUE
      DC 155 I=1,9
      YSUM(I)=0.0
  155 CCNTINUE
C     CCMPUTING PERCENTAGE REFLECTANCE IN 9 AIRCRAFT CHANNELS
      YSUM(1)=(((Y(2)+Y(4))/2)+Y(3))/3.0
      YSUM(2)=(((Y(5)+Y(7))/2)+Y(6))/3.0
      YSUM(3)=(((Y(7)+Y(9))/2)+Y(8))/3.0
      YSUM(4)=(((Y(10)+Y(12))/2)+Y(11))/3.0
      YSUM(5)=(((Y(12)+Y(14))/2)+Y(13))/3.0
```

```
      FX=3.14159264/42.0
      AN=14.0
      M=14
      DO 50 I=54,60
      YSUM(8)=YSUM(8)+(Y(I)+Y(I+M))*COS(AN*FX)
      YSUM(9)=YSUM(9)+(Y(I+33)+Y(I+33+M))*COS(AN*FX)
      AN=AN-2.
      M=M-2
   50 CONTINUE
      YSUM(8)=(YSUM(8)+Y(61))/15.0
      YSUM(9)=(YSUM(9)+Y(94))/15.0
      FX=3.14159264/24.0
      AN=8.0
      M=9
      J=30
      N=19
      DO 51 I=16,20
      YSUM(6)=YSUM(6)+(Y(I)+Y(I+M))*COS(AN*FX)
      YSUM(7)=YSUM(7)+(Y(J)+Y(J+1)+Y(J+N)+Y(J+N-1))*COS(AN*FX)
      M=M-2
      AN=AN-2.
      J=J+2
      N=N-4
   51 CONTINUE
      YSUM(6)=YSUM(6)/10.0
      YSUM(7)=YSUM(7)/20.0
C     COMPUTING CHANNEL RATIOS
      RAT(1)=YSUM(9)/YSUM(8)
      RAT(2)=YSUM(9)/YSUM(5)
      RAT(3)=YSUM(8)/YSUM(5)
      RAT(4)=YSUM(7)/YSUM(6)
      RAT(5)=YSUM(7)/YSUM(5)
      RAT(6)=YSUM(6)/YSUM(5)
      RAT(7)=YSUM(6)/YSUM(2)
      RAT(8)=YSUM(6)/YSUM(1)
      RAT(9)=YSUM(5)/YSUM(4)
      RAT(10)=YSUM(5)/YSUM(3)
      RAT(11)=YSUM(2)/YSUM(1)
      N=1
      DO 40 I=1,11
      M=-1
      NN=N+9
      DO 35 J=N,NN
      M=M+1
      IF (RAT(I).GT.EL(J).AND.RAT(I).LE.EL(J+1)) 34,35
   34 I(I)=M
      GO TO 36
   35 CONTINUE
   36 N=N+11
   40 CONTINUE
      DO 250 J=1,11
      K=I(J)+1
      MCCNT(J,K)=MCCNT(J,K)+1
  250 CONTINUE
C     WRITING OUT RESULTS
      WRITE (4,20) (I(J),J=1,11),IC1,IC2,(TITLE(I),I=1,ITITLE)
   20 FORMAT (//5X,11I1,5X,I6,A3,/(21X,16A6,A3))
      WRITE (4,21)
   21 FORMAT (120H    R1      R2      R3      R4      R5      R6      R7      R8      R9
     1 R9/R8 R9/R5 R8/R5 R7/R6 R7/R5 R6/R5 R6/R2 R6/R1 R5/R4 R5/R3 R2/R1
```

```
      2)
      WRITE (4,22) (YSUM(I),I=1,9),(RAT(I),I=1,11)
   22 FCRMAT (1X,F5.2,19(F6.2))
      WRITE (6,60) ((I(J),J=1,11),IC1,IC2,(RAT(I),I=1,11),NTITLE,(TITLE(I
    . 1),I=1,NTITLE)
   60 FCRMAT (2X,11I1,5X,A6,A3,11F6.3,/2X,I2,6X,19A6)
      GC TC 5
 1000 IF (NENC) 1050,1C50,25
 1050 NENC=1
      GC TO 5
   25 WRITE (9,26)
   26 FCRMAT (3HENC)
      WRITE (4,255)
  255 FCRMAT (16HHISTCGRAM TABLE)
      WRITE (4,260)
  260 FCRMAT (1H-, 9X,1HO,5X,1H1,5X,1H2,5X,1H3,5X,1H4,5X,1H5,5X,1H6,5X,1
     1H7,5X,1H8,5X,1H9)
      WRITE (4,270) ((PCCNT(I,J),J=1,10),I=1,11)
  270 FCRMAT (/5HR9/R8,10(2X,I4),//5HR9/R5,10(2X,I4),//5HR8/R5,10(2X,I4)
     1,//5HR7/R6,10(2X,I4),//5HR7/R5,10(2X,I4),//5HR6/R5,10(2X,I4),//5HR
     26/R2,10(2X,I4),//5HR6/R1,10(2X,I4),//5HR5/R4,10(2X,I4),//5HR5/R3,1
     30(2X,I4),//5HR2/R1,10(2X,I4))
      ENCFILE 4
      ENCFILE 6
      UNLCAC  3
      UNLCAC  4
      UNLCAC 6
      END
      END
```

Appendix C

DOCUMENTATION FOR COMPUTER PROGRAM KOLEKT

KOLEKT uses a total of five tape drives; their use is as follows:

UNIT	FUNCTION	FORMAT	
2	input		Search Information
		2X,I3	NUMB= number of input tape rewinds to be made (= number of NOUT cards -1)
		2X,I3	NOUT= number of output tape drivers used (1, 2, or 3)
		1X,6A6	Arbitrary Title
		11(I1,1X,I1,3X)	eleven pairs of limits, one per ratio
3	input		data tape from ARAGAL (unit 6)
4, 5, or 6	output		If NOUT=1, the output is on unit 4. If NOUT=2, the first search after NOUT has its output on 4, the record has its output on 5. For NOUT=3, the last set of output goes on 6. Whenever NOUT > 1, at the end of a production run units 5 and 6 (if used) will rewind and the data on the tapes will be transferred to tape 4. Then tape 4 is listed for printed output. If any special order is desired on the output, care must be taken in the ordering of searches on unit 2.

For the format rows: One set per search, NOUT sets per rewind. NUMB+1 sets per run.

CDC 1604 COMPUTER LISTING OF KOLEKT

```
   PROGRAM KOLEKT
   DIMENSION  I(11),        TITLE(20),LIM(99),MX1(20) ,MX2(20),ATITLE
  10)
   INTEGER ECF,P1,P2,P3,P4
   L=1
   NMX=1
   NCNT2=0
   NCNT3=0
   CC 1   I=1,20
   MX1(I)=C
   MX2(I)=0
 1 CCNTINUE
   NUMB IS THE NUMBER OF REWINDS OF THE DATA TAPE TO BE DONE
   READ (2,2) NUMB
 2 FCRMAT (2X,I3)
   NCUT IS THE NUMBER OF CHANNELS CF OUTPUT FOR EACH SEARCH
 3 READ (2,2) NCUT
   NM=0
   MN=0
   IF (NCUT.GT.NMX) 40,41
40 NMX=NCUT
41 IF (NCUT-2) 45,43,42
42 NCNT3=NCNT3+1
43 NCNT2=NCNT2+1
   READING LIMITS FCR DATA SEARCH
45 P1=1
   P2=6
   P3=1
   P4=22
   DC  55 MMM=1,NCUT
   READ (2,4) (ATITLE(I),I=P1,P2),(LIM(I),I=P3,P4)
 4 FCRMAT (1X,6A6,/1X,11(I1,1X,I1,3X))
   P1=P1+6
   P2=P2+6
   P3=P3+22
   P4=P4+22
55 CCNTINUE
   WRITE (4,5)
 5 FCRMAT (//////)
   WRITE (4,4) (ATITLE(I),I=1,6),(LIM(I),I=1,22)
   IF (NCUT-2) 6,46,46
46 WRITE (5,4) (ATITLE(I),I=7,12),(LIM(I),I=23,44)
   IF (NCUT-3) 6,47,47
47 WRITE (6,4) (ATITLE(I),I=13,18),(LIM(I),I=45,66)
   ASSIGN  5C TC NCF
   CALL SETECF (NCF)
   READING CATA SET
 6 READ (3,7) (I(J),J=1,11),ID1,ID2              ,NTITLE,(TITLE(I),I=
  11,NTITLE)
 7 FCRMAT (2X,11I1,5X,A6,A3,              /2X,I2,6X,18A6)
   J=1
   CC  9 I=1,11
   IF (I(I).GE.LIM(J).AND.I(I).LE.LIM(J+1)) 8,15
 8 J=J+2
 9 CCNTINUE
   WRITE (4,10)(I(J),J=1,11),IC1,IC2,(TITLE(I),I=1,NTITLE)
1C FCRMAT(2X,11I1,5X,A6,A3,/1CX,18A6)
11 FCRMAT(2X,11I1,5X,A6,A3,2X,I2,/1CX,18A6)
15 IF (NCUT-2) 6,16,16
16 J=23
```

```
      CC 18   I=1,11
      IF (I(I).GE.LIM(J).AND.I(I).LE.LIM(J+1)) 17,19
17    J=J+2
18    CCNTINUE
      MM=MM+1
      WRITE (5,11)(I(J),J=1,11),IC1,ID2,NTITLE,(TITLE(I),I=1,NTITLE)
19    IF (NCUT-3) 6,20,20
20    J=45
      DC 22   I=1,11
      IF (I(I).GE.LIM(J).AND.I(I).LE.LIM(J+1)) 21,6
21    J=J+2
22    CCNTINUE
      MN=MN+1
      WRITE (6,11)(I(J),J=1,11),IC1,IC2,NTITLE,(TITLE(I),I=1,NTITLE)
      GC TC 6
50    MX1(L)=MM
      MX2(L)=MN
      IF (NUMB) 25,25,24
24    REWINC 3
      NUMB=NUMB-1
      L=L+1
      GC TC 3
25    IF (NMX.GT.1)26,35
26    ENCFILE 5
      REWINC  5
      IF (NMX.GT.2)27,28
27    ENCFILE 6
      REWINC  6
28    DC 31   I=1,NCNT2
      WRITE (4,5)
      REAC (5,4) (ATITLE(J),J=1,6),(LIM(J),J=1,22)
      WRITE (4,4) (ATITLE(I),I=1,6),(LIM(I),I=1,22)
      DC 30  K=1, MX1(I)
      REAC (5,11)(I(J),J=1,11),ID1,IC2,NTITLE,(TITLE(J),J=1,NTITLE)
      WRITE(4,10)(I(J),J=1,11),IC1,ID2,(TITLE(J),J=1,NTITLE)
30    CCNTINUE
31    CCNTINUE
      IF (NCNT3) 35,35,32
32    DC 34  I=1,NCNT3
      REAC (6,4) (ATITLE(J),J=1,6),(LIM(J),J=1,22)
      WRITE (4,5)
      WRITE (4,4) (ATITLE(I),I=1,6),(LIM(I),I=1,22)
      DC 33  K=1,MX2(I)
      REAC (6,11)(I(J),J=1,11),IC1,IC2,(TITLE(J),J=1,NTITLE)
      WRITE(4,10)(I(J),J=1,11),IC1,ID2,(TITLE(J),J=1,NTITLE)
33    CCNTINUE
34    CCNTINUE
35    ENCFILE 4
      UNLCAC  2
      UNLCAC  3
      UNLCAC  4
      UNLCAC  6
      END
      END
```

Appendix D

AN ERTS EXPERIMENT FOR MAPPING IRON COMPOUNDS

[Reprint from Ref. 24]

General

The general objectives of this investigation are to develop a quantitative method for mapping lithologic units strongly associated with iron oxides, and to use this method to map iron oxides in the vicinity of the Wind River Range, Wyoming.

Progress During Period, 1 July - 31 August 1973

In this reporting period six ratio images and an automatic recognition map were made of an entire ERTS frame (E-1013-17294), a field trip was made to collect ground truth data, and temporal ratio maps were used to demonstrate that dark object subtraction and ratio normalization procedures described in the Second Type I report are correcting well for atmospheric and solar illumination effects. The automatic recognition map was constructed by making ratio inputs to a standard statistical decision method. Some stratigraphic mapping appears possible on a geochemical basis in the plains east of the Wind River Range, even though the grass cover is on the order of 40%. Besides the automatic recognition map (made with six ratios), an R_{54} (channel 5 divided by channel 4) ratio image delineates the hematitic Triassic red beds well, because the hematite is the brightest material in the scene in that image. This is in agreement with ratio codes calculated from laboratory data, which predict that hematite has a higher R_{54} ratio than 90% of the natural materials in the data bank. A list of materials and ratio codes is given in the recent Type II report for the period 1 January - 30 June 1973.

The field trip was successful, but only a small part (approximately 10%) of the processed ERTS frame could be observed owing to rugged terrain, unusually wet weather, and limited funds. Geologic maps will be used as ground truth for the rest of the frame. The bottom of the iron mine is composed mostly of magnetite ore, tailings, and some gangue rock of similar appearance. The Triassic red beds are strongly hematitic and are less vegetated than other members of the stratigraphic column near the Wind River Range. There is more grass cover than was expected on almost all targets; an overall estimate of grass cover (mostly brownish, even though it has been a wet year) on well exposed lithologic units in the region is 30-50%. It is encouraging that some geologic mapping can be done on a geochemical basis with so large an estimated percentage of grass cover. The only known natural iron ore outcroppings are not exposed in large enough areas to be identified on the recognition map. The typical naturally exposed iron ore in the area was on the order of less than 100 meters in diameter, which would be less than one resolution element in ERTS data.

A study to evaluate the effectiveness of the ratio method for suppressing atmospheric and solar illumination changes has been undertaken. The ratio method involves a subtraction of the

radiance detected from the darkest object in a given scene (usually a quarter of an ERTS frame) from all other points in the scene for each ERTS MSS channel, a ratioing of the remaining radiances in two MSS channels, and a normalization of the ratio to a single known area (on the order of 5 to 10 spatial resolution elements) in the scene. These steps approximately eliminate the additive and multiplicative atmospheric and solar illumination terms, leaving a spectral ratio of target reflectances.

To assess the effectiveness of this procedure, a temporal ratio map was produced in the following way. Spectral ratio maps (R_{75} for example) of two different ERTS passes are produced, with dark object subtraction and ratio normalization applied to correct for atmospheric and solar illumination effects. The two spectral ratio maps are merged such that they spatially coincide, and the spectral ratio map from one ERTS pass is divided by the spectral ratio map from the other ERTS pass to produce a temporal ratio map. If the empirical atmospheric and solar illumination corrections are effective, the temporal ratio should be at or near 1.0 for those objects on the ground which have not changed between ERTS passes. The area chosen for the temporal ratio map includes the iron mine near Atlantic City, Wyoming. The two ERTS passes were on 5 August 1972 (E-1013-17294) and 16 October 1972 (E-1085-17300). The 5 August frame had 0% cloud cover and was collected with sun elevation of 54.9° and sun azimuth of 130.2°, whereas the 16 October frame had 20% cloud cover (including some clouds in the scene used for the temporal ratio) and was collected with sun elevation of 34.0° and azimuth of 153.4°. Because of the differences in atmospheric state (evidenced by cloud cover) and sun position, these two frames offered a rigorous test of the empirical correction steps in the ratio method. The specific test site in the vicinity of the iron mine (which includes the ten resolution elements used for ratio normalization) was approximately 25% covered by cumulus clouds in the 16 October frame and was completely cloud-free in the 5 August frame. The path radiance, as determined from dark object subtraction, was approximately the same for both frames, though the multiplicative atmosphere and solar illumination variables were significantly different in the two frames.

The procedure for testing the atmospheric solar illumination invariance of the ratio method begins with an estimate of the number of elements (spatial resolution elements on the order of 100 meters in diameter) within the scene which had less than 50% vegetative cover in the 5 August frame and were uncovered by clouds in the 16 October frame. These elements, which will be called the ground invariant (GI) elements, represent the portion of the test area which is suspected not to have changed more than ±5% in spectral reflectance between the two ERTS passes. The non-vegetated areas were determined from a thresholding of an R_{75} ratio of 1.20, which appeared to approximately delineate areas of less than 50% vegetation cover on the basis of ground photographs and observations made during the 21-27 July 1973 field trip to the test area. The vegetation is primarily a mixture of coniferous and deciduous trees, coarse grass, and sage. The

111

cloud areas were delineated easily by ratioing ERTS MSS channel 7 for the 16 October frame to the same channel for the 5 August frame. [Note: In this section, the ratio of either spectral ratio or single-channel radiance maps from two different ERTS passes will be called a temporal ratio map.] The resulting map of the GI elements is shown in Figure D-1. The number of GI elements equaled 11,032 points out of a total of 25,125 points in the entire scene.

Next, a temporal ratio map of ERTS MSS channel 7 was constructed, which is shown in Figure D-2a; channel 7 radiance in the 16 October frame was divided by the channel 7 radiance in the 5 August frame. Figure D-2b shows a temporal ratio map of ERTS MSS channel 5. In all of the temporal ratio maps to be discussed, the 16 October frame data are in the numerator, with 5 August data in the denominator. Also, in this and all other temporal ratio maps, lighter-toned areas represent small changes (small departures of the temporal ratio from 1.0) and darker-toned areas represent large changes; the key to interpreting the symbols in all of the temporal ratio maps is given in Table D.1. Only 361 elements in the scene changed between ERTS passes by approximately ±5% or less (temporal ratio between 0.96 and 1.05) in the channel 7 temporal ratio, which represents only 3.27% of the GI elements (11,032). In the channel 5 temporal ratio map shown in Figure D-2b, there were 1,122 elements (10.17% of the GI elements) in the scene which changed by ±5% or less. Because channel 7 changes more between ERTS passes than channel 5 and because the path radiance as determined from dark object subtraction is approximately the same for both passes, it is concluded that the change in solar illumination was greater than the change in atmosphere between 5 August and 16 October for this test site.

In Figure D-3a is a temporal ratio map of a straight R_{75} spectral ratio, uncorrected by dark object subtraction and ratio normalization. The number of elements which changed by ±5% or less between ERTS passes in this case was 2,320 (21.02% of the GI elements). Thus, even an uncorrected R_{75} spectral ratio map is more invariant than single-channel radiance maps to atmospheric and solar illumination variations. Shown in D-3b is a temporal ratio map of an R_{75} spectral ratio, corrected by both the dark object subtraction and ratio normalization steps. For this case, the number of elements which changed by ±5% or less between ERTS passes was 11,032 (37.30% of the GI elements). Therefore, the corrective steps of the ratio method produce a spectral ratio map which is more invariant to atmospheric and solar illumination variations than either uncorrected spectral ratios or maps of single-channel radiances.

As to the absolute effectiveness of the ratio method for suppressing atmospheric and illumination effects, the temporal ratio map procedure offers only an approximate answer. Table D.2 shows the elements changing ±5% or less, ±10% or less, and ±15% or less between ERTS passes, expressed as a percentage of GI elements. This shows that the corrected R_{75} spectral ratio for

FIGURE D-1. ESTIMATED GROUND-
INVARIANT ELEMENTS BETWEEN
5 AUGUST AND 16 OCTOBER 1972
ERTS PASSES OVER ATLANTIC
CITY, WYOMING, TEST SITE. Dark
symbols represent elements in the
scene which have more than 50% veg-
etative cover, or which were cloud-
covered in the 16 October ERTS frame.
Blank areas represent elements in the
scene which are suspected of having
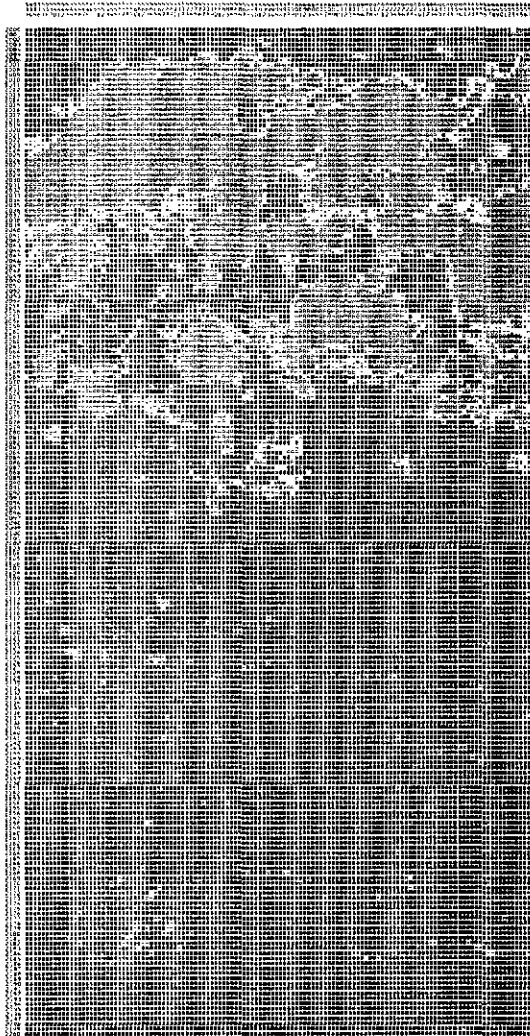changed less than 5% in spectral re-
flectance between the two ERTS passes.

113

TABLE D.1. KEY TO SYMBOLS FOR TEMPORAL
RATIO MAPS IN FIGURES D-2 AND D-3

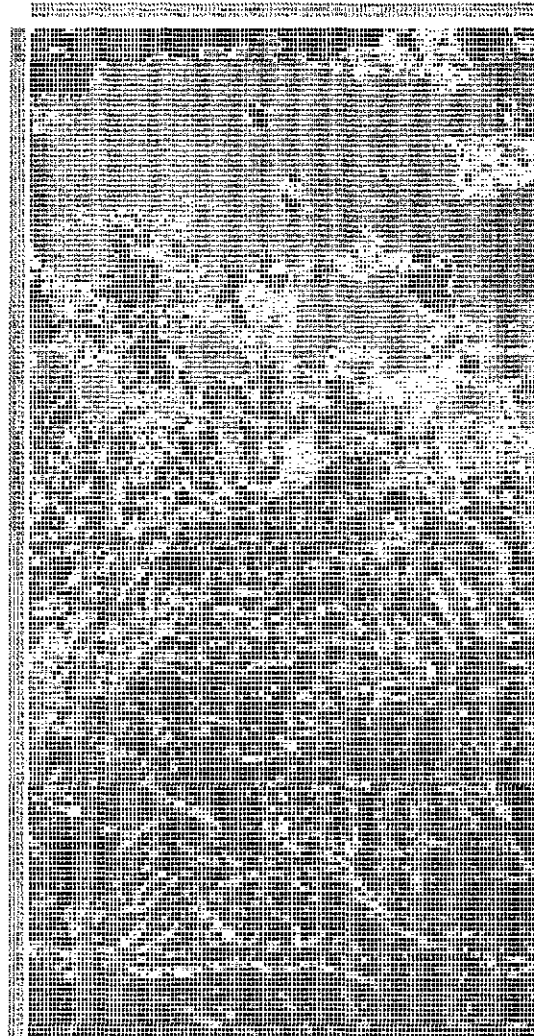| Temporal Ratio	Percent Change Between ERTS Passes	Symbols
≤0.80	≤ -20%	⋈
0.81 to 0.85	-19% to -15%	✕
0.86 to 0.90	-14% to -10%	=
0.91 to 0.95	-9% to -5%	-
0.96 to 1.05	-4% to +5%	Blank
1.06 to 1.10	+6% to + 10%	·
1.11 to 1.15	+11% to + 15%	*
≥1.16	≥+16%	θ

TABLE D.2. ESTIMATE OF R_{75} SPECTRAL RATIO ABSOLUTE INVARIANCE
CORRECTED BY DARK OBJECT SUBTRACTION AND RATIO NORMALIZATION.
Temporal ratio map of 16 October 72 and 5 August 72 ERTS passes over a test
site near Atlantic City, Wyoming.

| Change in Corrected R_{75} Between ERTS Passes (%)	Number of Elements Undergoing Change	Estimated Ground Invariant Elements* (%)
±5	4,115	37.30%
±10	7,745	70.20%
±15	10,682	96.83%

*11,032 element total.

(a) ERTS MSS Channel 7   (b) ERTS MSS Channel 5

FIGURE D-2. TEMPORAL RATIO MAPS OF 16 OCTOBER FRAME DIVIDED BY 5 AUGUST
FRAME. Lighter-toned symbols represent less change in the scene between ERTS passes
(See Table D.1).

115
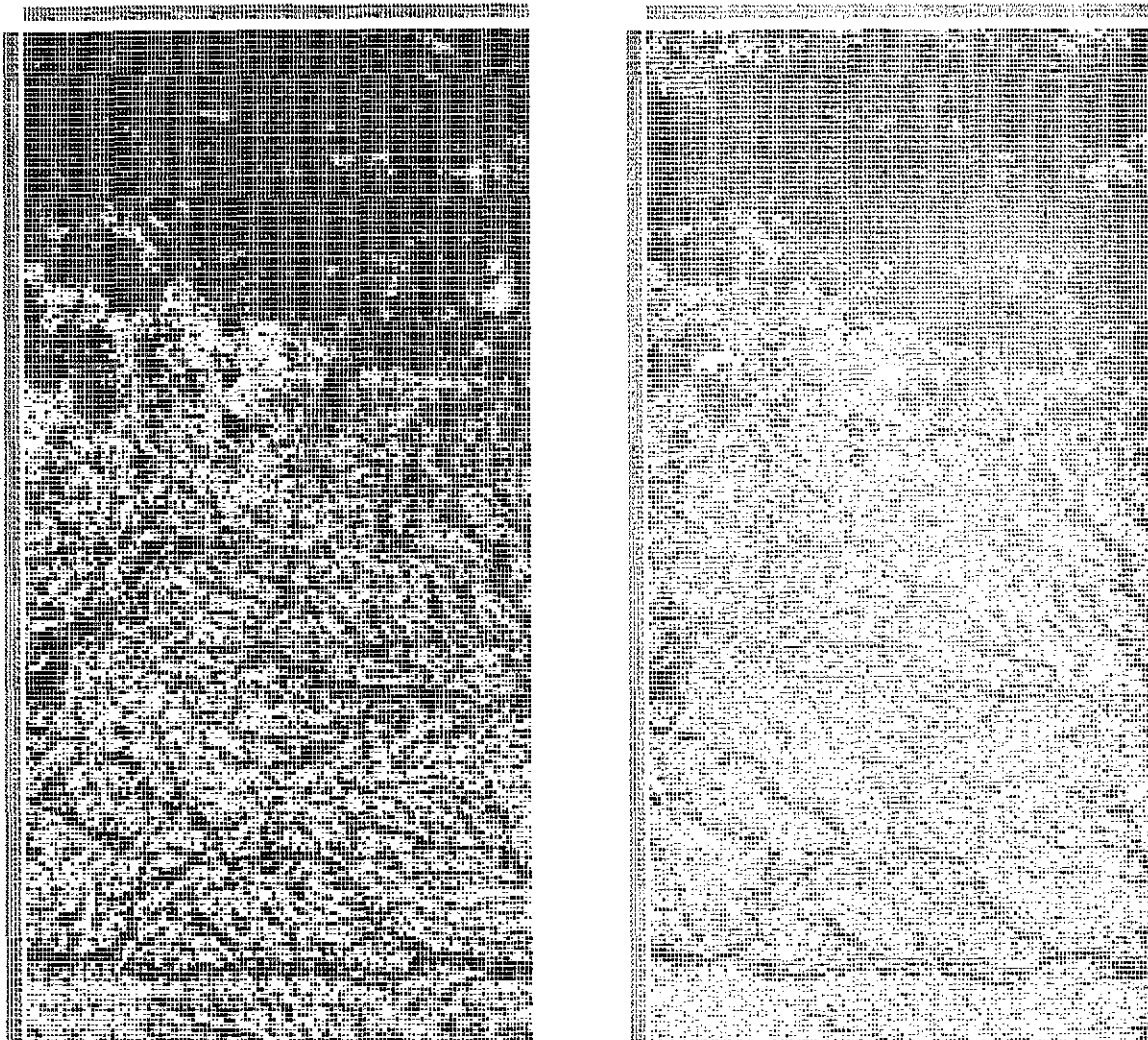
(a) Uncorrected R_{75} Spectral Ratio   (b) Corrected R_{75} Spectral Ratio

FIGURE D-3. TEMPORAL RATIO MAPS OF CORRECTED AND UNCORRECTED R_{75} RATIOS:
16 OCTOBER FRAME DIVIDED BY 5 AUGUST FRAME. Lighter tones represent areas of
lesser change between the two passes. (See Table D.1.)

this test site was invariant to atmospheric and illumination changes between 5 August and 16 October ERTS passes to within ±10% for 70% of the GI elements and to within ±15% for practically all of the GI elements (97%). These absolute numbers are only approximate because of three sources of error:

(1) Some of the estimated GI elements could have changed, by natural and unnatural causes, more than ±5% during the ERTS passes.

(2) The merging process is estimated to be accurate to within about two spatial resolution elements, which means that some points expected to be GI elements may show change only because of the merging process.

(3) No attempt was made to discount points with small change that occurred in non-GI elements, though a comparison of Figures D-1 and D-3b shows that the vast majority of elements exhibiting small change in corrected R_{75} values are GI elements.

The first two sources of error make the results of Figures D-2 and D-3 and Table D.2 appear worse than they actually are, whereas the third error source makes them appear better than actual fact. During the next reporting period, the third error will be corrected. These considerations and the above quantitative results indicate that the corrected R_{75} ratio map may be invariant to atmospheric and illumination effects to within ±10% or better.